

**A Stepped Frequency Continuous Wave Ranging Sensor for Aiding Pedestrian
Inertial Navigation**

Submitted in partial fulfillment of the requirements for
the degree of
Doctor of Philosophy
in
Electrical and Computer Engineering

James M. Downey

B.S., Electrical Engineering, The University of Toledo
M.S., Electrical & Computer Engineering, Carnegie Mellon University

Carnegie Mellon University
Pittsburgh, PA

August, 2012

Copyright 2012, James M. Downey. All rights reserved.

To my parents and grandparents.

ACKNOWLEDGEMENTS

I would like to thank the Defense Advanced Research Projects Micro-Inertial Navigation Technology program and the Air Force Research Laboratory for supporting this work.

My two thesis advisors, Professor Dan Stancil and Professor Tamal Mukherjee, were both sources of inspiration and exceptional guidance during my graduate studies. Dan's talent to take difficult concepts and explain them in an intuitive way sets the standard for what it means to be a great teacher. His always thoughtful comments and eagerness to pursue far-out ideas has made for an enjoyable 6 years. Though Tamal has not been my advisor as long as Dan, he certainly has been just as influential. Tamal's ability to frame a research problem from a broader perspective one moment and then dig deep into the finer details the next was immensely helpful. Whenever I had a problem interpreting some piece of data, Tamal would catch a subtle detail and bring everything back into focus. I would also like to thank my thesis committee members, Professor Jeyanandh Paramesh and Dr. Obed Scott Sands, for their contribution to my education. Jeyanandh's door was always open for interesting discussions on architecture and theory. Scott's inquisitive nature has kept me on my toes and our long conversations have led to interesting projects.

I would like to thank Michel Laverne, Michael George and Dane Bennington for their invaluable help with hardware development and measurements. This acknowledgement would not be complete without recognizing my official and adopted officemates: Reginald Cooper, Joey Fernandez, Darmindra Arumugam and Chenming Zhou. I have thoroughly enjoyed our time together, the long discourses on the random topic of the day, theoretical diversions, and covering for Matt. And I must also recognize Sadie and Eric Tedder who helped me refine the perfect grad student state: the juxtaposition of on and off task. Finally, I thank my family, friends, small group, and the LORD for your encouragement and support throughout this effort.

ABSTRACT

Pedestrian navigation is readily enabled by GPS in outdoor environments. However, there are many locations - such as indoors, urban canyons and underground - where the GPS signal is unreliable or unavailable. Compact inertial navigation, through the use of MEMS accelerometers and gyroscopes, has been applied to a pedestrian's shoes as a means to navigate without GPS. MEMS inertial technology has issues with sensor bias drift, causing significant navigational errors. Simulations by Brand and Phillips and experimental results from Laverne et al. have shown that the addition of a scalar range between shoes can constrain this error growth. A shoe ranging sensor (SRS) using radar technology, due to its relative insensitivity to environmental factors such as dirt and dust, will be applied to provide this scalar range. Commercially available radars generally operate over longer ranges ($>> 1$ m) and relatively coarse accuracy (>1 cm). This dissertation proposes stepped frequency continuous wave (SFCW) modulation will fill the technology gap and provide a ranging solution with <1 cm RMS accuracy in a 1 m range. The SRS architecture is extended using time division multiplexing to generate multiple ranges for estimating relative shoe heading. Theoretical limits on SFCW and combined CW ranging accuracy are derived. A ray-tracing channel model is developed for SRS simulation to analyze ranging performance on different surfaces, antennas and ranging algorithms (Fourier and Prony estimation). The channel model extends the Friis transmission equation to include propagation phase and develops a method to calculate phase from arbitrary antenna polarization and orientation. Measurements performed validate channel model and demonstrate antenna limited sub-cm ranging performance on metal, concrete and anechoic foam. Walking tests of the SRS co-mounted with an acoustic range sensor show good agreement.

TABLE OF CONTENTS

ACKNOWLEDGEMENTS	v
ABSTRACT	vii
TABLE OF CONTENTS	viii
LIST OF FIGURES	xi
LIST OF TABLES	xvii
LIST OF COMMON SYMBOLS	xxi
1. INTRODUCTION	1
2. RANGING TECHNOLOGY	4
2.1. Methods	4
2.1.1. Acoustic	4
2.1.2. Optical	5
2.1.3. Radio Frequency	5
2.2. Technical Requirements	6
2.3. RF Ranging	8
2.3.1. Resolution and Accuracy	9
2.3.1.1. RMS Phase Error	11
Impact of Oscillator Phase Noise	13
2.3.1.2. RMS Time Delay	14
2.3.2. Continuous Wave Radar	15
2.3.2.1. Hybrid Ranging and Accuracy	17
2.3.3. Frequency Modulated Continuous Wave Radar	19
2.3.4. Stepped Frequency Continuous Wave Radar	21
2.3.4.1. Derivation of SFCW Effective Bandwidth	22
2.3.5. Performance Summary	26
2.3.6. Multi-Ranger Architecture	27
3. THE CHANNEL	30
3.1. 2-Ray Flat Earth Model	31
3.2. LOS Propagation	32
3.3. NLOS Propagation	35

4. RANGING ALGORITHMS	39
4.1. Fourier Transform	39
4.1.1. Chirp z -Transform	40
4.2. Prony Analysis	42
4.3. CW Ranging	46
4.4. Range Filtering	47
4.4.1. Range Limits	48
4.4.2. Line-of-Sight	48
4.4.3. Antenna Location	48
4.4.4. Range Circle Intersection	49
5. SHOE RANGING SENSOR SIMULATOR	50
5.1. SRS Simulator Design	51
5.1.1. Antenna Integration	52
5.1.2. Multi-Ranger Extension	53
5.2. Channel Model Verification	54
5.3. SRS Simulation Results	56
5.3.1. Multiple Surface Results	57
5.3.2. Metal & Concrete	61
5.3.2.1. Performance Enhancement	63
5.3.2.2. Multipath Analysis	64
5.3.3. Multi-Ranger Simulation	66
5.3.3.1. Switch Attenuation	68
5.4. Summary	69
6. SRS HARDWARE	70
6.1. SRS Transceiver	70
6.2. FPGA Data Acquisition	73
6.3. Antennas	75
6.3.1. Dipole with Balun	76
6.3.2. E-Shaped Patch Antenna	77
6.3.3. Vivaldi Antenna	79
6.4. Antenna Mounting	80
7. SRS MEASUREMENTS	82
7.1. Calibration	82
7.1.1. VCO Frequency	82
7.1.2. Mixer DC Offset	83
7.1.3. RF Cable and VCO Power	84
7.1.4. Multi-Ranger Cable	84
7.1.5. Range	85

		x
7.2. Motion Stage Measurements		86
7.2.1. Stage Alignment		86
7.2.2. Results		88
7.2.2.1. Tabulated Results		89
Concrete		89
Microwave Absorbing Foam		91
Aluminum Plate		94
7.2.2.2. Optimal Antenna Alignment		96
Simulation of Lateral Separation		97
7.2.3. Analysis		98
7.2.3.1. Channel Power		101
7.2.3.2. Hybrid Ranging		102
7.2.3.3. Calibration Stability		104
7.2.3.4. Multipath Extraction		105
7.2.4. Walking Test		107
7.2.4.1. Single Ranger Heel Mount		107
7.2.4.2. Single Ranger Arch Mount		108
7.2.4.3. Multi-Ranger Test		110
7.3. Summary		111
8. CONCLUSION		113
8.1. Contributions		114
8.2. Future Work		115
8.2.1. Hardware		116
8.2.2. Simulation		117
8.2.3. Algorithms		117
A. COORDINATE TRANSFORMATIONS		118
A.1. Single Axis rotation		119
A.1.1. Rotation Matrices		119
A.1.2. LOS Vector in Antenna Frame		121
A.1.3. Spherical Unit Vectors in NED Frame		121
A.2. Euler Angles		123
REFERENCES		125

LIST OF FIGURES

Fig. 2.1. IMU data of a single step of right foot: position (a) and orientation (c). Computed range (b) between two antennas and corresponding range velocity (d). Gray highlighted regions indicate right shoe is moving (left is fixed). R1 is between antennas both located at the back of the shoe; R2 is between front on right shoe and back on left shoe.	7
Fig. 2.2. SRS concept: antennas are located on each foot with phase stable RF cables to a backpack mounted transceiver.	8
Fig. 2.3. Radar resolution, with bandwidth B , of two closely spaced targets.	9
Fig. 2.4. Phasor A_s corrupted with random noise A_N (left). Phasor with average angle, θ , removed and components of noise vector shown (right).	11
Fig. 2.5. Normalized error of approximation to sampled RMS phase error $\delta\theta$	12
Fig. 2.6. CW radar with range ambiguity. Note topology is different than SRS with transmitted wave reflecting off of a target.	16
Fig. 2.7. Probability of selecting the correct n given normalized coarse range standard deviation ς ..	19
Fig. 2.8. Left (a), VCO tuning waveform for FMCW and hybrid FMCW+CW. Right (b), transmitted and received FMCW waveform. Beat frequency Δf_b is proportional to channel delay Δt	20
Fig. 2.9. Example VCO tuning waveform for SFCW (a). Fourier transform of SFCW channel data, τD is the location of the peak corresponding to target range (b).....	22
Fig. 2.10. Comparison of RMS bandwidth calculation between delta function approximation and rect function with SSB 1MHz. Sweep bandwidth is 1.5 GHz.	25
Fig. 2.11. SRS Multi-Ranger concept: 2 antennas on each shoe connect through an RF switch to the backpack mounted transceiver. RF switches select which antenna pair are active (A2 and A3 displayed).....	27

Fig. 3.1. Plane of incidence and geometry for 2-ray flat earth model. Dotted lines aid in defining the geometry (a). Top view and global coordinate system North East Down (b).....	31
Fig. 3.2. Projection of \mathbf{pt} into receive coordinate frame formed by $\theta r, \phi r$ (a). \mathbf{pt} in native coordinate frame (b) and resulting \mathbf{ptr} vector in $\theta r, \phi r$ frame (c).....	33
Fig. 3.3. Skin depth for various materials vs. frequency.....	35
Fig. 3.4. Oblique incidence geometry at surface interface between medium 1 and 2 for perpendicular (a) and parallel (b) electric field components in plane-of-incidence.....	37
Fig. 4.1. Overview of Chirp- \mathbf{z} ranging algorithm.	41
Fig. 4.2. Overview of Prony ranging algorithm.	45
Fig. 4.3. LOS blockage of vector \mathbf{R} between antennas A1 and A4.	48
Fig. 4.4. Range circle intersection between A1, A2 and A3. $L1$ is the fixed distance between A1 and A2.	49
Fig. 5.1. SRS Multi-Ranger naming convention (left). Finite isolation RF switch fed by RF cables with length $Lc1, L1$, and $L1$ for the left shoe (right). Coordinate systems are defined for each IMU.....	53
Fig. 5.2. Experimental setup for measuring polarization phase.	55
Fig. 5.3. Comparison between SRS Simulator and measured polarization phase.	56
Fig. 5.4. Ground truth range LOS & NLOS and range difference.	57
Fig. 5.5. Summary of SRS Simulator RMS range error across all surfaces. Chirp- \mathbf{z} in circles and TLS Prony in *.	60
Fig. 5.6. SRS Simulator polarization phase for different antennas	61
Fig. 5.7. SRS Simulator peak power of time domain envelope (Chirp- \mathbf{z}) on concrete.	62

Fig. 5.8. SRS Simulator range solutions for concrete (left) and metal (right). TLS is Prony method and CZT is Chirp- \mathcal{Z} method.....	63
Fig. 5.9. SRS Simulator range solutions for concrete with optimal frequency sweep and location clipping ($R < 0.3$ m). TLS is Prony method and CZT is Chirp- \mathcal{Z} method.	64
Fig. 5.10. SRS Simulator channel response at 1.9483 s (left) and 2.365 s (right) on concrete with Vivaldi antenna. Top figures are channel spectral response and bottom are Chirp- \mathcal{Z} time domain response each decomposed into LOS and NLOS signals. Prony solutions plotted as delta functions in bottom figures.	65
Fig. 5.11. SRS Simulator Prony LOS and NLOS range solutions for concrete and Vivaldi Antenna (left). Ground truth range for LOS and NLOS (right).	66
Fig. 5.12. Summary of SRS Multi-Ranger Simulator RMS range error on copper, concrete along with optimal frequency sweep and 0.3 m range clipping. Chirp- \mathcal{Z} in circles and TLS Prony in *.	67
Fig. 5.13. SRS Multi-Ranger Simulator Prony range solutions on concrete with optimal frequency sweep and Vivaldi antennas.....	68
Fig. 5.14. Effect of non-ideal switch isolation on Prony RMS error. SRS Multi-Ranger Simulator on concrete with optimal frequency sweep and Vivaldi antennas.	69
Fig. 6.1. Block diagram of SRS Multi-Ranger transceiver architecture – outer dashed box contains components in dashed area of PCB (Fig. 6.3).....	71
Fig. 6.2. S-parameters of Wilkinson splitter – port 1 connects to VCO, port 3 to the transmit antenna and port 2 to the mixer.	72
Fig. 6.3. SRS Transceiver PCB (left and middle) – left shows without EMI can. RF switch and LVDS control board (right).....	73
Fig. 6.4. FPGA Data Acquisition board top and side view with SRS Transceiver board attached.	74
Fig. 6.5. 7 GHz dipole antenna with integrated balun (left). 3D and 2D gain plots (right).....	75

Fig. 6.6. E-shaped patch antenna (left). 3D and 2D gain plots (right).....	76
Fig. 6.7. Vivaldi antenna with right angle feed (left). 3D and 2D gain plots (right).....	77
Fig. 6.8. Vivaldi antenna with straight feed (left). 3D and 2D gain plots (right).....	78
Fig. 6.9. S-parameters of patch, dipole and Vivaldi antennas.....	79
Fig. 6.10. Patch antennas on Hydlar-Z mount on shoe with IMUs (left). Rogers RO4003 Vivaldi antennas mounted with carbon fiber on the motion stage (right).....	80
Fig. 7.1. SRS Multi-Ranger RF cable layout and calibration point <i>SREF</i>	83
Fig. 7.2. SRS Multi-Ranger on motion stage with foam surface. The moving antennas (A3 & A4) are shown at peak positions of the cosine motion. Fixed position P1 in a, b. Fixed position P2 in c, d. Coordinate system for antenna alignment shown in b.	86
Fig. 7.3. Laser alignment of linear motor axis.....	87
Fig. 7.4. From left to right: concrete, metal and foam surfaces.	88
Fig. 7.5. Inline Vivaldi antennas experimental setup with SRS single ranger (left). Measured error versus position using level 0 range filtering and Chirp- \mathcal{Z}	96
Fig. 7.6. Vivaldi antenna with straight coax feed and aluminum mount 2D and 3D gain patterns (left). Effect of left shoe lateral separation on RMS range error and antenna model choice in SRS Simulator (right).....	97
Fig. 7.7. Measured versus simulated RMS error using level 2 range filtering. Left Prony method, right Chirp- \mathcal{Z} . Blue is concrete, black is foam and red is metal.	98
Fig. 7.8. Prony computed range plots comparing level 0 (left) and level 2 (right) filtering. Cropped to 17 s due to ground truth alignment. R1 and R4 ground truth are approximately equal.	99
Fig. 7.9. Simulated and measured channel spectral response for concrete position P1 (6/20/12). Left corresponds to max range (2.75 s), right is min range (3.65 s).	100

Fig. 7.10. Comparison of Prony and Chirp- z (CZT) only solution with CW phase Hybrid ranging. Range plots on left, range error on right. Dataset is concrete at position P1 (6/20/12).....	101
Fig. 7.11. Range error and wavelength bin selection across frequency at 0 s (left). Range error across motion for all N measurements in dots – solid line is the final range solution from averaging all measurements (right). Average error is removed for all range error plots. Dataset is concrete at position P1 (6/20/12) and range R1 computed using Chirp- z	102
Fig. 7.12. Top, calibration stability over 1 hr shown through 10 s moving average of range error on concrete (6/20/12). Bottom, coarse and fine range error distribution of R1 with normal distribution fit. Prony on left, Chirp- z (CZT) on right.....	103
Fig. 7.13. Prony extraction of NLOS (right) and LOS (left) components ($M=20, m=2$). Top figures are Prony range output alone, middle figures add CW phase for hybrid ranging. Dataset is concrete at position P1 (6/20/12) with level 0 filtering. Bottom two figures show simulated ($M=3, m=2$) R1 and R3 hybrid ranges along with ground truth.	104
Fig. 7.14. Vivaldi antenna mounted to back of shoe with acoustic sensor (left). Walking results (7/25/12) on carpeted wood walkway using several ranging algorithms and acoustic ranger (right).	106
Fig. 7.15. Walking results (7/25/12) on concrete floor using several ranging algorithms and acoustic ranger (left). Ranging results during turn (right).	107
Fig. 7.16. Vivaldi antenna mounted in the forward position above arch of shoe (left). Walking results (7/27/12) on concrete floor using several ranging algorithms and acoustic ranger (right).....	108
Fig. 7.17. Walking results (7/27/12) on concrete floor using several ranging algorithms and acoustic ranger (sodar). Full dataset view (left) and zoomed section (right).	109

Fig. 7.18. Vivaldi antenna mounted in the forward position above arch of shoe and centered on the carbon fiber bar (left). Walking results (7/27/12) on concrete floor using several ranging algorithms and acoustic ranger (right).....	110
Fig. 7.19. Patch antenna mounted to shoe on Hydlar Z material (left). R1 walking results using SRS Prony algorithm and LOS filtering (middle). Simulated and measured R1 Prony power (right).	111
Fig. A.1. Global NED, IMU and antenna (ANT) frame definitions. All frames and rotations use right-handed conventions.....	119
Fig. A.2. Spherical coordinate system used for antenna electric field vectors.	122
Fig. A.3. Euler rotation sequence (zyx, left to right) to x" y" z" frame.....	123

LIST OF TABLES

Table 2.1. Comparison between a selection of existing RF ranging technologies with requirements of the SRS Ranger and Multi-Ranger (see section 2.3.6)	8
Table 2.2. Design equations for CW, FMCW and SFCW waveforms.....	26
Table 2.3. Summary of radar parameters for CW, FMCW and SFCW examples.....	26
Table 2.4. Comparison between a selection of existing RF ranging technologies with proposed SRS Ranger and SRS Multi-Ranger.	28
Table 3.1. Electromagnetic properties of various materials.	36
Table 5.1. SRS Simulator steps.....	51
Table 5.2. Ranging algorithm comparison with copper surface.....	58
Table 5.3. Ranging algorithm comparison with steel surface.....	58
Table 5.4. Ranging algorithm comparison with concrete surface.....	58
Table 5.5. Ranging algorithm comparison with asphalt surface.	58
Table 5.6. Ranging algorithm comparison with dry soil surface.....	58
Table 5.7. Ranging algorithm comparison with wet soil surface.	59
Table 5.8. Ranging algorithm comparison with snow surface.	59
Table 5.9. Ranging algorithm comparison with copper surface without CW ranging.....	59
Table 5.10. Ranging algorithm comparison with concrete surface without CW ranging.....	59
Table 5.11. Ranging algorithm comparison with optimal sweep, and location clipping (<0.3 m).	63
Table 5.12. SRS Multi-Ranger Simulator settings.....	67
Table 5.13. Algorithm comparison of multi-ranging on copper surface with Vivaldi antenna and ideal vs. leaky switch.....	67

Table 5.14. Algorithm comparison of multi-ranging on copper surface with Vivaldi antenna and ideal vs. leaky switch. Optimal frequency sweep with 0.3 range clipping used.	68
Table 5.15. Algorithm comparison of multi-ranging on concrete surface with Vivaldi antenna and ideal vs. leaky switch.....	68
Table 5.16. Algorithm comparison of multi-ranging on concrete surface with Vivaldi antenna and ideal vs. leaky switch. Optimal frequency sweep with 0.3 range clipping used.	68
Table 7.1. Initial antenna center positions in meters relative to surface and A2. Coordinate system in Fig. 7.2b, initial positions are shown in a) and c). Two alignments in position P1 were made... 87	
Table 7.2. Concrete results in mm. Position P1 cal-1, date taken: 5/16/12	89
Table 7.3. Concrete results in mm. Position P1 cal-1, date taken: 5/16/12. Filter drop percentage for each algorithm meas/sim in () after Range.....	90
Table 7.4. Concrete results in mm. Position P1 cal-1, date taken: 5/16/12. Filter drop percentage for each algorithm meas/sim in () after Range.....	90
Table 7.5. Concrete results in mm. Position P1 cal-2, date taken: 6/20/12	90
Table 7.6. Concrete results in mm. Position P1 cal-2, date taken: 6/20/12. Filter drop percentage for each algorithm meas/sim in () after Range.....	90
Table 7.7. Concrete results in mm. Position P1 cal-2, date taken: 6/20/12. Filter drop percentage for each algorithm meas/sim in () after Range.....	90
Table 7.8. Concrete results in mm for 1 hr cosine. Position P1 cal-2, date taken: 6/20/12	91
Table 7.9. Concrete results in mm for 1 hr cosine. Position P1 cal-2, date taken: 6/20/12. Filter drop percentage for each algorithm meas/sim in () after Range.....	91
Table 7.10. Concrete results in mm for 1 hr cosine. Position P1 cal-2, date taken: 6/20/12. Filter drop percentage for each algorithm meas/sim in () after Range.....	91
Table 7.11. Foam results in mm. Position P1 cal-1, date taken: 5/17/12.....	91

Table 7.12. Foam results in mm. Position P1 cal-1, date taken: 5/17/12. Filter drop percentage for each algorithm meas/sim in () after Range.....	91
Table 7.13. Foam results in mm. Position P1 cal-1, date taken: 5/17/12. Filter drop percentage for each algorithm meas/sim in () after Range.....	92
Table 7.14. Foam results in mm. Position P1 cal-2, date taken: 6/12/12.....	92
Table 7.15. Foam results in mm. Position P1 cal-2, date taken: 6/12/12. Filter drop percentage for each algorithm meas/sim in () after Range.....	92
Table 7.16. Foam results in mm. Position P1 cal-2, date taken: 6/12/12. Filter drop percentage for each algorithm meas/sim in () after Range.....	92
Table 7.17. Foam results in mm. Position P2, date taken: 6/12/12	92
Table 7.18. Foam results in mm. Position P2, date taken: 6/12/12. Filter drop percentage for each algorithm meas/sim in () after Range.....	93
Table 7.19. Foam results in mm. Position P2, date taken: 6/12/12. Filter drop percentage for each algorithm meas/sim in () after Range. “-“ indicates too many measurements were dropped.	93
Table 7.20. Foam results in mm for 1 hr cosine. Position P1 cal-2, date taken: 6/20/12.....	93
Table 7.21. Foam results in mm for 1 hr cosine. Position P1 cal-2, date taken: 6/20/12. Filter drop percentage for each algorithm meas/sim in () after Range.....	93
Table 7.22. Foam results in mm for 1 hr cosine. Position P1 cal-2, date taken: 6/20/12. Filter drop percentage for each algorithm meas/sim in () after Range.....	93
Table 7.23. Foam results in mm. Position P1 cal-2, date taken: 6/20/12.....	94
Table 7.24. Foam results in mm. Position P1 cal-2, date taken: 6/20/12. Filter drop percentage for each algorithm meas/sim in () after Range.....	94
Table 7.25. Foam results in mm. Position P1 cal-2, date taken: 6/20/12. Filter drop percentage for each algorithm meas/sim in () after Range.....	94

Table 7.26. Metal results in mm. Position P1 cal-2, date taken: 6/5/12	94
Table 7.27. Metal results in mm. Position P1 cal-2, date taken: 6/5/12. Filter drop percentage for each algorithm meas/sim in () after Range.....	94
Table 7.28. Metal results in mm. Position P1 cal-2, date taken: 6/5/12. Filter drop percentage for each algorithm meas/sim in () after Range.....	95
Table 7.29. Metal results in mm. Position P1 cal-2, date taken: 6/6/12	95
Table 7.30. Metal results in mm. Position P1 cal-2, date taken: 6/6/12. Filter drop percentage for each algorithm meas/sim in () after Range.....	95
Table 7.31. Metal results in mm. Position P1 cal-2, date taken: 6/6/12. Filter drop percentage for each algorithm meas/sim in () after Range.....	95
Table 7.32. Metal results in mm. Position P2, date taken: 6/11/12.....	95
Table 7.33. Metal results in mm. Position P2, date taken: 6/11/12. Filter drop percentage for each algorithm meas/sim in () after Range.....	96
Table 7.34. Metal results in mm. Position P2, date taken: 6/11/12. Filter drop percentage for each algorithm meas/sim in () after Range. “-“ indicates too many measurements were dropped.	96
Table 7.35. Concrete results in mm with Prony NLOS and LOS extraction ($M=20, m=2$). Position P1 cal-2, date taken: 6/20/12.....	106

LIST OF COMMON SYMBOLS

R	<i>range</i>
c	<i>speed of light in medium</i>
τ_D	<i>propagation time delay</i>
B	<i>Bandwidth</i>
σ, ς	<i>Standard deviation</i>
μ	<i>mean</i>
f	<i>Frequency</i>
λ	<i>Wavelength in medium</i>
τ	<i>VCO sweep time</i>
τ_s	<i>SFCW single frequency measurement time</i>
N	<i>Number of frequencies in SFCW sweep</i>
f_D	<i>Doppler frequency shift</i>
f_R	<i>Range update rate</i>
Δf_s	<i>SFCW frequency step size</i>
$\eta_{1,2}$	<i>Intrinsic wave impedance</i>
$\epsilon_{1,2}$	<i>Electric permittivity</i>
$\mu_{1,2}$	<i>Magnetic permeability</i>
$\Gamma_{\perp,\parallel}$	<i>Fresnel reflection coefficient</i>
$\gamma_{1,2}$	<i>Wave propagation constant</i>
w_n	<i>Additive white Gaussian noise</i>
P_t	<i>Transmit power</i>
$\sigma_{s_{1,2}}$	<i>Static conductivity</i>
M	<i>Number of Prony exponentials to fit</i>
m	<i>Number of nonzero elements in diagonal of Prony data matrix</i>

CHAPTER 1

1. INTRODUCTION

The satellite-based global position system (GPS) enables accurate navigation across the globe when an unobstructed view of the sky is available and radio interference is minimal. Pedestrian navigation scenarios are often in environments where GPS is known to be unreliable such as indoors, underground, near large structures and under thick foliage cover. Additionally, military navigation applications may involve situations where GPS is actively jammed. For these reasons, pedestrian navigation technologies are being developed that are functional in GPS-denied environments.

While there are many examples of pedestrian navigation solutions under development, generally they fall into two categories: infrastructure reliant and self-sufficient. Infrastructure based systems are similar to GPS and require beacons to be placed in known locations prior to navigation. Notable examples include WPI's personnel locator [1] and Q-Track's near-field locator [2] that use radio frequency (RF) beacons for navigation. Self-sufficient solutions are typically realized through inertial navigation and have the advantage of unrestricted movement, not limited by the working range of a beacon. Inertial measurement units (IMUs) integrate local accelerations and rotations to track position and orientation. The development of micro-electromechanical systems (MEMS) technology IMUs has led to compact devices suitable for pedestrian use. Recent examples by Foxlin [3] and

Borenstein [4] mount IMUs on the pedestrian’s shoes allowing for more robust signal processing. The disadvantage of self-sufficient inertial navigation is that navigational error accumulates the longer the system is in use whereas infrastructure systems generally have fixed error bounds.

MEMS IMUs have a significant drawback in that their internal biases are not stationary or predictable which can lead to large positioning errors over time. Both Foxlin [3] and Borenstein [4] use a zero-velocity update (ZUPT) to measure and remove these biases. A ZUPT operation measures the IMU when stationary yielding readings of acceleration bias and gravity. IMUs mounted on the shoe experience zero-velocity periods whenever a shoe is fixed on the ground. Ideally, an inertial navigation algorithm that incorporates ZUPTs can convert a cubic-in-time error growth of a free running IMU to linear in the number of steps [3]. For long-term navigation, ZUPTing alone is insufficient for maintaining accuracy due to uncorrected heading drift.

In [5], Brand and Phillips showed through simulations that adding a measurement of the scalar range between each shoe can decrease the navigational error growth by an order of magnitude over ZUPTing alone. The range measurement can be made throughout the entirety of the step, rather than only at zero-velocity, and directly corrects integrated position error growth in the direction of travel. This prediction was experimental proven by Laverne et al. [6] using an acoustic ranging sensor with a few cm accuracy to provide the scalar range between shoes. Even greater performance is expected if multiple ranges to different locations on the shoe are available as the heading drift will become observable.

A Shoe Ranging Sensor (SRS) has a unique set of challenges due to its placement on the foot. During walking, a shoe experiences large changes in velocity and orientation. The maximum range of the sensor is of order 1 m when the shoes are furthest apart yet ranging accuracy is desired to be around a few mm, [5], leading to a high dynamic range. The sensor’s proximity to the ground as well

as the ground material can significantly reduce accuracy. Environmental contaminants such as mud and dust will also degrade sensor performance. All these concerns point towards the need of a purpose-built sensor to address the needs of an SRS.

This thesis will focus on the design of a Shoe Ranging Sensor that addresses the unique challenges experienced on the foot. Existing ranging solutions are not well suited to the dynamic and close range environment between shoes. This dissertation proposes that stepped frequency continuous wave (SFCW) one-way radar will fill the technology gap and provide an SRS solution with accuracy of under 1 cm RMS over a 1 m range. Furthermore, an extension of the SRS design to generate multiple ranges will be developed.

The organization of the thesis is as follows. Ranging requirements, available technologies and theoretical performance limitations will be discussed in Chapter 2. A 2-ray channel model incorporating polarization effects of arbitrarily oriented antennas is developed in Chapter 3. Algorithms for computing range, including Fourier and parametric techniques, are presented in Chapter 4. A Matlab based channel simulator is developed and tested with IMU data in Chapter 5. The hardware designed for the SRS is described in Chapter 6. Finally, the performance of the SRS is tested on a motion stage with different ground surfaces and compared with simulation in addition to walking tests with a pedestrian in an indoor environment in Chapter 7.

CHAPTER 2

2. RANGING TECHNOLOGY

Measurement science has developed a wide variety of techniques for estimating distance, or ranging, between two objects. Acoustic, optical and radio frequency (RF) methods have been developed and are all capable of high accuracy given the right environment. All these techniques fundamentally rely on the finite wave velocity within a medium: optical and RF are limited by the speed-of-light, and acoustic is limited by speed-of-sound. Through direct measurement or inference of the propagation delay of waves through a medium, the range is determined through the classic equation $R = c\tau_D$, where c is the in-medium wave velocity and τ_D is the propagation time delay.

This chapter will discuss the limitations of acoustic and optical ranging methods in contrast to RF approaches in the context of ranging between shoes. The ranging performance requirements on the shoe will be described. A discussion of RF ranging approaches will follow focusing on accuracy and architecture complexity.

2.1. METHODS

2.1.1. ACOUSTIC

Acoustic ranging, sometimes called SODAR (Sonic Detection And Ranging), uses acoustic waves to measure distance. Modern sodar has origins in 1946 with atmospheric experiments

performed by Gilman, Coxhead and Willis [7]. Acoustic ranging measures distance through either the accumulated phase of a transmitted wave or by the time delay of a modulated waveform such as a pulse. Small, ultrasonic ranging sensors have been designed that show promise for mounting and ranging between shoes [8]. However, ultrasonic sensors are highly degraded when covered by environmental contaminates commonly encountered by pedestrians, such as dirt or mud, as well as wave speed variations (and thus range variation) due to temperature and humidity [9].

2.1.2. OPTICAL

Optical ranging is commonly known as LIDAR, Light Detection And Ranging, and uses light wave propagation to determine distance. Lidar was developed in the 1930s while studying the upper atmosphere [10]. Optical ranging can use accumulation of phase from light wave propagation, but primarily uses the timing of a pulsed waveform to estimate range. Lidar sensors can be made small with high accuracy. However, the presence of dust/fog or dirt on the sensors severely degrades or disables the sensors due to signal absorption or diffusion [11].

2.1.3. RADIO FREQUENCY

RF ranging is typically referred to as RADAR, Radio Detection And Ranging, and uses RF wave propagation in measuring distance. The first RF ranging device was developed by Lee de Forest in 1904 [12]. Radar sensors detect range by measuring the phase change or time delay of a modulated pulse after RF propagation. At microwave frequencies (1m to 1mm wavelength) RF ranging is capable of providing high accuracy with antennas small enough to be mounted on a shoe. As compared to lidar and sodar, small amounts of dirt/mud as well as dust/fog that may be encountered by a pedestrian are fairly transparent to microwaves [11]. Consequently, RF ranging is the chosen technology as it is better suited for the shoe-to-shoe environment.

2.2. TECHNICAL REQUIREMENTS

A shoe mounted RF ranging sensor is ideally small in size and has low power consumption for practical use. The sensor should be small to avoid impeding normal walking and preferably be conformal with the shoe. Power consumption must be low enough that a small lightweight battery or kinetic energy harvesting may be used for power. Design goals to meet these constraints are a target volume of <10 cc and <1 W for an RF ranger built from commercial-off-the-shelf (COTS) components. This work is primarily focused on proof-of-concept development, thus, strict adherence to this specification is not as important as choosing an architecture capable of meeting these goals. An operating frequency between 5-10 GHz (6-3 cm wavelength) is a good choice because the relatively small wavelength will lead to compact antennas. Additionally, the frequency is not so high that the microwave circuits are power inefficient.

The required ranging performance can be estimated by analyzing inertial data from walking. In Fig. 2.1, data from IMUs mounted on each shoe of a person walking at ~ 0.8 m/s is shown. In part (b) and (d) of Fig. 2.1 the range and range velocity between shoes is shown for two different sets of antenna locations. R1 is for a pair of antennas both located at the back of the shoes near the heel. R2 has the left shoe antenna located near the heel as before, however the right shoe antenna is located near the toe. This produces different range profiles with R1 creating a sine-like shape and a peak of about 0.65 m and R2 generates a lopsided sine with peak ~ 0.9 m. Allowing for variation in step size, the radar will need an operating range of about 1 m. Range velocity from R1 and R2 are relatively similar, with both peaking at about 3 m/s. This velocity will develop a Doppler shift of up to 100 Hz at 10 GHz. Depending on the operating frequency, the ranger will need an update in excess of 100 Hz to fully capture the Doppler shift and range variations during a step. Currently, walking tests for the navigation algorithm have used an in-house acoustic ranger with a few cm RMS

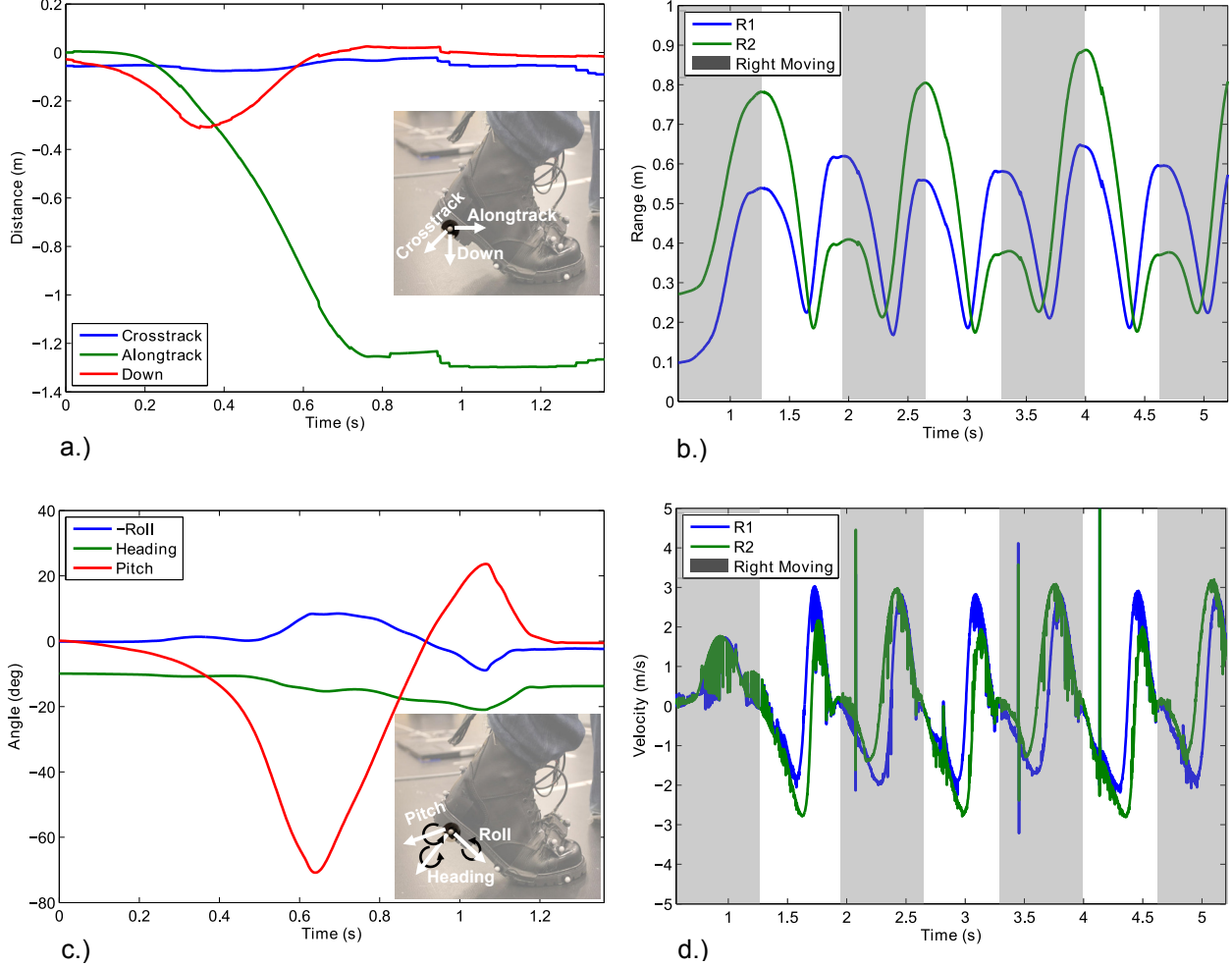


Fig. 2.1. IMU data of a single step of right foot: position (a) and orientation (c). Computed range (b) between two antennas and corresponding range velocity (d). Gray highlighted regions indicate right shoe is moving (left is fixed). R1 is between antennas both located at the back of the shoe; R2 is between front on right shoe and back on left shoe.

(root mean square) accuracy to supply the range [6]. The desire for this RF ranger is to have an order of magnitude improvement in accuracy, or a few mm RMS accuracy.

In Table 2.1, several different commercial RF ranging technologies are compared. Commercial systems are capable of providing centimeter grade accuracy though most are not designed for close ranges within a meter. There is currently a technology gap in providing sub-cm grade ranging in a close one meter range. Furthermore, none of the existing commercial rangers that operate without GPS are designed to perform close to the ground with a high update rate or can provide relative

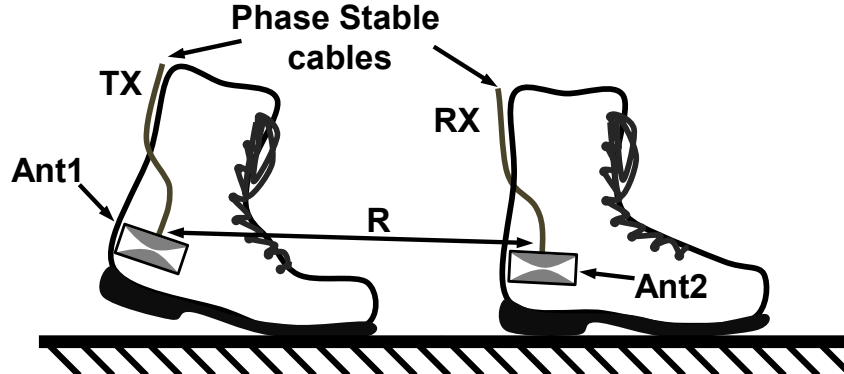


Fig. 2.2. SRS concept: antennas are located on each foot with phase stable RF cables to a backpack mounted transceiver.

heading information. The SRS ranger requirements necessitate the development of a new RF ranger to fill this gap.

Product	Technology	Accuracy	Range	BW	f_R	Heading
Novatel OEM6 [13]	GPS	1.2 m	>>km	41MHz	100 Hz	N
Novatel OEM6 [13]	DGPS	0.4 m	>>km	41MHz	100 Hz	N
Novatel OEM6 [13]	RT-2 GPS	1 cm	>>km	41MHz	100 Hz	N
Astyx MRS 77 [14]	FMCW	0.5 m/5%	1-50 m	490 MHz	>10 Hz	N
Astyx SRS 77 [14]	FMCW	5 cm/5%	0-5 m	900 MHz	>10 Hz	N
Time Domain P400 RCM [15]	UWB	3.5 cm	0.1-354 m	2.2 GHz	<40 Hz	N
SRS Ranger	?	1 mm	0-1 m	1.5 GHz	>100 Hz	N
SRS Multi-Ranger	?	1 mm	0-1 m	1.5 GHz	>100 Hz	Y

Table 2.1. Comparison between a selection of existing RF ranging technologies with requirements of the SRS Ranger and Multi-Ranger (see section 2.3.6).

2.3. RF RANGING

The concept for the SRS ranger is a transmit antenna on one shoe and a receive antenna on the other as shown in Fig. 2.2. An RF cable connects each shoe's antenna to a backpack mounted transceiver and is a high quality phase stable type to minimize ranging errors from cable motion. One antenna is connected to the transmitter and the other to a receiver. In contrast to traditional radar where range is computed from a signal reflected off of a target, the SRS range is the distance R between antennas. This means that range calculations for the SRS will differ from traditional radar by a factor of 2 because the signal only propagates through the RF channel once. Another important

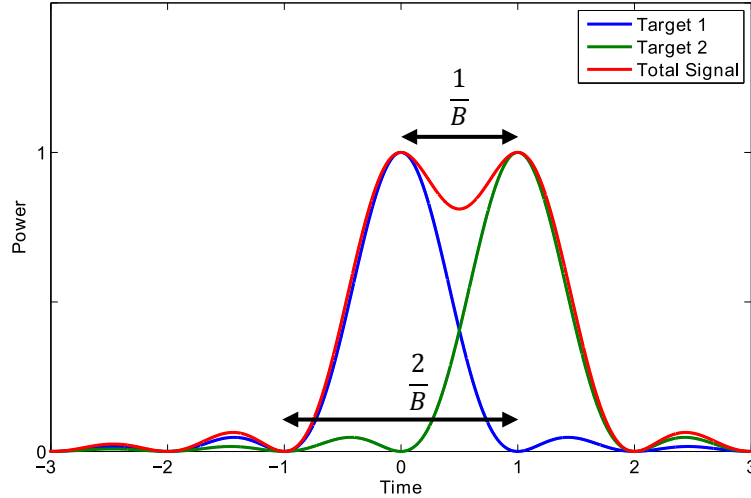


Fig. 2.3. Radar resolution, with bandwidth B , of two closely spaced targets.

difference between the SRS and radar is that radars generally need to be designed to identify multiple targets. The SRS can typically expect a single target (the other shoe/antenna) within its operating range. This means that the traditional concept of radar resolution limited by bandwidth is less important than the measurement accuracy in the presence of noise.

2.3.1. RESOLUTION AND ACCURACY

Radar resolution is defined as the ability of the system to identify two closely spaced targets. Consider modulated (in this case pulsed) radar with single-sided bandwidth (SSB) B that transmits a single pulse and then receives the reflected signal from two targets. Modeling the returns as incoherent signals with a sinc function envelope, the individual power envelopes add as in Fig. 2.3. It is clear that the two targets can be resolved if they are spaced by at least $1/B$ in time, placing the second peak at the minimum of the first. Much closer, and the power envelopes will merge to form a single peak. The range resolution limit is then

$$\delta R = \frac{c}{2B}, \quad (2.1)$$

where the $\frac{1}{2}$ factor comes from the pulse traveling through the channel twice. This resolution limit is sometimes referred to as the Rayleigh criterion because of the similarity to the optical definition of resolving two closely spaced fringes [16].

The SRS configuration increases equation (2.1) by a factor of two because the signal travels through the channel once. However, it is not yet clear from this discussion how much bandwidth will be needed for the SRS. Considering the shoe-to-shoe geometry and typical walking conditions, the radar view between shoes is unimpeded. There may be signal reflections at reduced intensities off the ground and a nearby surface such as a wall or ceiling (multipath). These multipath components add to the desired signal, corrupting the range measurement if they are not resolved.

The ground reflection path may only differ in length by 1 cm during parts of the step which will require ~ 30 GHz of bandwidth to resolve. This large amount of bandwidth is currently impossible to consider for low power architectures and more advanced processing may be required to reduce the effects from the ground reflection. The next closest reflection might be a wall and typically is $\geq 1/3$ m away. If the shoes are at their largest separation (~ 1 m), the path length of a signal off the wall is ~ 1.2 m (Pythagorean's theorem). To resolve the path length difference (0.2 m) and reject the wall reflection, a bandwidth of 1.5 GHz is needed. This bandwidth is within reason for low power circuits.

Radar accuracy is the ability to estimate range in the presence of noise. In the absence of multiple targets, as with the SRS, it is the theoretical limit to ranging performance. For the radar types to be discussed in the following sections (continuous wave and frequency modulated), range accuracy is affected by phase error and time delay error.

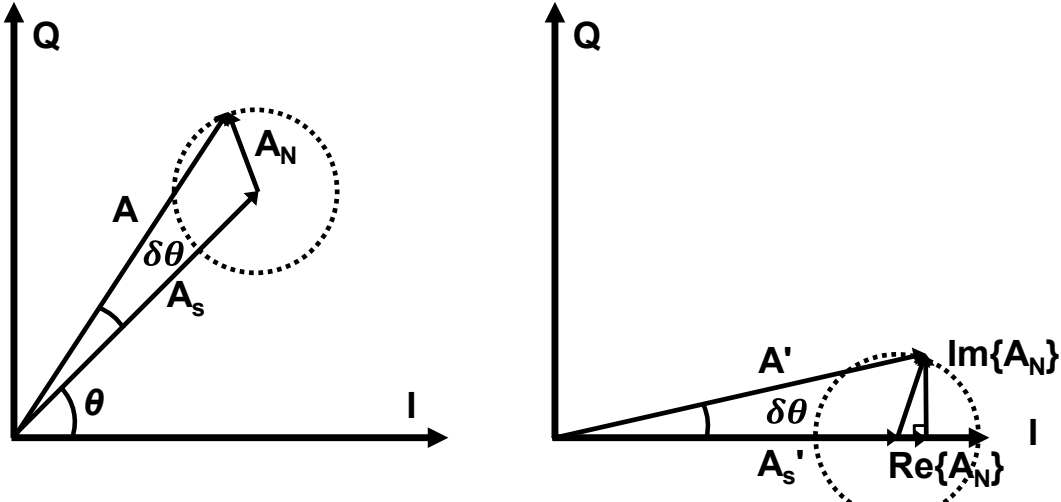


Fig. 2.4. Phasor A_s corrupted with random noise A_N (left). Phasor with average angle, θ , removed and components of noise vector shown (right).

2.3.1.1. RMS PHASE ERROR

\mathbf{A} is a sinusoidal signal (magnitude A_s , phase θ) represented in phasor domain (phasors notated in bold) and corrupted by complex additive white Gaussian noise (AWGN, \mathbf{A}_N) with power σ^2 (Fig. 2.4)

$$\mathbf{A} = \mathbf{A}_s + \mathbf{A}_N = A_s e^{j\theta} + \mathbf{A}_N \quad (2.2)$$

$$P_N = \sigma^2 \quad (2.3)$$

$$SNR = \frac{A_s^2/2}{\sigma^2} \quad (2.4)$$

$$\mathbf{A}_N = \sqrt{\frac{P_N}{2}} [X + iY] \quad (2.5)$$

where SNR (signal-to-noise ratio) is the ratio of RMS signal power ($A_s^2/2$) to RMS noise power, and X and Y are independent random variables with normal distribution (mean=0, variance=1). To find the RMS of the phase error $\delta\theta$ under conditions of moderate to large SNR, it is convenient to first remove the mean angle θ ($\mathbf{A}/e^{j\theta} \rightarrow \mathbf{A}'$), placing \mathbf{A}_s on the in-phase axis (\mathbf{A}'_s). The phase error is then

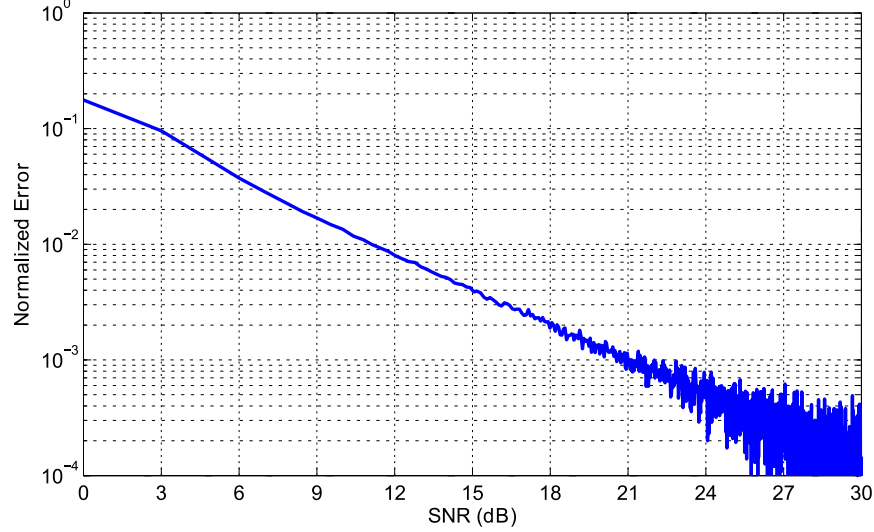


Fig. 2.5. Normalized error of approximation to sampled RMS phase error $\delta\theta$.

$$\delta\theta = \text{atan} \left(\frac{\text{Im}\{A/e^{j\theta}\}}{\text{Re}\{A/e^{j\theta}\}} \right) = \text{atan} \left(\frac{\text{Im}\{A_N\}}{\text{Re}\{A_s/e^{j\theta} + A_N/e^{j\theta}\}} \right) \quad (2.6)$$

At low SNR, (2.6) is known to have a uniform distribution $[-\pi, \pi]$ from the arctangent function [17]. For high SNR, it will be shown that the distribution of (2.6) converges to Gaussian.

If $A_s \gg A_n$ (high SNR), then the small angle approximation can be applied resulting in

$$\delta\theta \approx \frac{\text{Im}\{A_N\}}{\text{Re}\{A_s/e^{j\theta} + A_N/e^{j\theta}\}} = \frac{Y\sqrt{P_N/2}}{A_s} \quad (2.7)$$

The RMS value of the phase error under high SNR is

$$\delta\theta^{RMS} \approx \sqrt{\text{VAR}\left(\frac{Y\sqrt{P_N/2}}{A_s}\right)} = \sqrt{\frac{\text{VAR}(Y\sigma/\sqrt{2})}{A_s^2}} = \sqrt{\frac{\sigma^2/2}{2\sigma^2 SNR}} = \frac{1}{\sqrt{4SNR}}, \quad (2.8)$$

where $\text{VAR}()$ is the variance function. Comparing this approximation with the sampled standard deviation (equal to RMS for zero mean signals), the normalized approximation error for $\delta\theta$ is defined as

$$\text{error}_{\delta\theta} = \left| \frac{\text{std}(\text{angle}(A)) - 1/\sqrt{4SNR}}{\text{std}(\text{angle}(A))} \right| \quad (2.9)$$

and has $<10\%$ error for $\text{SNR} \geq 2.85$ dB and $<1\%$ for $\text{SNR} \geq 11.1$ dB (Fig. 2.5). Functions `std()` and `angle()` compute the standard deviation and polar angle. The noise at high SNR in Fig. 2.5 is due to the finite size of the A_N signal limited by computer memory (2^{25} samples). Thus, for $\text{SNR} > 3$ dB the continuous wave (CW) phase error distribution is Gaussian.

IMPACT OF OSCILLATOR PHASE NOISE

In addition to AWGN, phase noise from the reference oscillator can add to the phase error. High accuracy ranging uses coherent detection and requires that the phase of the transmitting oscillator be stable long enough for comparison with the received signal. The concept of coherence time and length from optics [16] is useful in estimating the stability requirements of an oscillator. Coherence time is defined as the temporal interval over which the phase of a wave is correlated. For radar operating over short distances, the coherence time τ_c needs to be much greater than the max time delay (R_{max}/c) for the impact on range error to be negligible ($\tau_c \gg 3.33$ ns for a max range of 1 m). A narrowband source with spectral width δf (-3 dB points), has a coherence time

$$\tau_c = 1/\delta f. \quad (2.10)$$

Oscillator phase noise is typically specified in noise power $\mathcal{L}(\Delta f)$ relative to peak power at some frequency Δf off the fundamental f_0 . Near f_0 and assuming a Lorentzian lineshape, the spectral width δf is related to $\mathcal{L}(\Delta f)$ by [18]

$$\mathcal{L}(\Delta f) = \frac{1}{2\pi} \frac{\delta f}{\delta f^2/4 + \Delta f^2}, \quad (2.11)$$

and can be solved for spectral width

$$\delta f = [\pi \mathcal{L}(\Delta f)]^{-1} \pm \sqrt{[\pi \mathcal{L}(\Delta f)]^{-2} - 4\Delta f^2}. \quad (2.12)$$

COTS voltage-controlled oscillators (VCOs) in the 5-10 GHz range from Hittite Microwave have about -50 dBc/Hz of phase noise with $\Delta f = 1$ kHz. From (2.12) and (2.10), $\delta f = 63.6$ kHz and

$\tau_c = 15.7 \mu s \gg 3.33 \text{ ns}$. The coherence times of unstabilized VCOs in the 5-10 GHz range are therefore sufficiently stable to have negligible contribution to phase error.

2.3.1.2. RMS TIME DELAY

A finite bandwidth radar pulse in the presence of noise can be shown to have a time delay estimation error of [19]

$$\delta\tau_D^{RMS} = \frac{1}{\beta\sqrt{E/(N_0/2)}} = \frac{1}{\beta\sqrt{2E/N_0}} \quad (2.13)$$

where β is the effective or RMS bandwidth, E is the signal energy (defined in (2.14)) and N_0 is the noise power per unit bandwidth (factor of 2 is because N_0 is defined for positive frequencies). It is derived from the Cramér-Rao Lower Bound (CRLB). β is related to spectral bandwidth and is defined as

$$\beta^2 = \frac{\int_{-\infty}^{\infty} (2\pi f)^2 |S(f)|^2 df}{\int_{-\infty}^{\infty} |S(f)|^2 df} = \frac{(2\pi)^2}{E} \int_{-\infty}^{\infty} f^2 |S(f)|^2 df. \quad (2.14)$$

Here, $S(f)$, is the video spectrum of the radar pulse with mean frequency at 0 Hz and total energy E . RMS bandwidth is larger than spectral bandwidth and can be increased by noting that (2.14) favors energy at the spectral extents rather than near zero.

The ratio $2E/N_0$, or signal-to-noise energy ratio, can be related to the more traditional SNR definition (RMS signal power to RMS noise power ratio) when the received signal is processed with a matched filter. A matched filter has a transfer function that is the complex conjugate of the transmitted signal which maximizes the peak SNR at the output of the filter. For radar waveforms with RMS signal power S over the duration of the transmission τ and RMS noise power N from filter bandwidth B [20],

$$\frac{2E}{N_0} = \frac{2S\tau}{N/B} = 2B\tau \frac{S}{N} = 2B\tau SNR. \quad (2.15)$$

Here, $B\tau$ is the time-bandwidth product that, with appropriate waveform parameters, can greatly increase SNR through processing gain.

2.3.2. CONTINUOUS WAVE RADAR

The simplest ranging system is continuous wave or CW radar and is also capable of the highest range accuracy. In this system, a reference oscillator continuously transmits a wave of single frequency. The transmitted wave will travel a distance through the channel, accumulating phase. Comparing the received wave to the transmitted wave and calculating the phase difference, the range may be calculated as

$$R = \lambda \left(\frac{\theta}{2\pi} + n \right) \quad (2.16)$$

where λ is the wavelength defined as c/f , f is the operating frequency, θ ($0-2\pi$) is the measured phase difference and n is the integer number of wavelengths between the shoes. For a CW radar up to 10 GHz at a range of 1 m, n can be greater than 30 between the shoes. This is known as the wavelength ambiguity problem because the receiver only measures θ and not n (see Fig. 2.6) [19]. For ranging scenarios beyond one wavelength, a modulated waveform rather than CW is commonly used to control ambiguities.

The range accuracy of CW radar in terms of the SNR can be defined using phase error (2.8) in (2.16)

$$\delta R_{CW}^{RMS} = \frac{\lambda}{2\pi} \sqrt{\frac{1}{4SNR}} \quad (2.17)$$

As an example, if the CW radar operates at 7.5GHz ($\lambda = 4$ cm) and the required range accuracy is 1 mm RMS, an SNR of greater than 10.1 dB is required. However, a 4 cm wavelength results in

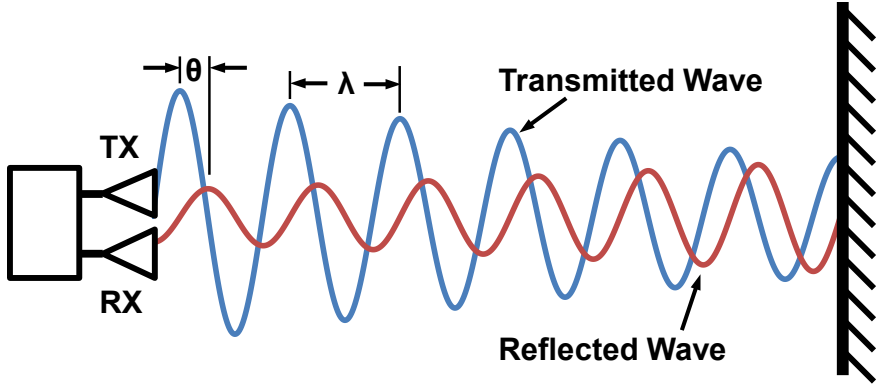


Fig. 2.6. CW radar with range ambiguity. Note topology is different than SRS with transmitted wave reflecting off of a target.

ambiguous distance measurements over the 1 m required range as there can be up to 25 wavelengths between the shoes. If a 1 m wavelength ($f = 300$ MHz) is used instead to avoid ambiguities (i.e. $n=0$), then a very high SNR of over 38 dB is required to maintain accuracy. Furthermore, efficient antennas for a 1 m wavelength are large (~ 0.5 m) and limit the close range performance due to near field effects.

The Doppler shift ($\Delta f_D = f\nu/c$, where ν is the velocity) of a CW signal arises from the changing signal phase when range is a function of time. Equations (2.18)-(2.20) show a derivation of the Doppler effect from a range signal $R(t)$ that moves with constant radial velocity ν and initial position r_0 .

$$S(f, t) = A \cos(2\pi f t + \phi), \quad (2.18)$$

$$\phi = \frac{2\pi}{\lambda} R(t) = \frac{2\pi f}{c} (r_0 + \nu t), \quad (2.19)$$

$$S(f, t) = A \cos(2\pi f t (1 + \nu/c) + 2\pi f r_0/c). \quad (2.20)$$

At 7.5 GHz the expected Doppler shift is 75 Hz for 3 m/s peak velocity. With homodyne detection, the minimum sampling rate for analog-to-digital converters (ADCs) is $2\Delta f_D$ (Nyquist). In practice, it is better to sample much higher than this for high data fidelity and excursions beyond the measured peak velocity. The navigation system that the SRS will interface to operates its inertial measurement

sensors at 600 Hz. A range rate f_R of 600 Hz is greater than the Nyquist requirement and is a convenient number for synchronizing the sensors.

Noting that CW range error (2.17) is proportional to $1/f$ and the error for modulated radar (2.13) is proportional to $1/\beta$, it is easier to increase frequency rather than bandwidth to minimize range error for a given SNR ($2E/N_0$ for modulated radar). Increasing bandwidth generally requires power hungry wideband components. A hybrid system, leveraging the high accuracy of CW ranging with modulation to resolve wavelength ambiguities, can be a highly efficient method for maximizing accuracy and minimizing power.

2.3.2.1. HYBRID RANGING AND ACCURACY

Defining a modulated radar range solution as R_{coarse} and the hybrid CW range as R_{fine} , the two solutions can be combined by taking the floor of the coarse range normalized to the CW wavelength to find n in (2.16)

$$R_{fine} = \lambda \left(\frac{\theta}{2\pi} + \left\lfloor \frac{R_{coarse}}{\lambda} \right\rfloor \right). \quad (2.21)$$

While the CW range accuracy needs to be the same as R_{fine} , the coarse range accuracy is reduced as it is used to determine n . A more formal accuracy requirement on R_{coarse} can be made by considering $R_{coarse}/\lambda = n + Z$ where Z is a Gaussian random variable with mean μ and variance σ^2 . If μ is allowed to vary between 0-1 (i.e. the mean is restricted to be within the correct n), then the total probability that the correct wavelength is chosen is

$$P_\lambda = \frac{\int_0^1 [F_Z(1) - F_Z(0)] d\mu}{\int_0^1 [F_Z(\infty) - F_Z(-\infty)] d\mu}, \quad (2.22)$$

where $F_Z(x)$ is the cumulative distribution function (CDF) of Z evaluated at x . The CDF of Z is a function of μ and (2.22) can be rewritten in terms of the error function $\text{erf}\left(\frac{z-\mu}{\zeta\sqrt{2}}\right)$ while also noting that the denominator is 1

$$\begin{aligned} P_\lambda &= \int_0^1 \left[\frac{1}{2} + \frac{1}{2} \text{erf}\left(\frac{1-\mu}{\zeta\sqrt{2}}\right) - \frac{1}{2} - \frac{1}{2} \text{erf}\left(\frac{0-\mu}{\zeta\sqrt{2}}\right) \right] d\mu \\ &= \frac{1}{2} \int_0^1 \left[\text{erf}\left(\frac{1-\mu}{\zeta\sqrt{2}}\right) - \text{erf}\left(\frac{-\mu}{\zeta\sqrt{2}}\right) \right] d\mu. \end{aligned} \quad (2.23)$$

From Wolfram Mathematica 7, the integral of the error function is

$$\begin{aligned} &\int_0^a \text{erf}\left(\frac{c-\mu}{b}\right) d\mu \\ &= \frac{b}{\sqrt{\pi}} \left[e^{-c^2/b^2} - e^{-(a-c)^2/b^2} \right] + (c-a) \text{erf}\left(\frac{a-c}{b}\right) + c \text{erf}\left(\frac{c}{b}\right). \end{aligned} \quad (2.24)$$

Inserting (2.24) into (2.23), the probability of choosing the correct wavelength is

$$P_\lambda = \sqrt{\frac{2}{\pi}} \zeta \left(e^{-1/2\zeta^2} - 1 \right) + \text{erf}\left(\frac{1}{\sqrt{2}\zeta}\right). \quad (2.25)$$

Equation (2.25) may be simplified if $\zeta \leq 0.5$ (i.e. $\delta R_{coarse}^{RMS} \leq \lambda/2$), then the exponential term approaches 0, the error function approaches 1 and

$$P_\lambda \cong 1 - \sqrt{\frac{2}{\pi}} \zeta, \quad (2.26)$$

$$\zeta \cong (1 - P_\lambda) \sqrt{\frac{\pi}{2}}. \quad (2.27)$$

In Fig. 2.7, a comparison between (2.25) and (2.26) is made. The approximation is accurate for $\zeta \leq 0.5$. For a 60% chance that the correct n (wavelength) is chosen, $\zeta = 0.5$ and $\delta R_{coarse}^{RMS} \leq \zeta\lambda = \lambda/2$. If $\zeta = 0.3$, this probability rises to 76%.

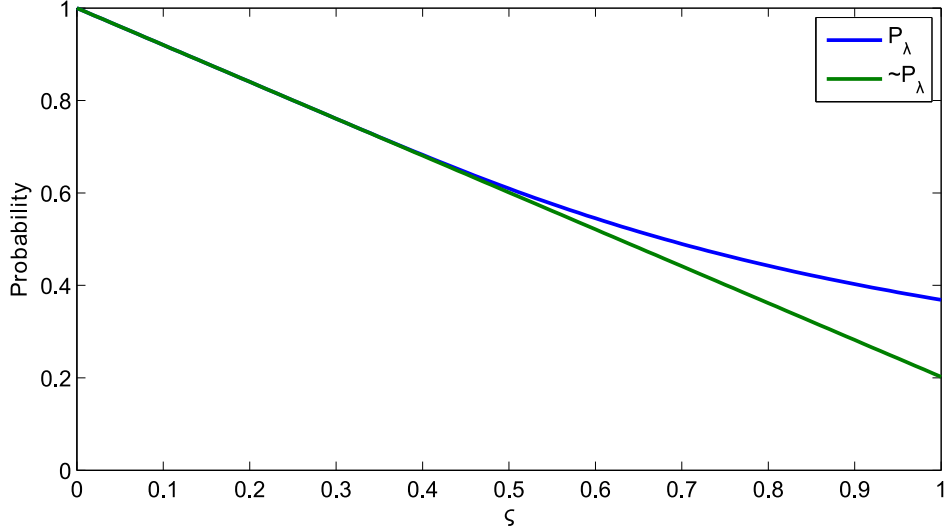


Fig. 2.7. Probability of selecting the correct n given normalized coarse range standard deviation ξ

The most convenient modulation scheme for providing R_{coarse} is one whose architecture can easily support CW transmission as well for hybrid ranging. There are two modulation methods that will be discussed and can be adapted to provide CW measurements: frequency-modulated CW (FMCW) and stepped-frequency CW (SFCW).

2.3.3. FREQUENCY MODULATED CONTINUOUS WAVE RADAR

FMCW radar is commonly used in close range and single target systems (such as altimeters [19]). In this method, a VCO is tuned over a bandwidth, B . The VCO is controlled using, for example, a triangle wave such that the frequency is always linearly changing (Fig. 2.8). The triangle wave allows for estimation of the Doppler frequency, [19], and may be easily modified to dwell for CW measurements as shown in Fig. 2.8a. A received signal is multiplied against the transmitted signal to provide a beat frequency Δf_b proportional to the range. The range accuracy for FMCW under optimal conditions is limited by the CRLB (2.13) and is defined with $\beta = \pi B / \sqrt{3}$, [19], as

$$\delta R_{FMCW}^{RMS} = \frac{c\sqrt{3}}{\pi B \sqrt{2E/N_0}}. \quad (2.28)$$

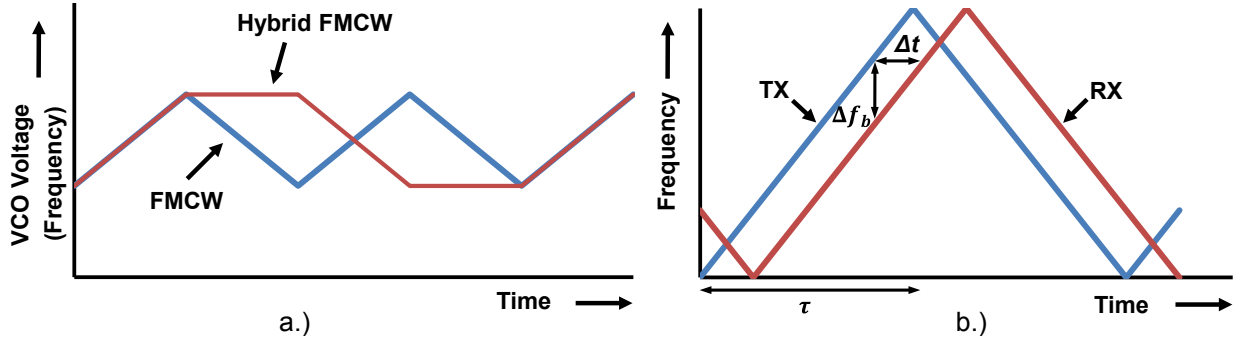


Fig. 2.8. Left (a), VCO tuning waveform for FMCW and hybrid FMCW+CW. Right (b), transmitted and received FMCW waveform. Beat frequency Δf_b is proportional to channel delay Δt .

The SNR-energy equation from (2.15) suggests that maximizing the time-bandwidth product will minimize the FMCW range error when processed with a matched filter. The required bandwidth that meets low power and range resolution constraints is 1.5 GHz as discussed previously. The sweep time τ has yet to be constrained and nominally should be as large as possible to maximize $B\tau$.

The ADC minimum sampling rate required for FMCW depends on the sweep time and the maximum range

$$f_{sampling} \geq 2\Delta f_b|_{max} = 2 \frac{BR_{max}}{c\tau}. \quad (2.29)$$

Range can be computed with a Fourier transform (which provides the matched filter) to identify the beat frequency leading to

$$R_{FMCW} = \frac{c\tau\Delta f_b}{B}. \quad (2.30)$$

Large τ results in small $\Delta f_b|_{max}$ and consequently long integration times are required to determine a Δf_b for an incremental change in R_{FMCW} . The range update rate f_R of 600 Hz determined in section 2.3.2 can also be viewed as a minimum beat frequency allowed. With this assumption, (2.29) is modified to set the maximum sweep time τ

$$\tau \leq \frac{B\Delta R}{c f_R}. \quad (2.31)$$

For $\Delta R = 1$ mm, τ must be less than $8.33 \mu\text{s}$. Setting τ to the nearest power of 10 ($1 \mu\text{s}$), $B\tau$ is 1500. For $R_{max} = 1$ m, the sampling rate required to digitize the highest beat frequency is 10 MHz. Using the same SNR from the CW radar example (10.1 dB) with (2.28) and (2.15), $\delta R_{FMCW}^{RMS} = 0.6$ mm and is capable of the required system accuracy without adding CW ranging. This is because of the processing gain from $B\tau$.

There are some disadvantages to FMCW. Increasing bandwidth requires larger receiver bandwidths and thus faster (and more power hungry) ADCs. Transmitter to receiver signal feedthrough is hard to calibrate and can corrupt range measurements similar to multipath [21]. Also, nonlinearity of the VCO can contribute to range error as the beat frequency for a given range will change over the period of the pulse.

2.3.4. STEPPED FREQUENCY CONTINUOUS WAVE RADAR

Stepped-frequency CW radar is fundamentally a discretized version of FMCW that measures the channel in the frequency domain with N equally spaced in frequency CW measurements [20]. Shown in Fig. 2.9a, a VCO is stepped through N frequencies within a bandwidth B . At each frequency the VCO dwells for τ_s to make a steady-state CW measurement, with a full sweep performed in $\tau = N\tau_s$. The sweep time should be short enough to sample the max expected Doppler shift $(\tau < \frac{1}{2\Delta f_D})$. A short sweep time is also desirable as it minimizes the range change ($v\tau$) during the measurement, approximating a static measurement (when $\tau \ll \frac{1}{2\Delta f_D}$). The minimum ADC sampling rate, assuming one measurement per frequency, is

$$f_{sampling} \geq N/\tau. \quad (2.32)$$

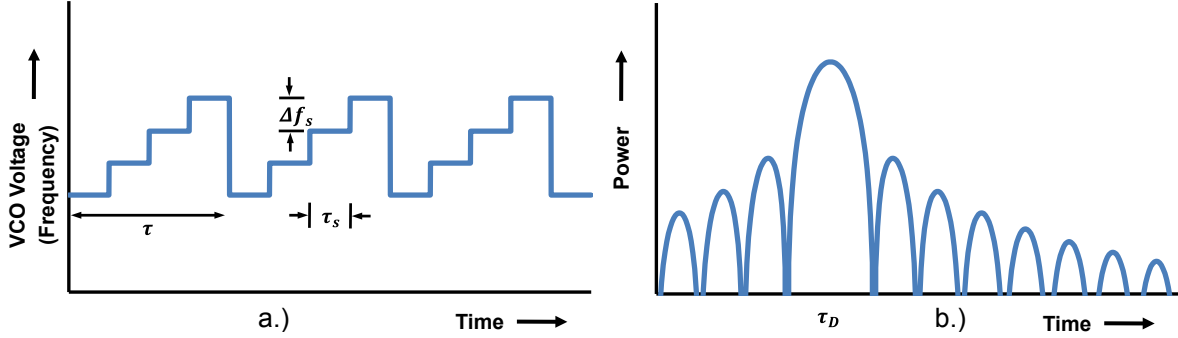


Fig. 2.9. Example VCO tuning waveform for SFCW (a). Fourier transform of SFCW channel data, τ_D is the location of the peak corresponding to target range (b).

Like CW ranging, SFCW experiences range ambiguity from the quantized frequency step size Δf_s at ranges beyond $c/\Delta f_s$. Care should be taken to choose N such that the ambiguity occurs beyond the desired max range. The frequency step size is defined as

$$\Delta f_s = \frac{B}{N-1}. \quad (2.33)$$

SFCW samples the channel in the frequency domain. Through the inverse Fourier transform (also the SFCW matched filter), the time domain impulse response of the channel can be found. For a single target, the time delay τ_D (see Fig. 2.9b) for the power envelope peak corresponds to range

$$R_{SFCW} = c\tau_D. \quad (2.34)$$

The range accuracy for SFCW requires the derivation of effective bandwidth for the CRLB.

2.3.4.1. DERIVATION OF SFCW EFFECTIVE BANDWIDTH

Assuming a total energy E and an equal energy for each of the N CW measurements (constant SNR), the video spectrum of SFCW is

$$|S(f)|^2 = \left| \sum_{n=0}^{N-1} \sqrt{\frac{E}{N}} \delta \left(f - B \left(\frac{n}{N-1} - \frac{1}{2} \right) \right) \right|^2 \text{ for } N \geq 2, \quad (2.35)$$

where $\delta()$ is the Kronecker delta function and approximates a narrowband CW frequency measurement. Inserting (2.35) into (2.14)

$$\beta^2 = \frac{(2\pi)^2}{E} \int_{-\infty}^{\infty} f^2 \left(\left| \sum_{n=0}^{N-1} \sqrt{\frac{E}{N}} \delta \left(f - B \left(\frac{n}{N-1} - \frac{1}{2} \right) \right) \right|^2 \right) df \quad (2.36)$$

Given

$$(\delta(x) + \delta(y))^2 = \delta(x) + \delta(y), \quad (2.37)$$

$$\beta^2 = \frac{(2\pi)^2}{E} \int_{-\infty}^{\infty} f^2 \sum_{n=0}^{N-1} \frac{E}{N} \delta \left(f - B \left(\frac{n}{N-1} - \frac{1}{2} \right) \right) df \quad (2.38)$$

From the delta function translation property,

$$\int_{-\infty}^{\infty} g(x) \delta(x - Y) dx = g(Y) \quad (2.39)$$

$$\begin{aligned} \beta^2 &= \frac{(2\pi)^2}{N} \sum_{n=0}^{N-1} \left(B \left(\frac{n}{N-1} - \frac{1}{2} \right) \right)^2 \\ &= \frac{(2\pi B)^2}{N} \sum_{n=0}^{N-1} \left(\left(\frac{n}{N-1} \right)^2 - \frac{n}{N-1} + \frac{1}{4} \right) \end{aligned} \quad (2.40)$$

Using polynomial summation identities

$$\sum_{i=j}^k 1 = k + 1 - j \quad (2.41)$$

$$\sum_{i=j}^k i = \frac{(k+1-j)(k+j)}{2} \quad (2.42)$$

$$\sum_{i=1}^k i^2 = \frac{k(k+1)(2k+1)}{6} \quad (2.43)$$

$$\begin{aligned}
\beta^2 &= \frac{(2\pi B)^2}{N} \left[\frac{(N-1)(N)(2N-1)}{6(N-1)^2} - \frac{N(N-1)}{2(N-1)} + \frac{N}{4} \right] \\
&= (2\pi B)^2 \left[\frac{(2N-1)}{6(N-1)} - \frac{1}{4} \right] \\
&= (2\pi B)^2 \left[\frac{8N-4-6N+6}{24(N-1)} \right] \\
&= \frac{(\pi B)^2}{3} \frac{N+1}{N-1}
\end{aligned} \tag{2.44}$$

Combining (2.44) with (2.13), the CRLB for SFCW is

$$\delta R_{SFCW}^{RMS} = \frac{c\sqrt{3}}{\pi B \sqrt{2E/N_0}} \sqrt{\frac{N-1}{N+1}}. \tag{2.45}$$

For the same SNR-energy ($2E/N_0$), the SFCW range accuracy can be up to 73% better than FMCW (i.e. $N=2$). This is because the RMS bandwidth heavily weights spectral energy at the extremes. For large N , the spectrum becomes effectively continuous and converges to the FMCW solution. Fig. 2.10 shows the RMS bandwidth versus N for a 1.5 GHz sweep (constant $2E/N_0$). The delta function solution from (2.44) is plotted along with a numeric integration of (2.14) using 1 MHz SSB sampled rect functions to simulate an ADC with 1 MHz of analog bandwidth. The delta function is a good approximation for this sweep and ADC bandwidth.

The time-bandwidth product for SFCW can be determined by considering the waveform to be a series of N pulses each with length τ_s and bandwidth $1/\tau_s$. The overall waveform time is $N\tau_s$ and the bandwidth is N/τ_s leading to $B\tau = N^2$. For constant SNR, this time-bandwidth product counteracts the previously discussed benefit of using lower N because of increased processing gain. For 1.5 GHz bandwidth sweep, the minimum N is 7 to have a unambiguous range interval of 1.2 m ($> R_{max}$). This ambiguity interval is a little close to the region of interest so generally N is increased to add a safety margin. Letting N equal 21 leads to an ambiguity range of 4 m and a $B\tau$ of 441. With a CW SNR of 10.1 dB, $\delta R_{SFCW}^{RMS} = 1.1$ mm and the required sampling rate is 12.6 kHz ($\tau = 1/f_R =$

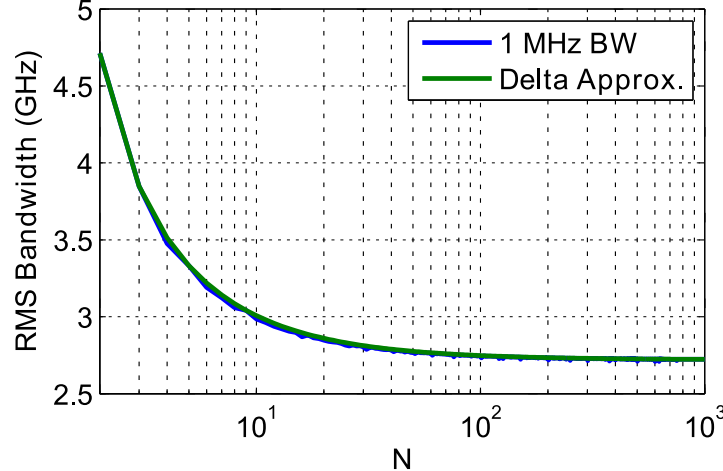


Fig. 2.10. Comparison of RMS bandwidth calculation between delta function approximation and rect function with SSB 1MHz. Sweep bandwidth is 1.5 GHz.

$1/600$ s). With a 1.67 ms sweep time, the maximum ΔR during a sweep is 5 mm at max velocity. The actual range error introduced will be less because each CW measurement is delayed differently. Additionally, the peak velocity periods while walking are short in duration (Fig. 2.1), so brief Doppler induced errors up to 5 mm should not impede achieving sub-cm accuracy. Again, the modulated RMS error is on the same order as the CW error due to processing gain, however this error metric does not consider multipath effects.

The SFCW has some advantages over FMCW. The linearity and feed-through concerns can easily be measured and largely removed using a lookup table. CW phase measurements are natively part of the waveform and are available for hybrid ranging. The ADC sampling rate requirements are drastically reduced which can allow ultra-low power designs with low noise, high bit-depth ADCs. SFCW measures the frequency response of the channel, not just a beat frequency, which may be of use to advanced signal processing.

2.3.5. PERFORMANCE SUMMARY

In the following tables, a comparison is made between the three ranging methods discussed – CW, FMCW and SFCW – presenting the relevant design equations and summarizing the performance metrics from the preceding examples.

Parameter	CW	FMCW	SFCW
Bandwidth	-	B	$B = (N - 1)\Delta f_s$
RMS Bandwidth	-	$\frac{\pi B}{\sqrt{3}}$	$\frac{\pi B}{\sqrt{3}} \sqrt{\frac{N+1}{N-1}}$
Sweep Time	-	$\tau \leq \frac{B\Delta R}{c f_R}$	$\tau = N\tau_s = \frac{1}{f_R} < \frac{1}{2\Delta f_D}$
Time-Bandwidth	-	$B\tau$	N^2
RMS Range Accuracy	$\frac{\lambda}{2\pi} \sqrt{\frac{1}{4SNR}}$	$\frac{c\sqrt{3}}{\pi B \sqrt{2B\tau SNR}}$	$\frac{c\sqrt{3}}{\pi B \sqrt{2N^2 SNR}} \sqrt{\frac{N-1}{N+1}}$
Range	$\lambda \left(\frac{\theta}{2\pi} + \left\lceil \frac{R_{coarse}}{\lambda} \right\rceil \right)$	$\frac{c\tau\Delta f_b}{B}$	$c\tau_D$
Range Ambiguity	λ	$c\tau$	$\frac{c}{\Delta f_s}$
Min sampling rate	$\geq 2\Delta f_D$	$\geq 2 \frac{B R_{max}}{c\tau}$	$\geq \frac{N}{\tau}$

Table 2.2. Design equations for CW, FMCW and SFCW waveforms.

Parameter	CW	FMCW	SFCW
Bandwidth/Frequency	7.5 GHz	1.5 GHz	1.5 GHz
RMS Bandwidth	-	2.72 GHz	2.85 GHz
Sweep Time	-	1 μs	1.67 ms
Time-Bandwidth	-	1500	441
# of Frequencies	1	∞	21
SNR	10.1 dB	10.1 dB	10.1 dB
RMS Range Accuracy	1 mm	0.6 mm	1.1 mm
Range Ambiguity	4 cm	300 m	4 m
ADC Sampling rate	600 Hz	10 MHz	12.6 kHz

Table 2.3. Summary of radar parameters for CW, FMCW and SFCW examples.

Comparing the three ranging examples in Table 2.3, all techniques are capable of providing mm-level ranging, though only FMCW and SFCW are able to achieve this without ambiguity within 1 m. SFCW has a large sampling rate advantage over FMCW and is easier to calibrate out non-idealities of the receiver. In [22], an $N=2$ version of SFCW was used and found that multipath effects near the ground corrupted the range from the SFCW solution. Using a hybrid ranging approach to combine SFCW with CW solutions led to a combined accuracy of 0.92 mm RMS without ambiguity. Given

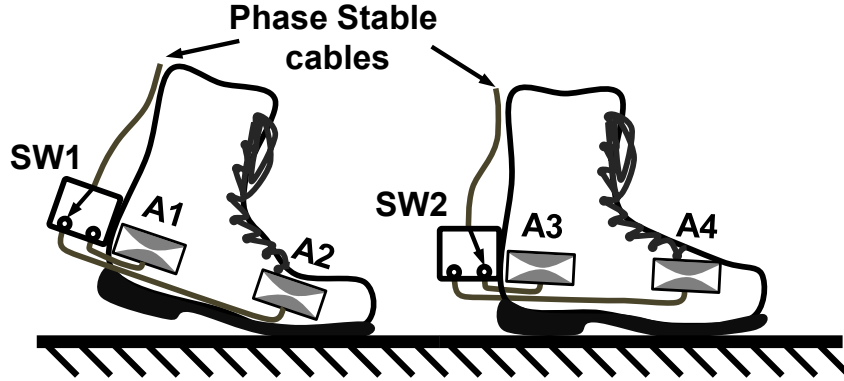


Fig. 2.11. SRS Multi-Ranger concept: 2 antennas on each shoe connect through an RF switch to the backpack mounted transceiver. RF switches select which antenna pair are active (A2 and A3 displayed).

the ADC and calibration advantages of SFCW along with the multipath reduction effects of hybrid ranging, the SRS will use a SFCW+CW waveform. Table 2.4 shows the proposed SRS theoretical performance along with various commercial ranging technologies.

2.3.6. MULTI-RANGER ARCHITECTURE

Simulation [5] and experimental results [6] have found that adding a single range measurement greatly enhanced pedestrian navigation performance through reducing the effects of inertial sensor drift. Potentially, multiple range measurements to different locations on the shoe will enhance this effect by allowing better estimates of relative shoe heading. The proposed SRS architecture can be easily modified to include multiple range measurements by using time-division multiplexing. A single RF phase stable cable runs down to each shoe as before, however at each shoe the cable connects to a high-speed RF switch. The RF switches selects which antenna pair is connected to the transmitter/receiver. With M_S switch positions on each shoe, a total of 2^{M_S} antenna pair combinations are available. Fig. 2.11 shows a concept SRS multi-ranger with $M_S=2$, or 4 possible ranges.

The impact of the RF switch on the SFCW+CW architecture in 2.3.5 can be relatively minimal. The switch control sequentially selects all pair combinations for a multi-ranging cycle and therefore

must be synchronous with the VCO frequency control so that a measurement is correlated to the correct antenna pair. The single range update requirement, $f_R \geq 600$ Hz, leads to two options for integrating multiple ranges: set the multi-range update rate $f_{MR} = 2^M s f_R$ to compute all ranges within the same f_R period, or $f_{MR} = f_R / 2^M s$ where each range is computed sequentially at the same individual rate a single range is made. The second option has the disadvantage of reduced sampling of the Doppler shift, however, it does not require a faster ADC sampling which may allow lower power operation (or increased averaging at higher sampling rates). For $M_S=2$, the update rate of a single range is still 150 Hz which meets the Nyquist criteria to sample a 75 Hz Doppler shift. From a navigation perspective, the use of more measurements is likely more important than having good Doppler estimates. Table 2.4 shows the specifications of the SRS Multi-Ranger in comparison with existing RF ranging technologies shown earlier.

Product	Technology	Accuracy	Range	BW	f_R	Heading
Novatel OEM6 [13]	GPS	1.2 m	>>km	41MHz	100 Hz	N
Novatel OEM6 [13]	DGPS	0.4 m	>>km	41MHz	100 Hz	N
Novatel OEM6 [13]	RT-2 GPS	1 cm	>>km	41MHz	100 Hz	N
Astyx MRS 77 [14]	FMCW	0.5 m/5%	1-50 m	490 MHz	>10 Hz	N
Astyx SRS 77 [14]	FMCW	5 cm/5%	0-5 m	900 MHz	>10 Hz	N
Time Domain P400 RCM [15]	UWB	3.5 cm	0.1-354 m	2.2 GHz	<40 Hz	N
SRS Ranger	SFCW+CW	1 mm	0-4 m	1.5 GHz	600 Hz	N
SRS Multi-Ranger	SFCW+CW	1 mm	0-4 m	1.5 GHz	150 Hz ($M_S=2$)	Y

Table 2.4. Comparison between a selection of existing RF ranging technologies with proposed SRS Ranger and SRS Multi-Ranger.

In summary, RF ranging has the best feature set for the shoe-to-shoe environment. Consideration of the technical merits of several radar techniques has led to the conclusion that SFCW combined with CW ranging is well suited to providing high accuracy and a low-power architecture. Time-division multiplexing allows the extension of SFCW+CW to provide multiple ranges between several antenna pairs mounted on the shoes. The optimal parameters were found to

be 1.5 GHz bandwidth with 21 frequency steps in a 1.67 ms single range sweep time. Four ranges are sequentially made to form a 6.67 ms multi-ranging period with no impact on the required ADC sampling rate.

CHAPTER 3

3. THE CHANNEL

High resolution ranging with electromagnetic waves between a pedestrian's shoes requires careful consideration of the effects of the physical environment, or channel, the waves propagate through. The dynamic nature of the foot and the potential for changing terrain surface properties can lead to a rapidly varying channel. These channel variations may ultimately lead to degraded ranging accuracy during parts of the pedestrian's step or over certain surfaces. Therefore, it is useful to construct a theoretical channel model to assess the accuracy limitations of the SRS in the shoe-to-shoe environment. This model will also allow estimation of required RF specifications of the ranger as well as provide a benchmark to test ranging algorithms.

The typical surface a pedestrian walks on is fairly flat and generally free of objects that would inhibit an electromagnetic line-of-sight (LOS) between shoes. When configured with a transmit antenna on one shoe and a receive antenna on the other, there exist two dominate wave paths (or rays): the LOS and a ground reflected path (Non-LOS or NLOS). Additional wave paths, such as off a wall or ceiling indoors and a tree or rock outdoors, will travel a larger distance and experience more attenuation. Furthermore, with sufficient bandwidth, secondary reflections may be resolved if separated from the maximum shoe-to-shoe range by the radar resolution. A bandwidth of 1.5 GHz can easily reject reflections whose path lengths are >0.2 m from the LOS path length. Therefore, a

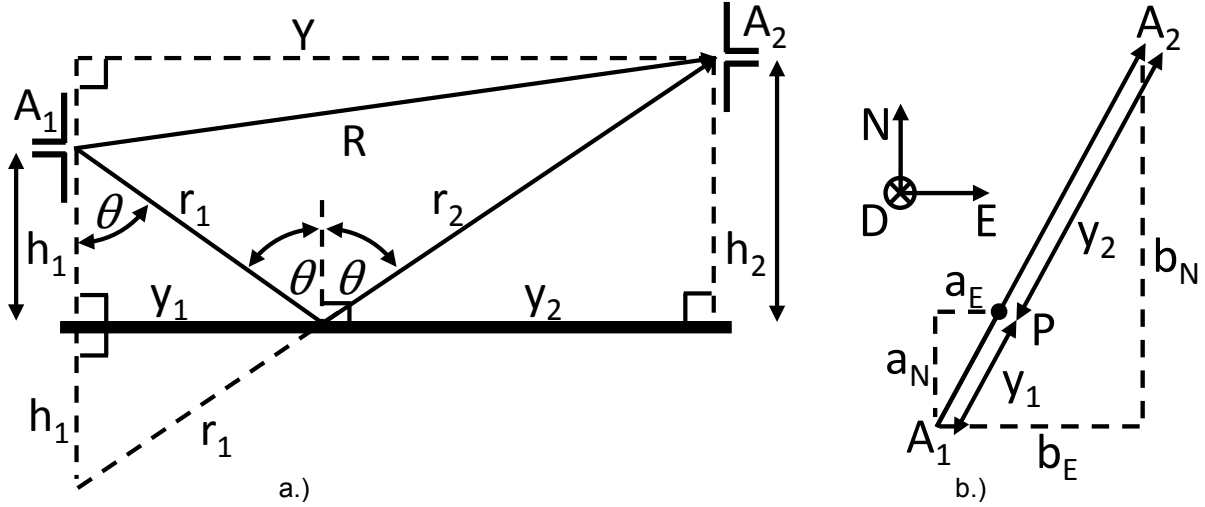


Fig. 3.1. Plane of incidence and geometry for 2-ray flat earth model. Dotted lines aid in defining the geometry (a). Top view and global coordinate system North East Down (b).

2-ray flat earth channel model is an appropriate approximation for the shoe-to-shoe channel during most walking conditions.

This chapter will develop the mathematical framework for modeling the SRS channel. The 2-ray geometry will be described and used in calculation of the received signal after propagation. An electric field version of the Friis propagation equation will also be derived to increase phase accuracy of the model.

3.1. 2-RAY FLAT EARTH MODEL

The geometry for the 2-ray flat earth model [23] is shown in Fig. 3.1 in both the plane of incidence and in the global North East Down coordinate system. Two antennas (A_1, A_2) with respective coordinates (N_1, E_1, h_1) and (N_2, E_2, h_2) have a LOS path with Euclidian distance R and a reflected path $r_1 + r_2$. Following Snell's law of reflection, the reflected path forms the same angle θ referenced off the normal to the reflecting surface. Based on this angle restriction, the NE plane separation distance $Y = \sqrt{b_N^2 + b_E^2}$ and the law of similar triangles, the reflected path r_1 , r_2 and θ can be found with the following equations:

$$y_1 = Y/(1 + h_2/h_1) \quad (3.1)$$

$$y_2 = y_1 h_2/h_1 \quad (3.2)$$

$$r_1 = \sqrt{h_1^2 + y_1^2} \quad (3.3)$$

$$r_2 = \sqrt{h_2^2 + y_2^2} \quad (3.4)$$

$$\theta = \text{atan}(y_1/h_1). \quad (3.5)$$

Given the positions of the antennas, the position P of the ground reflection may be determined.

Relative to A_1 , P is located at (a_N, a_E, h_1) where

$$a_N = b_N y_1 / Y \quad (3.6)$$

$$a_E = b_E y_1 / Y. \quad (3.7)$$

3.2. LOS PROPAGATION

In the far-field of an antenna in free space, where the radiation pattern's angular variations are independent of distance, the available signal power drops off proportional to the inverse square of the distance. For commonly used antennas, the far-field distance criteria is defined as $> 2D^2/\lambda$ where D is the largest dimension of the antenna's radiating elements and λ is the operating wavelength ($\lambda = c/f$ where c is the speed of light and f is frequency). Half-wavelength sized antennas will transition to far-field at about $\lambda/2$ away: at 6 GHz, this distance is about 2.5 cm. Propagation in the far-field is described by the Friis equation [24]

$$P_r = P_t \left(\frac{\lambda}{4\pi R} \right)^2 G_t(\theta_t, \phi_t) G_r(\theta_r, \phi_r) |\hat{\mathbf{p}}_t^r(\theta_t, \phi_t) \cdot \hat{\mathbf{p}}_r^*(\theta_r, \phi_r)|^2 \quad (3.8)$$

where P_r and P_t are the received and transmitted power respectively, R is the propagation distance as in Fig. 3.1, G_t and G_r are the respective transmit and receive antenna gain and $\hat{\mathbf{p}}_t^r$ and $\hat{\mathbf{p}}_r^*$ are the polarization vectors of the antenna. The notation in the equation uses bold to indicate a vector, \wedge denotes a unit vector, $*$ is the complex conjugate and scalars or scalar magnitudes of a vector are not

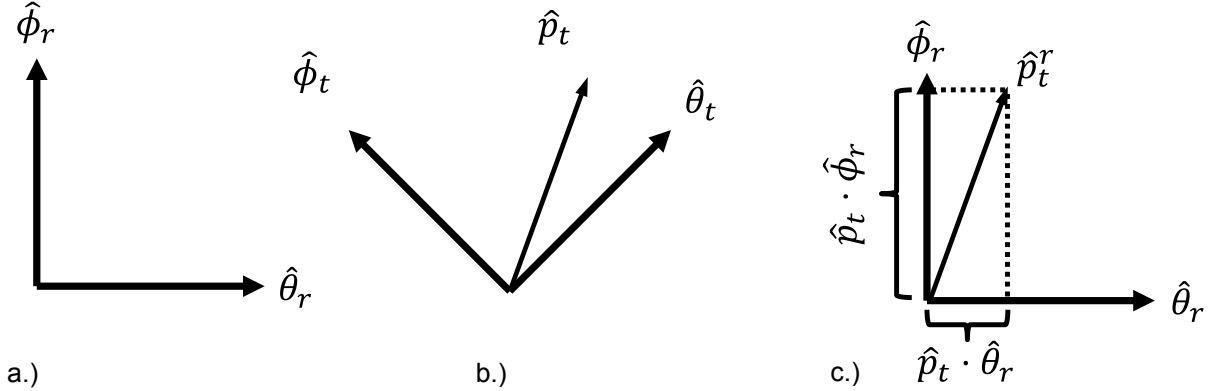


Fig. 3.2. Projection of \hat{p}_t into receive coordinate frame formed by $\hat{\theta}_r, \hat{\phi}_r$ (a). \hat{p}_t in native coordinate frame (b) and resulting \hat{p}_t^r vector in $\hat{\theta}_r, \hat{\phi}_r$ frame (c).

in bold. The r superscript on \hat{p}_t^r indicates that θ_t and ϕ_t components are projected into the coordinate system of the \hat{p}_r^* vector (Fig. 3.2) resulting in

$$\hat{p}_t^r = (p_{\theta_t} \hat{\theta}_t \cdot \hat{\theta}_r + p_{\phi_t} \hat{\phi}_t \cdot \hat{\theta}_r) \hat{\theta}_r + (p_{\theta_t} \hat{\theta}_t \cdot \hat{\phi}_r + p_{\phi_t} \hat{\phi}_t \cdot \hat{\phi}_r) \hat{\phi}_r. \quad (3.9)$$

Gain and polarization are functions of $\theta_{t,r}$ and $\phi_{t,r}$ in the local spherical coordinate system of each antenna. The polarization vector describes the antenna's polarization reference direction and type – linear (real) or elliptical (complex) – in the transmit mode. A conjugate operation is used to convert from transmit to receive mode.

This channel model will use antenna gain and polarization computed by the finite-element simulation package Ansoft HFSS. Polarization and gain can be redefined in terms of the radiated electric field which will be shown to simplify (3.8). The radiated electric field is useful because it includes radiation efficiency and polarization effects. Gain, in terms of radiated electric field [24], is

$$G(\theta_{t,r}, \phi_{t,r}) = \frac{4\pi}{2\eta_1 P_{in}} |r \tilde{\mathbf{E}}(\theta_{t,r}, \phi_{t,r})|^2 = \frac{4\pi}{2\eta_1 P_{in}} [r E(\theta_{t,r}, \phi_{t,r})]^2 \quad (3.10)$$

where η_1 is the intrinsic wave impedance, P_{in} is the power input to the antenna terminals (1 W in HFSS), and $r \tilde{\mathbf{E}}$ is the radiated electric field vector multiplied by radial distance r . The wave impedance is approximately the ratio of the magnetic permeability to the electric permittivity or

dielectric constant ($\sqrt{\mu_1/\epsilon_1}$ - about 377Ω in free space) and is given in more exact form in (3.20).

$r\tilde{\mathbf{E}}$ is the far-field output from HFSS that includes the effects of impedance mismatch (return loss) and is a complex vector (denoted by \sim). The polarization vector is essentially the electric field unit vector and, in terms of the HFSS output, is defined as

$$\hat{\mathbf{p}}(\theta_{t,r}, \phi_{t,r}) = \frac{r\tilde{\mathbf{E}}(\theta_{t,r}, \phi_{t,r})}{rE(\theta_{t,r}, \phi_{t,r})}. \quad (3.11)$$

Combining (3.8)-(3.11), the Friis equation can be redefined with the radiated electric field

$$P_r = P_t \left(\frac{\lambda}{4\pi R} \right)^2 \left(\frac{4\pi}{2\eta_1 P_{in}} \right)^2 [rE_t(\theta_t, \phi_t)]^2 [rE_r(\theta_r, \phi_r)]^2 \left| \frac{r\tilde{\mathbf{E}}_t^*(\theta_t, \phi_t)}{rE_t(\theta_t, \phi_t)} \cdot \frac{r\tilde{\mathbf{E}}_r^*(\theta_r, \phi_r)}{rE_r(\theta_r, \phi_r)} \right|^2, \quad (3.12)$$

$$P_r = P_t \left(\frac{\lambda}{4\pi R} \right)^2 \left(\frac{4\pi}{2\eta_1 P_{in}} \right)^2 |r\tilde{\mathbf{E}}_t^*(\theta_t, \phi_t) \cdot r\tilde{\mathbf{E}}_r^*(\theta_r, \phi_r)|^2. \quad (3.13)$$

The phase of the signal in (3.13) is composed of two parts: propagation and polarization phase. Propagation phase results from the wave traveling a number of wavelengths to the receiver. It is defined for LOS as $2\pi R/\lambda$ or kR where k is the wavenumber. Polarization phase is due to polarization mismatch of the antennas from differing orientations or changing polarization characteristics across the pattern. This phase results from the electric field terms in (3.13) and can be defined as

$$e_{LOS} = r\tilde{\mathbf{E}}_t^*(\theta_t, \phi_t) \cdot r\tilde{\mathbf{E}}_r^*(\theta_r, \phi_r) \quad (3.14)$$

$$\angle e_{LOS} = \text{atan2}(\text{Im}\{e_{LOS}\}, \text{Re}\{e_{LOS}\}). \quad (3.15)$$

For example, using dipole antennas, the polarization is linear and the normalized electric field can be described by the vector $\langle 1 \ 0 \rangle$. If one antenna is inverted with respect to the other, $e_{LOS} = \langle 1 \ 0 \rangle \cdot \langle -1 \ 0 \rangle = -1$ and $\angle e_{LOS} = \pi$, the signal will be 180° out of phase in addition to the propagation phase. Combining these phases with the received power in (3.13) results in the complex LOS signal

$$S_{LOS} = \sqrt{P_t} \left(\frac{\lambda}{2\eta_1 P_{in} R} \right) |r\tilde{\mathbf{E}}_t^*(\theta_t, \phi_t) \cdot r\tilde{\mathbf{E}}_r^*(\theta_r, \phi_r)| e^{j(kR + \angle e_{LOS} + \psi)}, \quad (3.16)$$

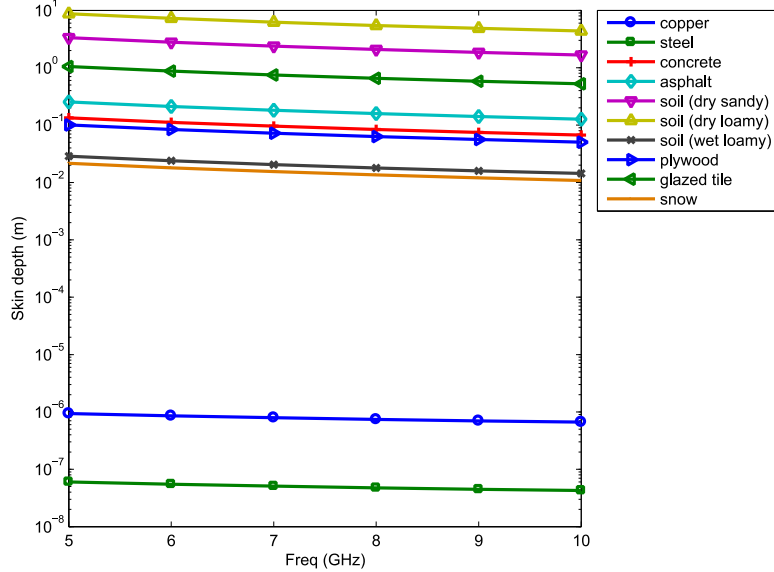


Fig. 3.3. Skin depth for various materials vs. frequency.

where ψ is the antenna specific initial phase in the far field.

3.3. NLOS PROPAGATION

The 2nd ray wave (r_1 , r_2 in Fig. 3.1) interacts with the ground and changes amplitude, phase and polarization depending on the electromagnetic properties of the surface. If the ground can be considered smooth and homogenous, the classical electromagnetic reflection coefficient will describe the resulting wave. Most pedestrian surfaces are relatively smooth, though to be considered homogenous, the ground should be at least a skin depth deep of the modeled material. The skin depth is defined to be the distance within a material where an electromagnetic wave has decreased in amplitude by $1/e$ or 0.368 of its original value. Mathematically, this is found from the wave propagation constant within the medium

$$\gamma = \sqrt{-\omega^2 \mu \epsilon + j \omega \mu \sigma_s}, \quad (3.17)$$

$$\delta = 1/\text{Re}\{\gamma\}, \quad (3.18)$$

where γ is the propagation constant, ω is the radial frequency, σ_s is the static conductivity and δ is the skin depth. Fig. 3.3 shows the skin depth for various materials with parameters given in Table

3.1 - ϵ_r, μ_r are relative dielectric constant and magnetic permeability with respect to their vacuum values. In cases where the dielectric loss tangent $\tan\delta_e$ is given, conductivity is found by $\sigma_s = \omega\epsilon\text{tan}\delta_e$. For materials such as concrete, soil, steel, and snow, the typical surface is homogenous for at least one skin depth. Indoor materials such as plywood and glazed tile may not be thick enough to consider homogenous and may require more careful treatment (such as effective reflection coefficient for multiple interfaces [25]).

Material	ϵ_r	σ_s (S/m)	$\tan\delta_e$	μ_r	Freq (GHz)
Copper [25]	1	5.76e7	-	0.999991	-
Mild Steel [25]	1	6.99e6	-	2000	-
Concrete [26]	5.65	0.151	0.06	1	8
Asphalt (rock aggregate) 8.5% [27]	6.3	0.116	0.03	1	11
Soil (dry sandy) [28]	2.53	5.07e-3	0.0036	1	10
Soil (dry loamy) [28]	2.44	1.09e-3	0.0014	1	10
Soil (13.77% moisture loamy) [28]	13.8	1.38	0.18	1	10
Plywood [29]	2.5	0.117	0.12	1	7
Glazed tile [30]	5.28	2.28e-2	0.00792	1	9.8
Snow [25]	3.3	-	0.5	1	-

Table 3.1. Electromagnetic properties of various materials.

Under oblique incidence the reflected wave must be treated in two, orthogonal electric field components: parallel and perpendicular to the plane-of-incidence. In Fig. 3.4, these electric (E) and magnetic (H) field components for wave reflection are shown with i, r, t indicating incidence, reflected and transmitted respectively and \perp, \parallel for perpendicular and parallel components. β_x is the wave vector and points along the direction of propagation with magnitude $\beta = \text{Im}\{\gamma\} \cong 2\pi/\lambda$. From Snell's law, the angle θ off the surface normal (defined in (3.5)) is equal for incidence and reflected waves whereas the transmitted angle is defined as

$$\theta_t = \text{asin}(\gamma_1 \sin \theta / \gamma_2), \quad (3.19)$$

with $\gamma_{1,2}$ defined in (3.17) for the respective medium. Combined with the complex wave (or intrinsic) impedance for each medium

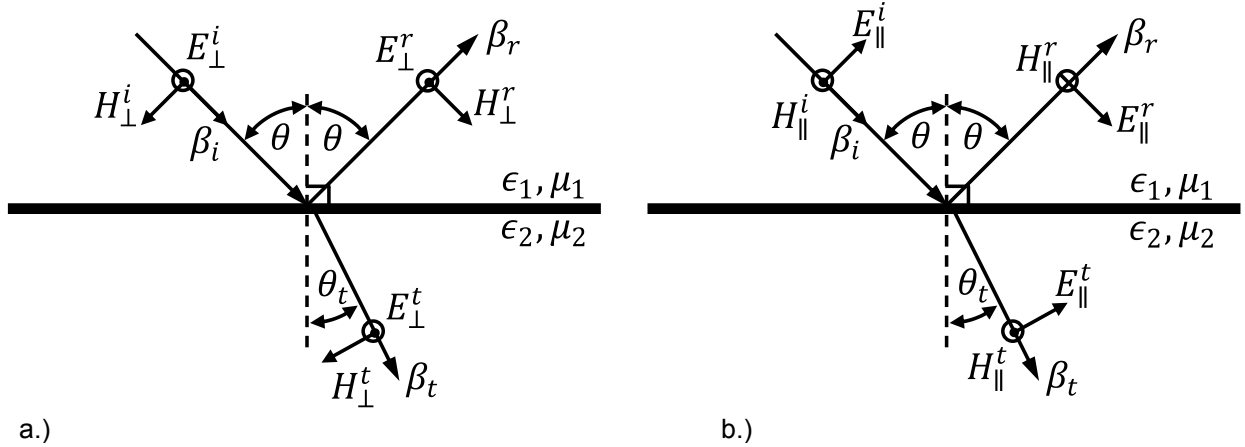


Fig. 3.4. Oblique incidence geometry at surface interface between medium 1 and 2 for perpendicular (a) and parallel (b) electric field components in plane-of-incidence.

$$\eta = \sqrt{\frac{j\omega\mu}{\sigma_s + j\omega\epsilon}} , \quad (3.20)$$

the complex Fresnel reflection coefficient describing amplitude and phase characteristics of the electric field upon reflection can be defined [25]

$$\Gamma_{\perp} = \frac{\eta_2 \cos\theta - \eta_1 \cos\theta_t}{\eta_2 \cos\theta + \eta_1 \cos\theta_t} , \quad (3.21)$$

$$\Gamma_{\parallel} = \frac{-\eta_1 \cos\theta + \eta_2 \cos\theta_t}{\eta_1 \cos\theta + \eta_2 \cos\theta_t} . \quad (3.22)$$

To calculate the NLOS signal, a common coordinate system is required. The most convenient coordinate system is the oblique plane-of-incidence shown in Fig. 3.4 which has unit vectors

$$\hat{\mathbf{E}}_{\perp}^i = \hat{\mathbf{E}}_{\perp}^r = \frac{\mathbf{r}_1 \times \mathbf{R}}{|\mathbf{r}_1 \times \mathbf{R}|} , \quad (3.23)$$

$$\hat{\mathbf{E}}_{\parallel}^i = \frac{\hat{\mathbf{E}}_{\perp}^i \times \mathbf{r}_1}{|\hat{\mathbf{E}}_{\perp}^i \times \mathbf{r}_1|} , \quad (3.24)$$

$$\hat{\mathbf{E}}_{\parallel}^r = \frac{\hat{\mathbf{E}}_{\perp}^r \times \mathbf{r}_2}{|\hat{\mathbf{E}}_{\perp}^r \times \mathbf{r}_2|} , \quad (3.25)$$

where vectors $\mathbf{R} = \mathbf{A}_2 - \mathbf{A}_1$, $\mathbf{r}_1 = \mathbf{P} - \mathbf{A}_1$, and $\mathbf{r}_2 = \mathbf{P} - \mathbf{A}_2$ as shown in Fig. 3.1. Both transmit and receive antenna $\mathbf{r}\tilde{\mathbf{E}}$ must be projected into this coordinate system (superscript V) before an

equation similar to (3.16) can be constructed. Additionally, the incident electric field is scaled by the Fresnel reflection coefficients in (3.21) and (3.22). The projected electric field vectors are

$$\tilde{\mathbf{E}}_t^v = \Gamma_{\perp} (E_{\theta_t} \hat{\boldsymbol{\theta}}_t \cdot \hat{\mathbf{E}}_{\perp}^i + E_{\phi_t} \hat{\boldsymbol{\phi}}_t \cdot \hat{\mathbf{E}}_{\perp}^i) \hat{\mathbf{E}}_{\perp}^i + \Gamma_{\parallel} (E_{\theta_t} \hat{\boldsymbol{\theta}}_t \cdot \hat{\mathbf{E}}_{\parallel}^i + E_{\phi_t} \hat{\boldsymbol{\phi}}_t \cdot \hat{\mathbf{E}}_{\parallel}^i) \hat{\mathbf{E}}_{\parallel}^i, \quad (3.26)$$

$$\tilde{\mathbf{E}}_r^v = (E_{\theta_r} \hat{\boldsymbol{\theta}}_r \cdot \hat{\mathbf{E}}_{\perp}^r + E_{\phi_r} \hat{\boldsymbol{\phi}}_r \cdot \hat{\mathbf{E}}_{\perp}^r) \hat{\mathbf{E}}_{\perp}^r + (E_{\theta_r} \hat{\boldsymbol{\theta}}_r \cdot \hat{\mathbf{E}}_{\parallel}^r + E_{\phi_r} \hat{\boldsymbol{\phi}}_r \cdot \hat{\mathbf{E}}_{\parallel}^r) \hat{\mathbf{E}}_{\parallel}^r. \quad (3.27)$$

Similar to the LOS signal in (3.14)-(3.16), the NLOS signal can be calculated as

$$e_{NLOS} = r \tilde{\mathbf{E}}_t^v(\theta_t, \phi_t) \cdot r \tilde{\mathbf{E}}_r^{v*}(\theta_r, \phi_r), \quad (3.28)$$

$$\angle e_{NLOS} = \text{atan2}(\text{Im}\{e_{NLOS}\}, \text{Re}\{e_{NLOS}\}), \quad (3.29)$$

$$S_{NLOS} = \sqrt{P_t} \left[\frac{\lambda}{2\eta_1 P_{in}(r_1+r_2)} \right] |r \tilde{\mathbf{E}}_t^v(\theta_t, \phi_t) \cdot r \tilde{\mathbf{E}}_r^{v*}(\theta_r, \phi_r)| e^{j(k(r_1+r_2) + \angle e_{NLOS} + \psi)}. \quad (3.30)$$

Note that the polarization phase in (3.29) for the NLOS path also includes the phase change from the reflection coefficient. Combining (3.16) and (3.30) and including additive white Gaussian noise (AWGN) the 2-ray channel model is found to be

$$S = S_{LOS} + S_{NLOS} + w_n, \quad (3.31)$$

where w_n indicates complex AWGN with thermal noise power of $k_B T B$, k_B is the Boltzmann constant, T is the temperature in kelvin, B is the analog bandwidth of the receiver.

CHAPTER 4

4. RANGING ALGORITHMS

SFCW samples the channel response in the frequency domain with N measurements over a bandwidth B . Each measurement yields a complex number corresponding to the specific attenuation and phase shift each frequency experienced within the channel. Two approaches will be used to convert these measurements into ranges: an inverse Fourier transform and a parametric modeling approach (Prony analysis) that performs a numeric fit to complex exponentials. This chapter will describe these two approaches along with a method to combine SFCW ranges with CW measurements. Finally, a discussion of a few methods to filter out ranges with poor accuracy will be described.

4.1. FOURIER TRANSFORM

The sampled channel response in the frequency domain can be related to its time domain impulse response through the inverse discrete Fourier transform (DFT). For N samples of the channel S_k , the inverse DFT is defined as [31]

$$s_n = \frac{1}{N} \sum_{k=0}^{N-1} S_k e^{j2\pi \frac{k}{N} n}, \quad (4.1)$$

where n is the time index, k is the frequency index and N is the number of samples. The time vector for s_n is

$$t_n = \frac{n}{\Delta f_s(N-1)}, \text{ for } n = 0, 1 \dots N-1. \quad (4.2)$$

where $\Delta f_s = \frac{B}{(N-1)}$ is the frequency step size. Under certain circumstances it may be desirable to zero-pad the S_k data vector to interpolate the peak position more accurately. Zero padding S_k to length L , where $L > N$, results in a time step of $\delta t = \frac{1}{\Delta f_s(L-1)}$. Single target range is computed as

$$R_{DFT} = ct_n|_{\max(|s_n|)}. \quad (4.3)$$

Depending on Δf_s and the choice of L , the computational penalty to compute the inverse DFT may become too large for a real-time system.

4.1.1. CHIRP z -TRANSFORM

The Chirp z -Transform (CZT) is a computationally efficient method of padding a DFT within a subset of the transform [32]. A DFT is computed along the entire unit circle (i.e. for all possible frequencies), whereas the CZT can be specified to compute the solution along a smaller arc of the unit circle with an arbitrary amount of interpolation. The CZT is defined as

$$S_z = \sum_{n=0}^{N-1} s_n z^{-n}, \quad (4.4)$$

$$z = AW^{-k} \text{ for } k = 0, 1 \dots M_T - 1, \quad (4.5)$$

$$W = W_0 e^{j2\pi\phi_0}, \quad (4.6)$$

$$A = A_0 e^{j2\pi\theta_0}, \quad (4.7)$$

where N is again the number of input samples, M_T is the number of output samples, A describes the starting point of the transform with angle θ_0 and W is the frequency increment. If $A_0 = W_0 = 1$,

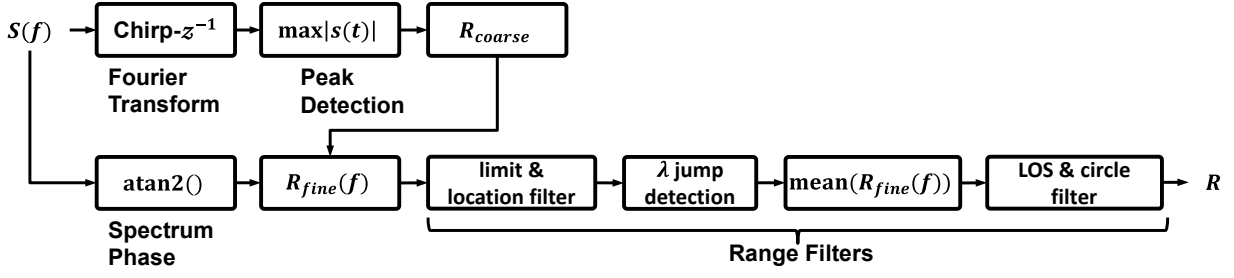


Fig. 4.1. Overview of Chirp- z ranging algorithm.

$\theta_0 = 0$, $\phi_0 = -1/N$, and $M_T = N$, the CZT is equal to the DFT. When the CZT is constrained to the unit circle ($A_0 = W_0 = 1$), the inverse CZT is defined as [33]

$$s_z = \left[\sum_{n=0}^{N-1} S_n^* z^{-n} \right]^*, \quad (4.8)$$

where $*$ indicates the complex conjugate. For the purposes of zero-padding the inverse DFT in the range between L_{min} and L_{max} (in meters), the inverse CZT coefficients are defined

$$W = e^{-j2\pi \frac{\Delta f_s (L_{max} - L_{min})}{c(M_T - 1)}}, \quad (4.9)$$

$$A = e^{j2\pi \frac{\Delta f_s L_{min}}{c}}. \quad (4.10)$$

The corresponding time vector for s_z is

$$t_z = \frac{L_{min}}{c} + \frac{L_{max} - L_{min}}{c(M_T - 1)} z, \text{ for } z = 0, 1 \dots M_T - 1. \quad (4.11)$$

Range for a single peak is determined in the same manner as the DFT

$$R_{CZT} = ct_z|_{\max(|s_z|)}. \quad (4.12)$$

The CZT is not always more efficient than the equivalent zero-padded DFT. The Matlab implementation of the CZT involves three DFT operations with length $M_T + N - 1$ rounded to the nearest power of 2. While not implemented in this work, a smart algorithm could estimate the computation cost of the CZT versus the equivalent zero-padded DFT to select the most appropriate

approach for minimizing processing time. Fig. 4.1 shows a block diagram overview of the ranging algorithm using the Chirp- z transform. CW and range filtering will be discussed in section 4.3 and 4.4.

4.2. PRONY ANALYSIS

An alternative method to compute the range between shoes is based on parametric modeling of the underlying form of the measured data. From chapter 3, it was found that the channel is predicted to be mathematically described with a sum of complex exponentials corresponding to line-of-sight (LOS) and multipath non-LOS (NLOS) components

$$S = \sum A e^{j\vartheta}. \quad (4.13)$$

With parametric modeling, an assumption is made on the complexity of the data (how many exponentials) and then a numeric fit is performed. If the underlying model is consistent with reality, parametric modeling has the potential for accuracy far beyond the Fourier technique because it can potentially isolate the multipath components from the LOS.

Prony's Method is one approach to parametrically fitting regularly sampled data to a sum of complex exponentials that has been successfully applied to radar data [34]. The form of the model is as follows

$$S_n = \sum_{k=1}^M C_k \mu_k^n + w_n, \quad \text{for } n = 0, 1, \dots, N-1. \quad (4.14)$$

where M is the model order, N is the number of data samples, w_n is complex noise and

$$\mu_k^n = e^{(\alpha_k + j\vartheta_k)n}, \quad (4.15)$$

$$\vartheta_k = \Delta k R = 2\pi \frac{R}{\Delta \lambda} = \frac{2\pi \Delta f_s R}{c}. \quad (4.16)$$

Solving these equations requires $N \geq 2M$. In the $N > 2M$ case, (4.14) is solved in the least-squares (LS) sense. The general approach to solving for μ_k is to let them be the roots to the polynomial equation

$$\begin{aligned} B(z) &= 1 + b_1 z + b_2 z^2 + \cdots + b_M z^M = 0 \\ &= (z - \mu_1)(z - \mu_2) \cdots (z - \mu_M). \end{aligned} \quad (4.17)$$

This converts the nonlinearity from μ_k in (4.14) to a single polynomial equation.

Solving for the coefficients $b = [b_1 \ b_2 \ \cdots \ b_M]^T$ is through arranging the sampled data S_n into a data matrix Y and an observation vector y

$$Yb = -y, \quad (4.18)$$

for which the LS solution is

$$b = -Y^+y, \quad (4.19)$$

where $+$ indicates the Moore-Penrose pseudoinverse. The roots of the b polynomial coefficient vector are the values for μ_k . For a detailed discussion of the Prony Method using LS, see [35]. It is known that in the low SNR case, the least squares method has significant errors [36]. The total least squares (TLS) extension to the Prony Method has been shown in [36] to perform well in the presence of noise through the use of singular value decomposition (SVD) to reduce the rank (decreasing the noise effect) of the data matrix Y and observation column vector y .

The data matrix and the observation vector are formed through a Hankel matrix of the spectral samples S_n for the backward linear prediction equation [37]

$$[y \ : \ Y] \begin{bmatrix} 1 \\ b \end{bmatrix} \approx 0, \quad (4.20)$$

$$[y \ : \ Y] = \begin{bmatrix} S_0 & S_1 & \cdots & S_M \\ S_1 & S_2 & \cdots & S_{M+1} \\ \vdots & \vdots & \ddots & \vdots \\ S_{N-M-1} & S_{N-m} & \cdots & S_{N-1} \end{bmatrix}. \quad (4.21)$$

The SVD of (4.21) is

$$SVD([y \ : \ Y]) = U\Sigma V^*. \quad (4.22)$$

Rank reduction is performed on the Σ matrix by setting a portion of the diagonal elements to 0, keeping m of the j diagonal elements

$$\Sigma = \begin{bmatrix} \sigma_1 & & & \\ & \sigma_2 & & \\ & & \ddots & \\ & & & \sigma_j \\ \mathbf{0} & & & \end{bmatrix}_{(N-M) \times (M+1)}, \quad (4.23)$$

$$\hat{\Sigma} = \begin{bmatrix} \sigma_1 & & & \\ & \ddots & & \\ & & \sigma_m & \\ \mathbf{0} & & & 0 \end{bmatrix}_{(N-M) \times (M+1)}, \quad (4.24)$$

The diagonal elements in Σ are ordered from largest to smallest. Generally, a threshold will be used to determine which elements are zeroed. For the SRS case, the LOS is the only desired signal so all but the first element in Σ ($m=1$) is zeroed – this seems to produce the highest range accuracy even with low SNR. To also calculate the NLOS ground reflection, the second element in the diagonal should be retained as well ($m=2$). The rank reduced version of (4.21) is

$$[\hat{y} \ : \ \hat{Y}] = U\hat{\Sigma}V^*. \quad (4.25)$$

Similar to (4.19), the coefficients to $B(z)$ are

$$b = -\hat{Y}^+\hat{y}, \quad (4.26)$$

and the values of the exponentials are

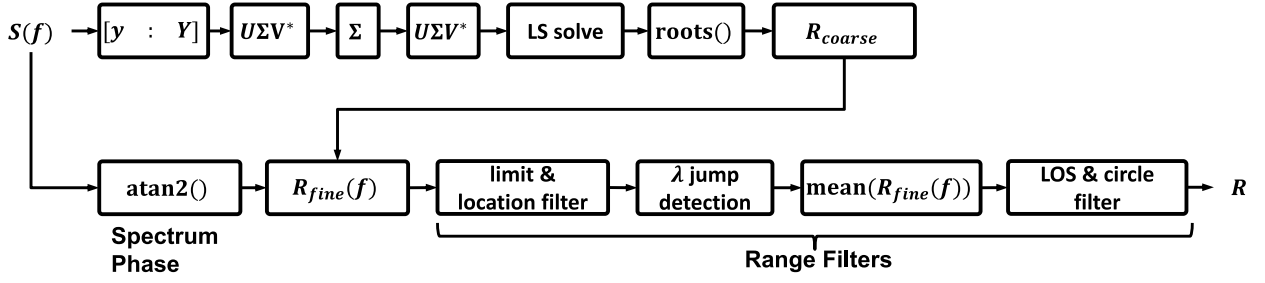


Fig. 4.2. Overview of Prony ranging algorithm.

$$\hat{\mu}_k = \text{roots} \left(\begin{bmatrix} b^\downarrow \\ 1 \end{bmatrix} \right), \quad (4.27)$$

where \downarrow indicates that element ordering is flipped to $b^\downarrow = [b_M \ b_{M-1} \ \dots \ b_1]^T$ for proper treatment by the root finding algorithm.

The remaining step is to solve for the amplitude coefficients C_k . This is done by solving the following equation using LS

$$\begin{bmatrix} 1 & 1 & \dots & 1 \\ \hat{\mu}_1 & \hat{\mu}_2 & \dots & \hat{\mu}_M \\ \hat{\mu}_1^2 & \hat{\mu}_2^2 & \dots & \hat{\mu}_M^2 \\ \vdots & \vdots & & \vdots \\ \hat{\mu}_1^{N-1} & \hat{\mu}_2^{N-1} & \dots & \hat{\mu}_M^{N-1} \end{bmatrix} \begin{bmatrix} \hat{C}_1 \\ \hat{C}_2 \\ \vdots \\ \hat{C}_{M-1} \end{bmatrix} \approx \begin{bmatrix} S_0 \\ S_1 \\ S_2 \\ \vdots \\ S_{N-1} \end{bmatrix} \quad (4.28)$$

and equivalently

$$\hat{A}\hat{C} = S, \quad (4.29)$$

where both S and \hat{C} are column vectors and \hat{A} is a matrix of size $N \times M$. The solution to this equation is

$$\hat{C} = \hat{A}^+ S. \quad (4.30)$$

Range from the TLS Prony method is computed using (4.15), (4.16) and (4.27)

$$R_{TLS} = \text{Im}\{\ln(\hat{\mu}_k)\}/\Delta k. \quad (4.31)$$

The k value for the LOS solution can vary. One method to find the LOS output is to check the amplitude coefficients for the largest magnitude (which should be the LOS). If $m=1$, the LOS solution always shows up at the same value of k and it is unnecessary to calculate \hat{C} for determining range. Fig. 4.2 shows a block diagram of the steps involved for calculating range based on the Prony method. CW and range filtering methods displayed in the figure are discussed in section 4.3 and 4.4.

4.3. CW RANGING

The coarse range estimates from either Fourier or Prony analysis are combined with CW phase measurements to form the fine range

$$R_{fine} = \lambda \left(\frac{\theta}{2\pi} + \left\lfloor \frac{R_{coarse}}{\lambda} \right\rfloor \right) = \lambda N_{CW}, \quad (4.32)$$

where λ is the wavelength (c/f) at a particular frequency, and θ is between $0-2\pi$, N_{CW} is the fractional distance normalized to the wavelength. Due to noise in R_{coarse} , N_{CW} may jump to the next integer wavelength too soon. To counteract this effect, a smoothing algorithm on N_{CW} is used that looks at the solution of the last time instance. Let t be the previous time instance and $t + t_0$ is the current time instance of N_{CW} , the smoothing algorithm is

$$dN_{CW} = N_{CW}(t + t_0) - N_{CW}(t), \quad (4.33)$$

$$N'_{CW}(t + t_0) = N_{CW}(t + t_0) - \text{sign}(dN_{CW}), \quad \text{if } |dN_{CW}| > N_{thresh}. \quad (4.34)$$

N_{thresh} is between 0-1 and found experimentally (0.6 was found to work the best). The `sign()` function returns ± 1 depending on the sign of the argument. N'_{CW} is the new value of N_{CW} at time instance $t + t_0$ with the wavelength jump corrected. Equation (4.34) is only used if the criterion $|dN_{CW}| > N_{thresh}$ is met, signifying a wavelength-sized jump has occurred. The smoothing filter is reset if any of the range filtering mechanisms in section 4.4 is activated. Note that the smoothing filter can result in a velocity limit depending on the time step t_0 . If the max velocity is greater than

λ/t_0 , then the smoothed output will generate large errors in the range. Assuming a fast sweep rate $f_R=600$ Hz, $\lambda=4$ cm, and a max velocity of 3 m/s, then the range update rate ($1/t_0$) should be >75 Hz.

There are N measurements of range R_{fine} available for each sweep (one for each frequency). A method to combine these ranges into a single output is to simply compute the average. This has the effect of reducing the impact of wavelength jumps not corrected by the smoothing filter because these jumps will occur at different locations depending on the wavelength. Additionally, if a particular range is more strongly affected by multipath than others, the averaged output will be degraded less. Another method may be to analyze the N ranges for outliers first and remove them from the average solution. This may result in higher accuracy if the majority of the R_{fine} ranges are correct. If instead the removed outlier ranges were correct, lower accuracy compared to first method may be obtained. Only the first method (complete average) was implemented in this work.

4.4. RANGE FILTERING

Inaccurate ranges may occur for a variety of reasons such as strong multipath, non-ideal antenna effects, hardware malfunction or signal blockage. In this section, four methods to remove inaccurate ranges will be described. Only robust methods are reported as other techniques that were evaluated (such as signal power analysis) were found to have inconsistent performance. Setting thresholds based on signal power or the derivative of power (to detect nulls) was found to be unreliable due to variations between a pedestrian's step and different antenna characteristics.

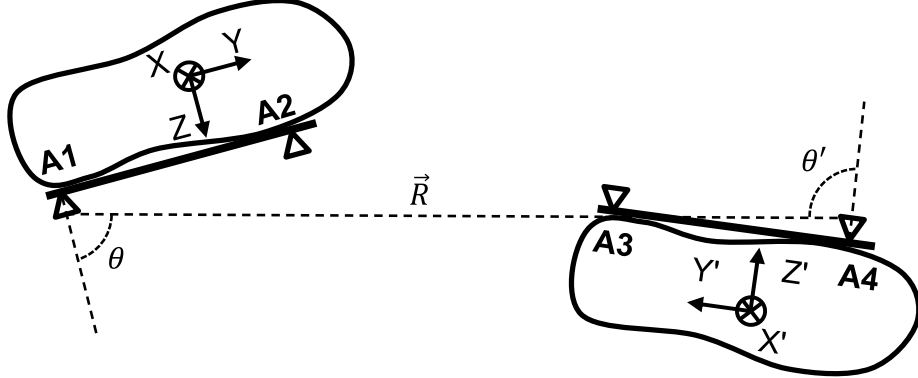


Fig. 4.3. LOS blockage of vector \vec{R} between antennas A1 and A4.

4.4.1. RANGE LIMITS

The most basic range filter simply checks whether the computed range is within a preconfigured range bound i.e. $L_{min} \leq R \leq L_{max}$. If the computed range (R) is outside those bounds, the solution is forced to 0 so that subsequent processing knows to discard it.

4.4.2. LINE-OF-SIGHT

It is possible for the shoes to have an orientation such that LOS is blocked by the shoe itself.

Given the coordinate systems for each shoe in Fig. 4.3, the angles are defined as

$$\theta = \arccos(R_z / |\vec{R}|), \quad (4.35)$$

$$\theta' = \arccos(R_{z'} / |\vec{R}|), \quad (4.36)$$

where R_z and $R_{z'}$ are the Z and Z' components of LOS vector \vec{R} . The navigation system can calculate θ and θ' based on the location and orientation of each shoe. LOS exists as long as $\theta \leq \pi/2$ and $\theta' \leq \pi/2$ for a given range pair.

4.4.3. ANTENNA LOCATION

There are certain locations within a step where the SRS may be known to produce bad ranges. This is primarily due to antenna effects such as nulls, polarization changes or proximity to the near-

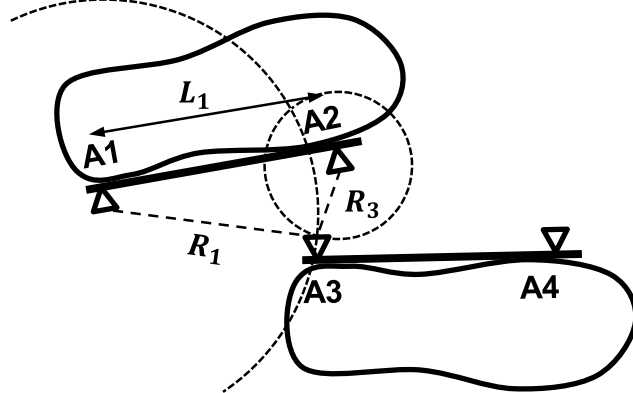


Fig. 4.4. Range circle intersection between A1, A2 and A3. L_1 is the fixed distance between A1 and A2.

field zone. After SRS characterization, these regions may be mapped and the navigation system can ignore the ranges produced while within the region. See section 5.3.2.1 for an example of this filter.

4.4.4. RANGE CIRCLE INTERSECTION

Two ranges that share a common antenna should have intersecting range circles (Fig. 4.4). If one of the following equations is true

$$L_1 > R_1 + R_3, \quad (4.37)$$

$$L_1 < |R_1 - R_3|, \quad (4.38)$$

then one of the ranges is inaccurate, where L_1 is the fixed distance between mount points of antennas A1 and A2, R_1 is the range between A1 and A3 and R_3 is the range between A2 and A3. (4.37) is the criteria that the circles intersect and (4.38) is the condition that one circle is not contained within the other. Similar equations can be defined for R_2 (range between A1 and A4) and R_4 (range between A2 and A4). This filter is best suited for rejecting grossly inaccurate ranges, such as those from improper peak selection in the Chirp- z , as smaller errors may still have intersecting range circles.

CHAPTER 5

5. SHOE RANGING SENSOR SIMULATOR

The purpose of channel simulation is to gain insight on performance characteristics of a wireless system in a controlled environment. This can help shape hardware requirements as well as analyze problems seen from hardware if the simulator is accurate enough. The SRS channel offers a somewhat unique challenge in that the antennas are nearly always in motion both in position and in orientation. Most standard wireless scenarios can consider the polarization of the antennas to be relatively fixed during the measurement period. In the context of ranging, this changing polarization may introduce a phase term that adds error to the range estimate.

This chapter will cover the development of an SRS Simulator. The simulator moves an antenna pair through predefined positions and orientations and calculates a 2-ray channel model. This channel model is excited by SFCW modulation to simulate the SRS with different antennas and ranging algorithms. The channel model prediction for polarization phase will be compared to measured results for validation. A comparison will be made between the different types of ranging algorithms as well as the effect of different antennas. Finally, an extension of the model will be made to handle a multi-ranger system.

5.1. SRS SIMULATOR DESIGN

The SRS Simulator is implemented in Matlab and uses ground-truth position and orientation for each shoe above a surface to generate a 2-ray propagation model. Ground-truth data is sourced from inertial measurement units (IMUs) mounted on shoes under normally walking conditions. The IMU dataset is from ~ 5 s of walking data just after calibration so accumulated error is not significant. Also, a single-axis cosine motion on a linear motor stage is available as ground-truth. An SFCW waveform is synthesized and propagated through the model with AWGN to produce the channel response. Antenna characteristics for the model are obtained from HFSS simulations or are generated from equations. Finally, one or more of the ranging algorithms is performed on the channel response to determine performance. Table 5.1 gives a description of the steps involved for the simulator along with references to the chapters containing more detail.

Step	Description	Chapter Reference
1	Define constants: $N, f, \epsilon_{1,2}, \mu_{1,2}, \eta_{1,2}, \gamma_{1,2}, c, P_t, w_n, f_R, \sigma_{s1,2}$	2.3.2, 2.3.4, 3.2, 3.3
2	Load antenna data for right and left shoe	5.1.1
3	Load position and orientation ground-truth data	5.3
4	Define antenna origins within IMU frame	A.1.1
5	Transform antenna location to global NED frame and define LOS vector	A.1.2, A.2
6	2-ray geometry calculation for NLOS vector	3.1
7	Rotate LOS/NLOS vector from NED to antenna spherical coordinates	A.1.2
8	Rotate spherical coordinate unit vectors to NED	A.1.3
9	Define unit vectors for $\Gamma_{\parallel, \perp}$ in NED frame	3.3
10	Resample all to SFCW rate (Nf_R)	2.3.4
11	Generate frequency dependent $\Gamma_{\parallel, \perp}$	3.3
12	Interpolate antenna E-field components along LOS/NLOS and f	5.1.1
13	Project LOS left antenna E-field onto right antenna components	3.2
14	Project NLOS E-field components onto unit vectors for $\Gamma_{\parallel, \perp}$	3.3
15	Calculate Gain and polarization phase for LOS/NLOS paths	3.2, 3.3
16	Add LOS/NLOS channel response together with AWGN	3.3
17	Apply range filtering and ranging algorithm (CZT/TLS)	4

Table 5.1. SRS Simulator steps.

5.1.1. ANTENNA INTEGRATION

Ansoft HFSS is used to model the antennas for the simulation. The radiated electric-field $r\tilde{\mathbf{E}}$ solution from HFSS includes matching losses, efficiency and polarization characteristics of the antenna. For simulated antennas, an HFSS file is created that includes $r\tilde{\mathbf{E}}$ far-field spherical components in θ and ϕ at 4° increments and across frequency in 100 MHz steps. Within the SRS Simulator, these components are 3D cubic interpolated to the requested frequency and angles.

The HFSS antennas that are included for simulation are wideband Vivaldi, E-shaped patch, and a dipole with integrated balun. More details on these antennas will be given in chapter 6. The Vivaldi antenna is actually an array of two Vivaldi antennas with bandwidth at least 6-9 GHz and provides a beam directed toward the front and rear of a shoe (maximizing signal when shoes are furthest apart). Two versions of the Vivaldi simulation are used: one with ~ 1 cm straight coax feed and the other with ~ 1 cm right angle feed (labeled RA). The E-shaped patch (referred to as patch) has ~ 770 MHz of simulated bandwidth centered around 6.9 GHz and is mounted parallel to the shoe (peak gain normal to side of foot). The dipole with integrated balun (referred to as dipole) has ~ 1.4 GHz of simulated bandwidth at 6.9 GHz.

In addition to the HFSS antennas, a theoretical $\lambda/2$ dipole is available to simulate a polarization pure antenna. This antenna is treated as frequency independent, i.e. it is $\lambda/2$ for whatever frequency is requested. The equation for this antenna model uses the integral form as there are numeric difficulties found in the closed form solution. From [24],

$$E_\theta \simeq j\eta \frac{\sqrt{P_{in}/R_r} e^{-jkr}}{2\pi r} \frac{\cos\left(\frac{\pi}{2} \cos \theta\right)}{\sin \theta}, \quad (5.1)$$

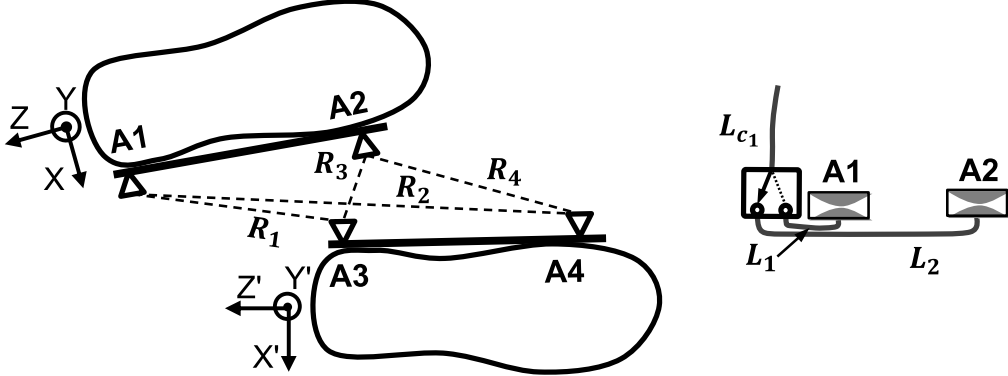


Fig. 5.1. SRS Multi-Ranger naming convention (left). Finite isolation RF switch fed by RF cables with length L_{c_1} , L_1 , and L_2 for the left shoe (right). Coordinate systems are defined for each IMU.

where η is the intrinsic impedance, $k = 2\pi/\lambda$ is the wavenumber, P_{in} is the input power to the terminals (1W as with HFSS), r is the radial distance (taken to be 1m), and R_r is the radiation resistance (73Ω for $\lambda/2$ dipole). There is no E_ϕ component in the far-field of an ideal dipole antenna. E_θ in (5.1) is calculated across frequency and angle to generate a similar set of data as the HFSS antennas.

5.1.2. MULTI-RANGER EXTENSION

The SRS Simulator outlined previously can be easily extended to the SRS Multi-Ranger design. A first order approach is to run the simulator for all antenna pair combinations (4 for the SRS). However this treats the RF switch as an ideal component with perfect isolation. In reality, the RF switch has signal leakage between the selected and the disconnected path. This results in a multipath effect which may degrade ranging performance if switch isolation is too low. The multipath effect can be modeled by taking the individual (isolated) simulated channel from each antenna pair and summing attenuated and phase shifted combinations to simulate the non-ideal switch.

As shown in Fig. 5.1, antennas are connected through cables of some length that add a phase shift to the signal. L_{c_1} is the cable length on the left shoe that connects the switch to the calibration point of the SRS, L_1 and L_2 are the lengths to connect the switch to A1 and A2 respectively. A

corresponding set of cable lengths L_{c_2}, L_3 and L_4 exists for the right shoe. The signal phase shift from the cable length assuming negligible attenuation is

$$D_k = e^{j2\pi L_k / (\lambda v_p)} \text{ for } k = c_1, c_2, 1, 2, 3, 4, \quad (5.2)$$

where v_p is the velocity propagation factor within the cable (% of c , 83% for the cables used) and all lengths are in meters. With (5.2) and the single switch isolation A (dB), the multi-ranger channel response for each switch pair (S_1, S_2, S_3, S_4) is

$$S'_1 = S_1 + \frac{10^{-A/20}}{(D_1 D_3)^*} \left(\frac{S_3}{D_2 D_3} + \frac{S_2}{D_1 D_4} + \frac{10^{-A/20} S_4}{D_2 D_4} \right), \quad (5.3)$$

$$S'_2 = S_2 + \frac{10^{-A/20}}{(D_1 D_4)^*} \left(\frac{S_1}{D_1 D_3} + \frac{S_4}{D_2 D_4} + \frac{10^{-A/20} S_3}{D_2 D_3} \right), \quad (5.4)$$

$$S'_3 = S_3 + \frac{10^{-A/20}}{(D_2 D_3)^*} \left(\frac{S_1}{D_1 D_3} + \frac{S_4}{D_2 D_4} + \frac{10^{-A/20} S_2}{D_1 D_4} \right), \quad (5.5)$$

$$S'_4 = S_4 + \frac{10^{-A/20}}{(D_2 D_4)^*} \left(\frac{S_3}{D_2 D_3} + \frac{S_2}{D_1 D_4} + \frac{10^{-A/20} S_1}{D_1 D_3} \right), \quad (5.6)$$

where $*$ is the complex conjugate which shifts the multipath components to the reference plane of the LOS antenna pair. Range is then computed with the new channel response accounting for RF switch feedthrough. For simplicity, all channel responses are simulated simultaneously using the same time base – i.e. the time division multiplexing is not simulated in this model.

5.2. CHANNEL MODEL VERIFICATION

One of the critical components of the channel model in chapter 3 is the polarization phase term derived from $r\tilde{\mathbf{E}}$. This term has the potential to affect ranging accuracy because range is calculated from signal phase with the algorithms used in this work. Therefore, it is important to make sure this calculation is done properly. The equations for polarization phase are repeated here

$$e_{LOS} = r\tilde{\mathbf{E}}_t^r(\theta_t, \phi_t) \cdot r\tilde{\mathbf{E}}_r^*(\theta_r, \phi_r), \quad (5.7)$$

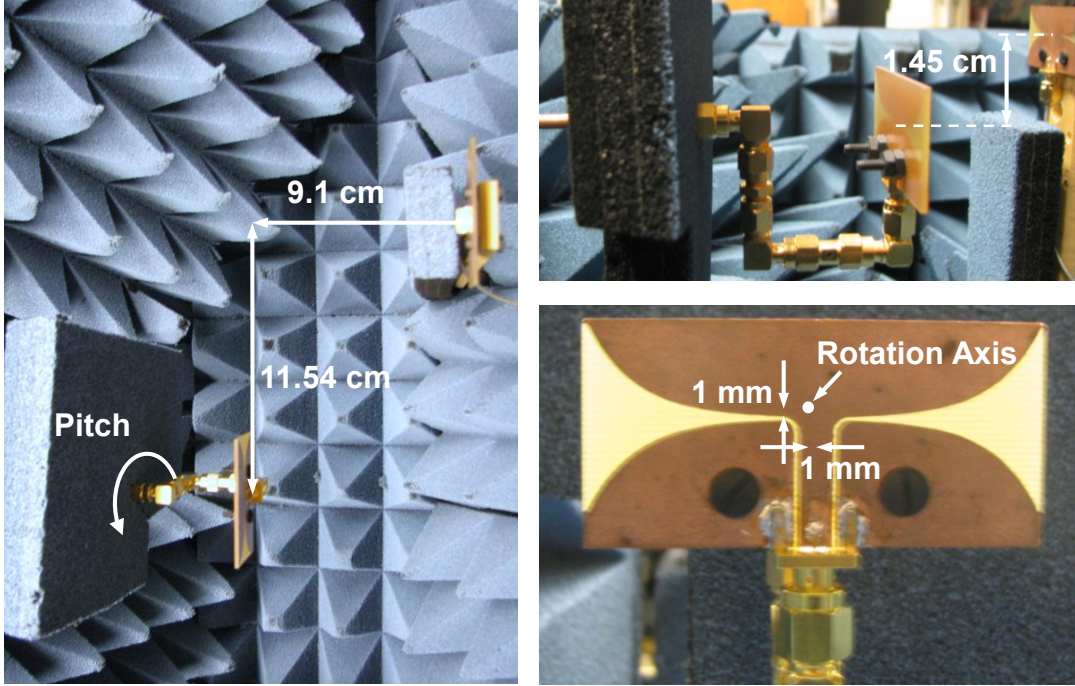


Fig. 5.2. Experimental setup for measuring polarization phase.

$$\angle e_{LOS} = \text{atan2}(\text{Im}\{e_{LOS}\}, \text{Re}\{e_{LOS}\}), \quad (5.8)$$

$$\angle S_{LOS} = kR + \angle e_{LOS} + \psi. \quad (5.9)$$

An experiment was performed to compare (5.9) with the measured phase of a real antenna. In Fig. 5.2, the experiment setup is shown. A pair of wideband Vivaldi antennas are used for the measurement and are positioned at different heights and at a diagonal from each other to produce interesting polarization changes. Alignment was performed with a laser reference and is within ~ 0.5 mm. The left antenna rotates 360° on a Velmex rotary stage while the right antenna remains fixed. Alignment of the left antenna center to the stage rotation axis is 1 mm offset in two dimensions due to the use of RF adapters. Microwave absorbing foam is surrounding the two antennas and rotation structure to ensure LOS is the predominant signal. An Agilent E8358A Vector Network Analyzer (VNA) measured the channel response (S_{LOS}) at 6.876 GHz and 4° increments of rotation. The SRS Simulator was configured for the geometry described in Fig. 5.2 along with HFSS simulations of the Vivaldi antenna. Two different HFSS models were used: a right angle coax feed for the left antenna

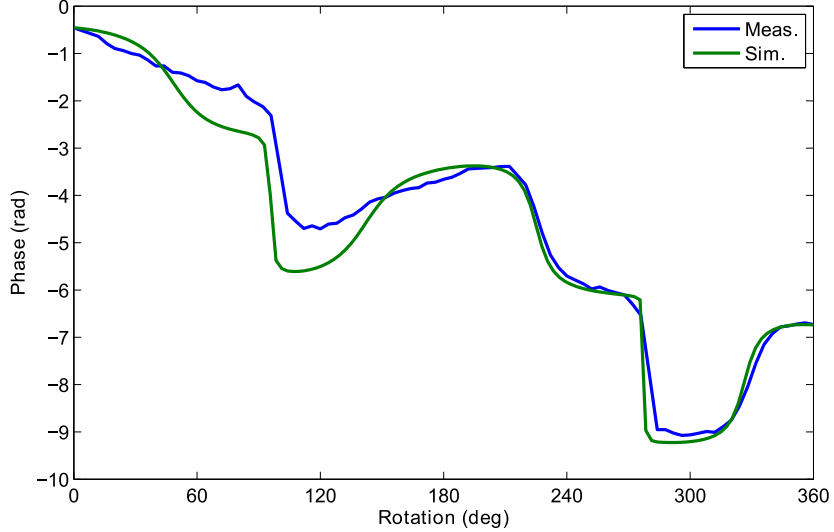


Fig. 5.3. Comparison between SRS Simulator and measured polarization phase.

and a straight feed coax for the right antenna. In both cases, the coax is modeled up to ~ 1 cm from the antenna.

Fig. 5.3 shows the results of the experiment and simulation. The measured results are calibrated to have the same initial phase as the simulated and a phase unwrap operation is used on both datasets. The measured/simulation match is excellent from 180° - 360° , while between 0° - 180° it follows the trends though may have up to 1 radian of error. This can be attributed to the large feed structure on the left antenna which is closest to the right antenna from 0° - 180° . The HFSS model does not include the full feed structure which explains why the simulation is showing a difference. From chapter 2, it was shown from typically walking data that the expected pitch range of the shoe is $+30^\circ$ to -70° . That range of motion does have close agreement so it is not necessary to develop a more complicated HFSS model.

5.3. SRS SIMULATION RESULTS

This section will discuss results of the SRS Simulator with the IMU ground-truth dataset (Fig. 5.4) and compare the different ranging algorithms along with antenna options. The IMU dataset is from a pedestrian walking at ~ 0.8 m/s with high precision MEMS IMUs mounted at the heel of

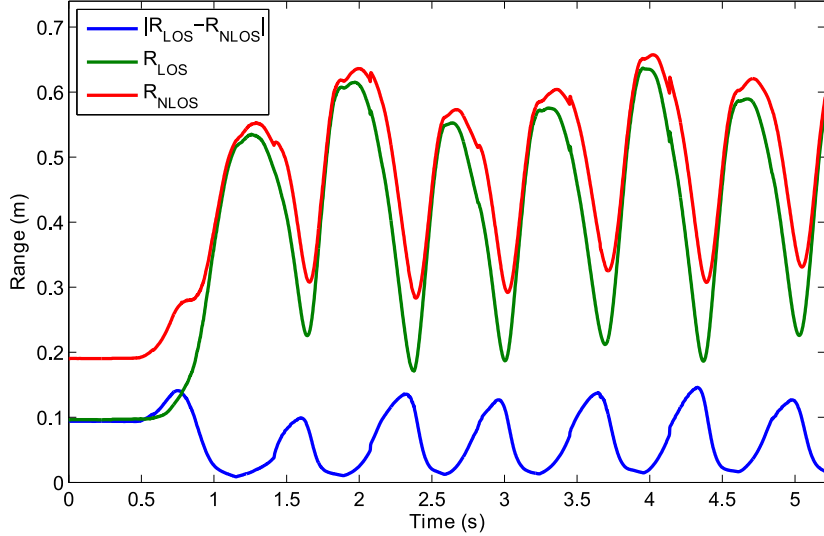


Fig. 5.4. Ground truth range LOS & NLOS and range difference.

each shoe. Given the short time of the data (<6 s), the IMUs have not drifted appreciably from their true position. Also shown in Fig. 5.4 is the NLOS range along with the path difference with respect to the LOS range (6.7 cm average difference). The ability of the Prony method to resolve multipath components will be evaluated. Additionally, the multi-ranger extension will be tested. Results using the motion stage dataset will be shown in chapter 7.

5.3.1. MULTIPLE SURFACE RESULTS

In Table 5.2 - Table 5.8, the mean (μ) and standard deviation (σ) of the range error for different antennas and surfaces are shown. The position of the antennas is at the back of each shoe. Surface model parameters are given in chapter 3. Air is modeled with a relative dielectric constant of 1.0006, conductivity 8e-15 S/m, and relative permeability of 1.0000004. The SFCW settings used are $N=21$ between 6.2-7.7 GHz, with a sweep rate $f_R=600$ Hz. Transmit power is 1 mW (0 dBm) with noise power set for 800 kHz of ADC bandwidth (-114.8 dBm). The TLS Prony method is configured for a model order $M=3$ and $m=1$. Hybrid ranging results are shown unless otherwise stated. No range filtering is used other than if the computed range is beyond 1 m.

Antenna	Chirp- z		TLS Prony	
	μ (mm)	σ (mm)	μ (mm)	σ (mm)
Vivaldi	-27.45	34.03	-14.68	20.31
Vivaldi RA	-14.25	37.39	-8.41	17.25
Patch	0.62	23.58	4.74	18.83
Dipole	-6.47	26.53	-6.71	22.42
Dipole Theory	0.25	6.63	-0.32	4.92

Table 5.2. Ranging algorithm comparison with copper surface.

Antenna	Chirp- z		TLS Prony	
	μ (mm)	σ (mm)	μ (mm)	σ (mm)
Vivaldi	-24.12	35.08	-11.67	18.27
Vivaldi RA	-4.93	38.08	-6.38	14.73
Patch	0.64	22.60	4.55	18.2
Dipole	-7.29	25.75	-6.51	22.76
Dipole Theory	0.06	5.61	-0.38	4.46

Table 5.3. Ranging algorithm comparison with steel surface.

Antenna	Chirp- z		TLS Prony	
	μ (mm)	σ (mm)	μ (mm)	σ (mm)
Vivaldi	-11.12	29.79	-2.02	14.64
Vivaldi RA	-11.97	29.54	-3.79	19.55
Patch	-8.24	18.41	1.45	10.67
Dipole	-11.55	22.09	-6.18	24.66
Dipole Theory	-0.06	2.17	0.54	1.64

Table 5.4. Ranging algorithm comparison with concrete surface.

Antenna	Chirp- z		TLS Prony	
	μ (mm)	σ (mm)	μ (mm)	σ (mm)
Vivaldi	-12.90	28.86	-2.11	14.77
Vivaldi RA	-12.74	30.09	-4.15	19.42
Patch	-7.63	19.00	1.58	10.78
Dipole	-11.57	22.08	-6.16	24.60
Dipole Theory	-0.09	2.14	0.51	1.58

Table 5.5. Ranging algorithm comparison with asphalt surface.

Antenna	Chirp- z		TLS Prony	
	μ (mm)	σ (mm)	μ (mm)	σ (mm)
Vivaldi	-7.98	31.12	0.75	12.66
Vivaldi RA	-13.84	30.79	-2.55	20.21
Patch	-9.58	17.73	-1.16	3.47
Dipole	-11.20	21.24	-7.80	22.83
Dipole Theory	0.15	2.34	0.75	1.84

Table 5.6. Ranging algorithm comparison with dry soil surface.

Antenna	Chirp- z		TLS Prony	
	μ (mm)	σ (mm)	μ (mm)	σ (mm)
Vivaldi	-15.47	30.58	-4.00	16.6
Vivaldi RA	-12.17	28.11	-5.44	17.46
Patch	-6.77	18.97	3.00	12.48
Dipole	-12.47	23.01	-6.85	24.79
Dipole Theory	0.53	1.78	0.21	1.53

Table 5.7. Ranging algorithm comparison with wet soil surface.

Antenna	Chirp- z		TLS Prony	
	μ (mm)	σ (mm)	μ (mm)	σ (mm)
Vivaldi	-9.10	30.80	-2.04	13.86
Vivaldi RA	-10.73	29.71	-2.86	19.48
Patch	-9.67	17.81	-0.28	5.92
Dipole	-11.16	21.43	-8.20	23.28
Dipole Theory	0.07	2.38	0.67	1.92

Table 5.8. Ranging algorithm comparison with snow surface.

Antenna	Chirp- z		TLS Prony	
	μ (mm)	σ (mm)	μ (mm)	σ (mm)
Vivaldi	-17.21	39.69	-14.71	24.84
Vivaldi RA	-11.23	39.17	-10.48	23.44
Patch	0.13	28.59	0.93	23.52
Dipole	-2.32	27.52	-3.58	24.10
Dipole Theory	-0.56	14.83	-1.02	13.78

Table 5.9. Ranging algorithm comparison with copper surface without CW ranging.

Antenna	Chirp- z		TLS Prony	
	μ (mm)	σ (mm)	μ (mm)	σ (mm)
Vivaldi	-1.95	29.42	-3.58	18.47
Vivaldi RA	-2.17	26.99	-2.67	19.67
Patch	-0.98	18.76	-1.33	15.73
Dipole	-1.62	24.92	-1.72	23.72
Dipole Theory	-0.79	11.21	-0.76	11.00

Table 5.10. Ranging algorithm comparison with concrete surface without CW ranging.

The SRS Simulator is calibrated to the input of each antenna. Mean error shown in the tables can be attributed to several factors such as residual antenna phase (ψ) as well as from wavelength errors in the CW processing. Conceivably, the mean error would be removed during calibration for a real system, in which case standard deviation σ is equivalent to RMS error. It is interesting, particularly on the TLS Prony results, that the mean error is generally highest on metal. This is likely due to an increase in multipath signal strength on metal surfaces.

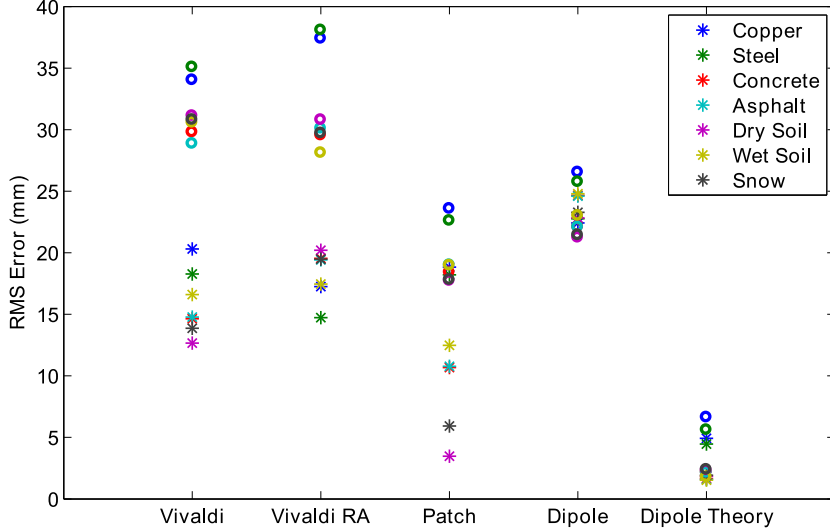


Fig. 5.5. Summary of SRS Simulator RMS range error across all surfaces. Chirp-*z* in circles and TLS Prony in *.

RMS error (i.e. standard deviation σ) results are summarized in Fig. 5.5. In Table 5.9 and Table 5.10, the ranging algorithms are shown without using CW phase for copper and concrete. On average, $\sim 20\%$ improvement in accuracy is found with using CW phase in the ranging solution. The Prony algorithm performs much better than the Chirp-*z* with errors below 2 cm for all antennas except the dipole. The theoretical dipole performs significantly better than the other antennas. This can be attributed to the polarization phase term producing ranging errors.

In Fig. 5.6 the LOS polarization phase is shown for each antenna at 6.95 GHz. The theoretical dipole has zero phase because of its polarization purity and the orientation of the antenna never moves beyond $\pi/2$ of its nominal. The dipole antenna switches between $\pm\pi$ because the antennas are inverted with respect to each other when mounted. Polarization purity of the dipole antenna is significantly affected by the integrated balun explaining its reduced ranging accuracy. The large peaks seen in the Vivaldi antennas correspond to when the shoe is swinging past the other shoe. The Vivaldi antennas are actually two antennas in an array and during this swing, nulls are experienced as the LOS path transitions between elements in the array.

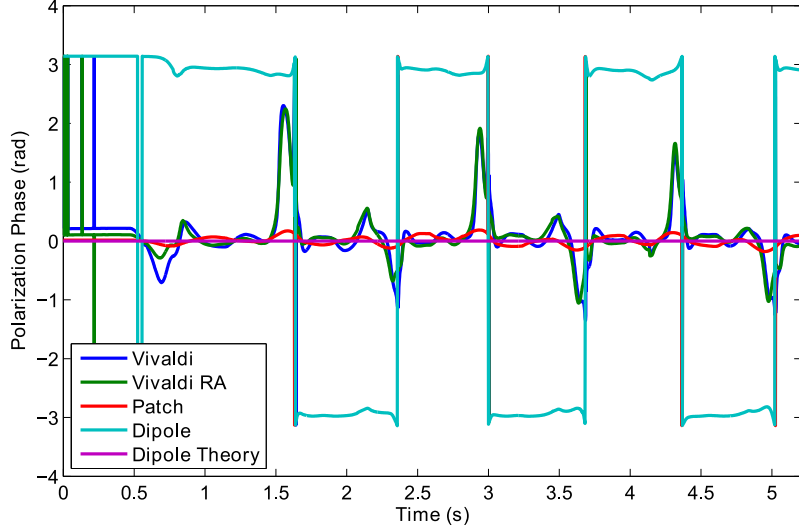


Fig. 5.6. SRS Simulator polarization phase for different antennas

5.3.2. METAL & CONCRETE

The following analysis will focus on concrete and copper results because concrete is the more common walking surface and metal is the worst case performance due to strong multipath. Also, there will be a focus on the Vivaldi antennas. Both the dipole and patch were found experimentally to have poor performance. The dipole's performance is expected from simulation; however the patch was predicated to have good performance in part due to its polarization purity. The patch had reliable ranging only when the antennas were closest, and the antenna gain was highest. This will be discussed more in chapter 7, but the poor patch performance is primarily due to lower SNR than simulated when the shoes are furthest apart because of antenna coupling to the mount. The Vivaldi antenna design maximizes antenna gain when the shoes are at their furthest leading to a more consistent SNR. In Fig. 5.7, the time domain envelope peak power from the Chirp- \mathcal{Z} is compared for patch and Vivaldi antennas on concrete. The Vivaldi signal power has a standard deviation of 6.5 dB versus 12.7 dB with the patch.

Range plots for concrete and metal are shown in Fig. 5.8. Between 0-0.6 s, the shoes are adjacent to each other. This is one of the worst locations for the Vivaldi antennas because the gain is lowest

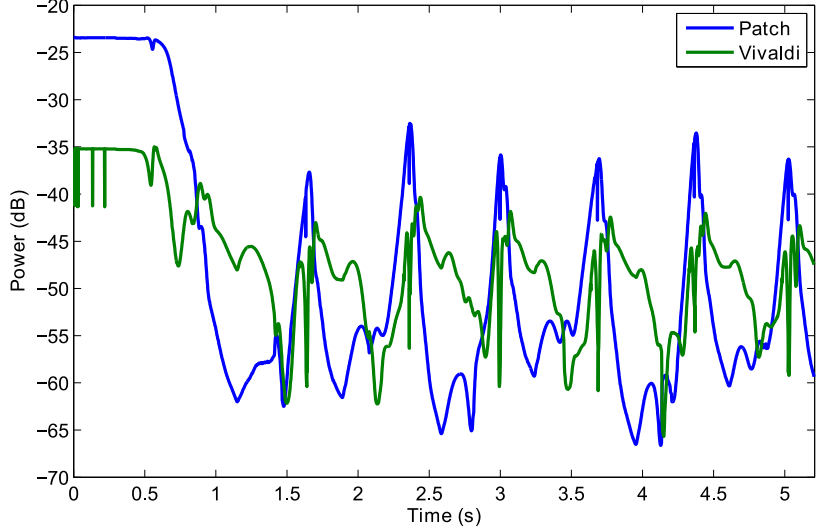


Fig. 5.7. SRS Simulator peak power of time domain envelope (Chirp- z) on concrete.

and there are several nulls near this position. Additionally, the NLOS path difference is fairly large and strong (Fig. 5.4). The Prony method is nonetheless able to generate an accurate range in this region, whereas the Chirp- z has significant difficulties due to the multipath. As expected, there are large range errors when the shoe swings past each other (1.5 s, 3 s, 3.75 s, 4.4 s) and travels through the nulls of the Vivaldi.

At 4 s on the concrete surface, the Prony method has a significant range error. This is due to improper CW wavelength selection from an error in the smoothing algorithm – it appears to recover soon after. Another feature to notice is there are glitches in the range on the falling edges (1.4 s, 2.2 s, 2.8 s, 3.5 s, 4.2 s, 4.8 s). At this point in the step, the rear-most shoe is lifting off the ground and the heel is moving to its peak height and max pitch placing the antenna at an odd angle. The metal has more consistently bad ranges at the peaks. Metal results in little to no attenuation after reflection and with R_{LOS} and R_{NLOS} ranges so close to each other (Fig. 5.4), the NLOS signal is strongly biasing the range solution.

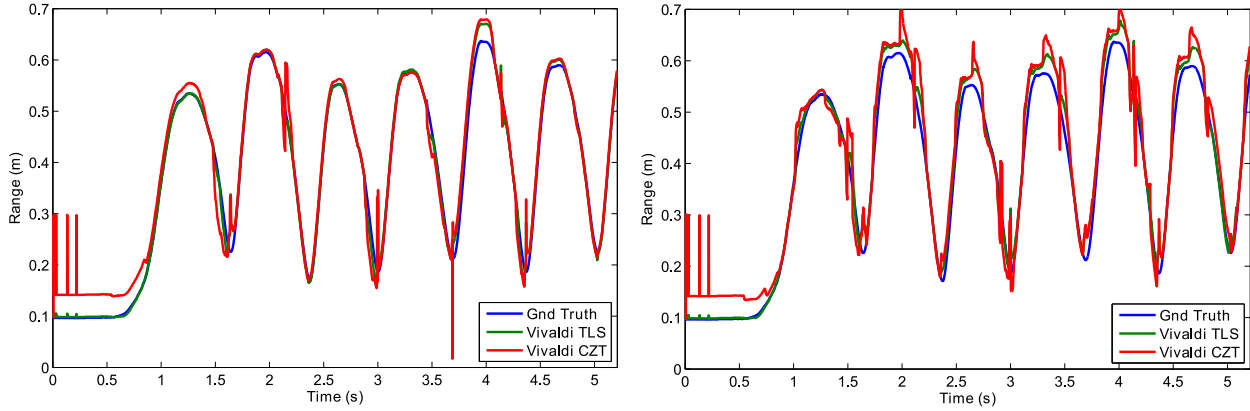


Fig. 5.8. SRS Simulator range solutions for concrete (left) and metal (right). TLS is Prony method and CZT is Chirp- z method.

5.3.2.1. PERFORMANCE ENHANCEMENT

Antenna	Surface	Chirp- z		TLS Prony	
		μ (mm)	σ (mm)	μ (mm)	σ (mm)
Vivaldi	Copper	-25.16	32.83	-13.42	18.18
Vivaldi clipped	Copper	-27.03	34.84	-16.98	18.09
Vivaldi	Concrete	-10.55	26.07	-0.23	10.69
Vivaldi clipped	Concrete	-0.30	19.01	-0.13	6.19

Table 5.11. Ranging algorithm comparison with optimal sweep, and location clipping (<0.3 m).

There are a couple of enhancements that can be made to further reduce the range error. One is reordering the frequency sweep. Instead of linearly increasing the frequency from low to high $[f_0 \ f_1 \dots f_{N-2} \ f_{N-1}]$ the sweep may be arranged with even frequencies up and odd frequencies down $[f_0 \ f_2 \ f_4 \dots f_3 \ f_1]$. The shoe is in motion during the frequency sweep and the alternating pattern may diminish the motion blur by interspersing measurements among high and low frequencies. Another benefit of this sweep configuration is that it reduces the settling time of the VCO when the sweep restarts. Care must be taken to make sure the measurements are reordered with linear frequency before range processing. This effect has not been tested in hardware yet, so it is not clear to what extent it helps performance.

The other enhancement has been discussed in chapter 4 and is using antenna location to filter out known low accuracy regions. A basic version is implemented in Fig. 5.9 and Table 5.11. This

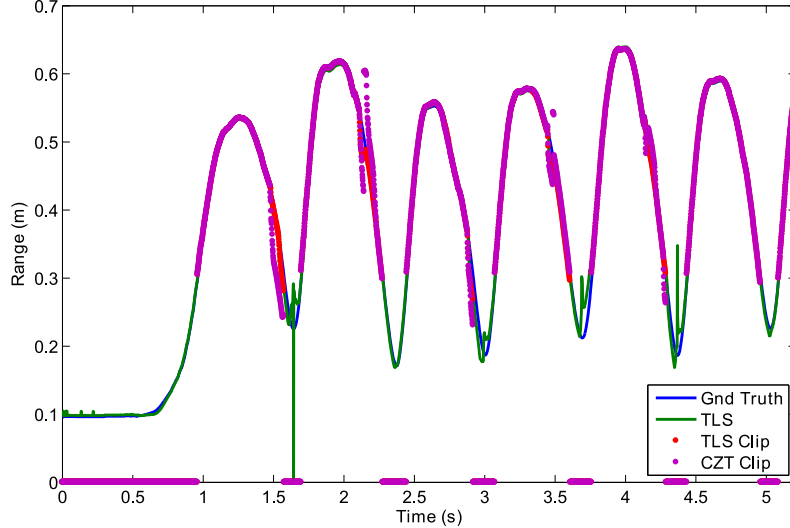


Fig. 5.9. SRS Simulator range solutions for concrete with optimal frequency sweep and location clipping ($R < 0.3$ m). TLS is Prony method and CZT is Chirp- ζ method.

simply sets the range to 0 if the ground truth is below 0.3 m. Clearly, for the Prony method, this filter is too aggressive as there are good ranges < 0.3 m, especially from 0-1 s. The SRS does not necessarily perform poorly at close ranges, just in certain regions of the antenna pattern. A smarter filter would base the rejection criteria on the vector range rather than the scalar range.

5.3.2.2. MULTIPATH ANALYSIS

In Fig. 5.10, the channel response in spectral and time domains is shown for two different locations in the step – shoes furthest apart (left) and shoes swinging passing each other (right). The surface is concrete with the Vivaldi antennas and a linear frequency sweep. Each channel response is decomposed into the LOS and NLOS signals. In addition, the Prony solutions are shown as delta functions in the time domain response. The close range solution (2.365 s) Prony estimates are similar to the actual LOS and NLOS components. For the far range solution (1.9483 s), the Prony estimates exaggerate the path difference and the amplitude coefficients seem mixed up. The simulator was set to $m=2$ so the Prony algorithm would calculate the coefficients on the NLOS path. Increasing m from 1 to 2 greatly increases range error, exceeding the Chirp- ζ error.

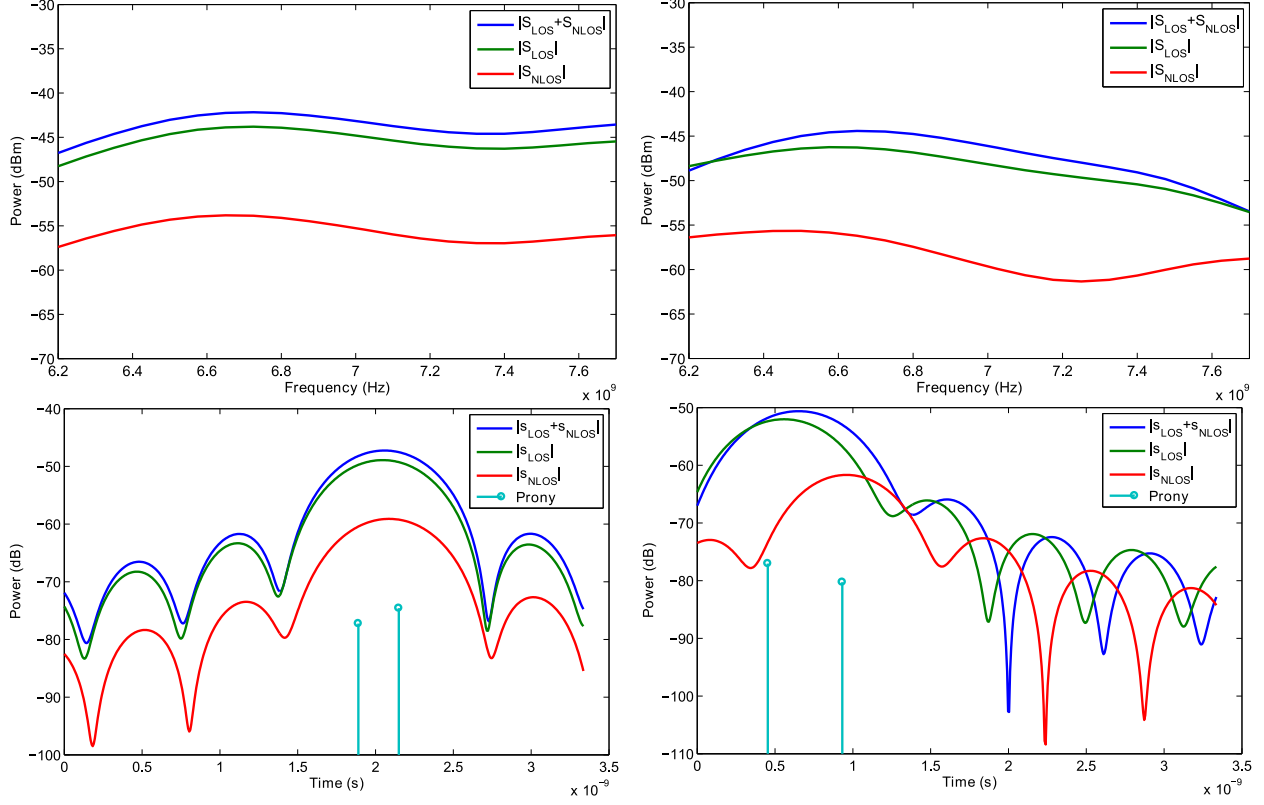


Fig. 5.10. SRS Simulator channel response at 1.9483 s (left) and 2.365 s (right) on concrete with Vivaldi antenna. Top figures are channel spectral response and bottom are Chirp- z time domain response each decomposed into LOS and NLOS signals. Prony solutions plotted as delta functions in bottom figures.

The Prony model assumes the amplitude coefficients of the channel are frequency independent and the phase term only depends on range. As modeled, the SRS channel has frequency dependent amplitude coefficients from path loss and antenna gain and the signal phase has an additional polarization phase term that is also frequency dependent. This explains why the Prony technique has trouble separating the multipath components. In Fig. 5.11, the Prony computed LOS and NLOS range without CW phase are shown along with the ground truth ranges. The LOS and NLOS Prony solutions are selected based on largest range (NLOS>LOS) and show a broad similarity to the ground truth.

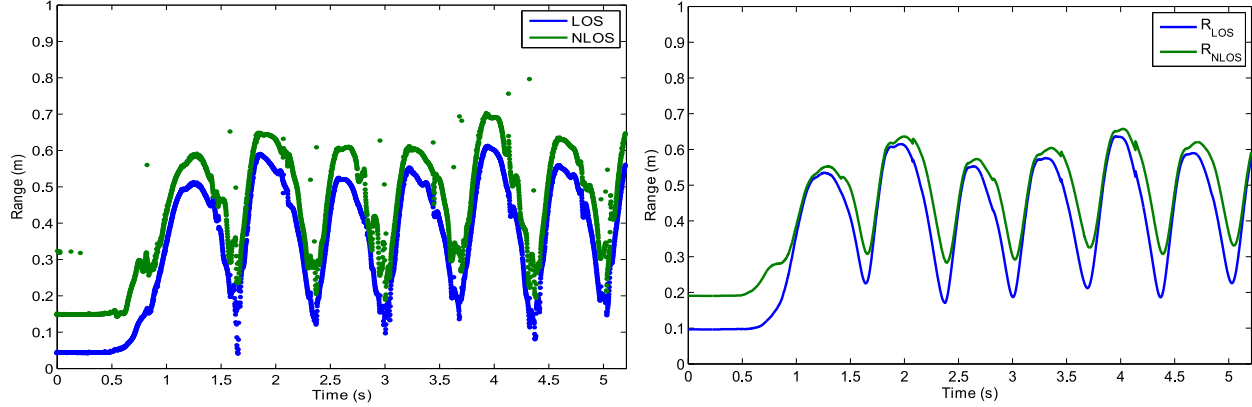


Fig. 5.11. SRS Simulator Prony LOS and NLOS range solutions for concrete and Vivaldi Antenna (left). Ground truth range for LOS and NLOS (right).

5.3.3. MULTI-RANGER SIMULATION

The multi-ranger extension as described in 5.1.2 requires the definition of a few additional parameters. In Table 5.12, the additional simulation settings for the multi-ranger are shown, sweep rate, bandwidth etc. remain the same as before. The antenna positions are relative to each shoe's IMU whose coordinates are shown in Fig. 5.1. The coordinates chosen along with the RF cable lengths were taken from the hardware implementation. Antennas A1 and A3 are the same used in the previous simulations (in section 5.3.1 and 5.3.2).

Results for concrete and copper using the Vivaldi antenna are shown in Table 5.13 - Table 5.16. Overall, the effect of finite switch isolation is fairly minimal on the RMS error. As before, the best Prony results were with $M = 3$ and $m=1$, and consistently performs better than the Chirp- z despite the model mismatch. The RMS error results are summarized in Fig. 5.12. Example ranges are shown in Fig. 5.13.

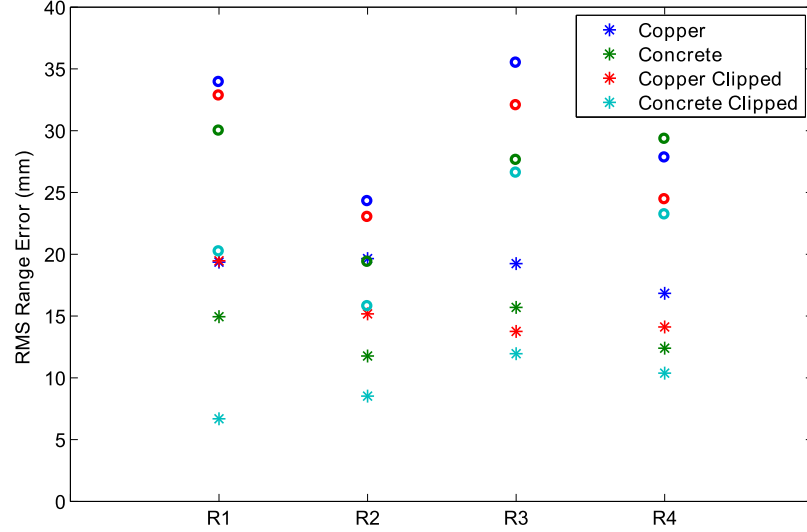


Fig. 5.12. Summary of SRS Multi-Ranger Simulator RMS range error on copper, concrete along with optimal frequency sweep and 0.3 m range clipping. Chirp- z in circles and TLS Prony in *.

Parameter	Value
A1 Position (IMU Frame)	(0.052, .0168, 0.022) m
A2 Position (IMU Frame)	(0.052, .0498, -0.232) m
A3 Position (IMU Frame)	(-0.052, .0168, 0.022) m
A4 Position (IMU Frame)	(-0.052, .0478, 0.225) m
$L_{c_1} + L_{c_2}$	0.708 m
$L_1 + L_3$	0.314 m
$L_1 + L_4$	0.524 m
$L_2 + L_3$	0.575 m
$L_2 + L_4$	0.784 m
v_p	83 %
Switch attenuation (A)	41 dB

Table 5.12. SRS Multi-Ranger Simulator settings.

Range	Chirp- z , A=∞		Chirp- z , A=41 dB		Prony, A=∞		Prony, A=41 dB	
	μ (mm)	σ (mm)	μ (mm)	σ (mm)	μ (mm)	σ (mm)	μ (mm)	σ (mm)
R₁	27.61	33.81	29.54	33.92	14.73	20.35	19.40	19.36
R₂	15.78	24.19	14.11	24.28	14.04	20.16	13.29	19.65
R₃	23.83	35.68	22.18	35.48	19.89	20.05	19.49	19.24
R₄	19.10	30.73	18.47	27.81	13.24	21.35	13.05	16.84

Table 5.13. Algorithm comparison of multi-ranging on copper surface with Vivaldi antenna and ideal vs. leaky switch.

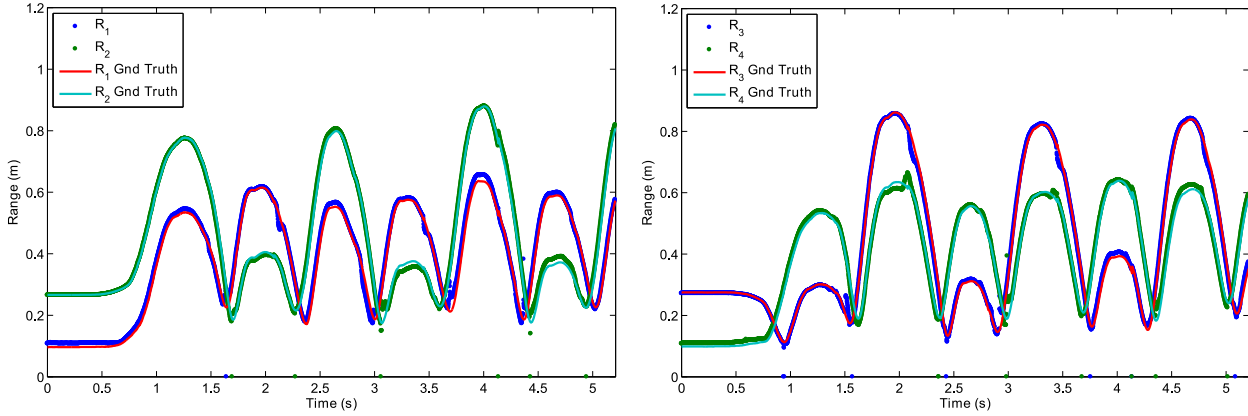


Fig. 5.13. SRS Multi-Ranger Simulator Prony range solutions on concrete with optimal frequency sweep and Vivaldi antennas.

Range	Chirp- z , A=∞		Chirp- z , A=41 dB		Prony, A=∞		Prony, A=41 dB	
	μ (mm)	σ (mm)	μ (mm)	σ (mm)	μ (mm)	σ (mm)	μ (mm)	σ (mm)
R_1	27.08	34.75	30.34	32.82	16.98	18.09	20.06	19.47
R_2	11.57	22.98	11.69	23.00	8.83	17.87	9.32	15.17
R_3	29.04	33.49	27.33	32.04	24.95	16.98	23.17	13.75
R_4	19.45	23.77	18.44	24.43	14.91	14.78	11.68	14.11

Table 5.14. Algorithm comparison of multi-ranging on copper surface with Vivaldi antenna and ideal vs. leaky switch. Optimal frequency sweep with 0.3 range clipping used.

Range	Chirp- z , A=∞		Chirp- z , A=41 dB		Prony, A=∞		Prony, A=41 dB	
	μ (mm)	σ (mm)	μ (mm)	σ (mm)	μ (mm)	σ (mm)	μ (mm)	σ (mm)
R_1	10.57	29.94	15.12	29.98	2.02	14.65	6.73	14.94
R_2	6.83	20.93	4.43	19.37	4.11	11.69	1.66	11.77
R_3	-2.37	28.31	1.76	27.61	0.56	13.01	3.38	15.70
R_4	11.20	31.92	10.05	29.32	2.43	10.01	3.83	12.40

Table 5.15. Algorithm comparison of multi-ranging on concrete surface with Vivaldi antenna and ideal vs. leaky switch.

Range	Chirp- z , A=∞		Chirp- z , A=41 dB		Prony, A=∞		Prony, A=41 dB	
	μ (mm)	σ (mm)	μ (mm)	σ (mm)	μ (mm)	σ (mm)	μ (mm)	σ (mm)
R_1	-0.01	18.89	1.36	20.21	0.12	6.22	-0.49	6.68
R_2	2.85	15.96	3.16	15.78	2.51	8.77	2.50	8.52
R_3	2.87	26.36	0.25	26.59	4.01	11.50	2.27	11.95
R_4	-1.62	23.42	-3.27	23.21	4.35	10.07	1.75	10.38

Table 5.16. Algorithm comparison of multi-ranging on concrete surface with Vivaldi antenna and ideal vs. leaky switch. Optimal frequency sweep with 0.3 range clipping used.

5.3.3.1. SWITCH ATTENUATION

A sweep of switch isolation A from 0-41 dB was performed using the SRS Multi-Ranger Simulator configured with the concrete surface, Vivaldi antennas, optimal frequency sweep and 0.3

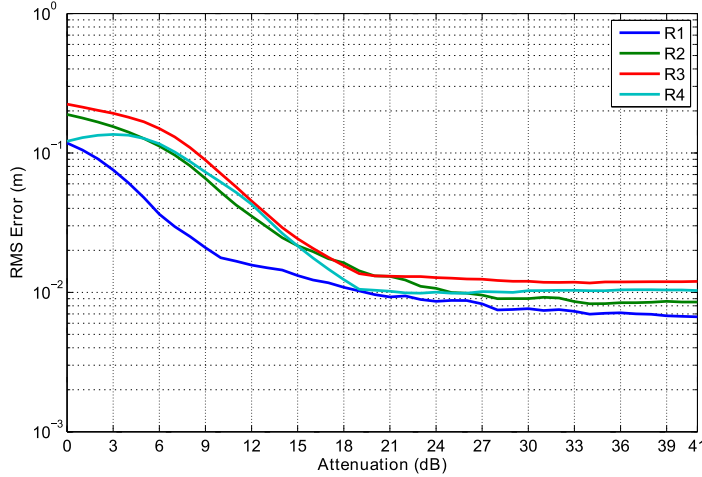


Fig. 5.14. Effect of non-ideal switch isolation on Prony RMS error. SRS Multi-Ranger Simulator on concrete with optimal frequency sweep and Vivaldi antennas.

range clipping. In Fig. 5.14, the RMS error of the Prony range solution is shown versus isolation.

The range error starts to level off at about 21 dB and is fairly flat beyond 30 dB.

5.4. SUMMARY

The SRS Simulator found the best ranging performance when using the Prony algorithm along with location based range rejection. Sub-cm RMS error is attainable and possibly even lower error with smarter range filtering. The Prony method performs well despite the model mismatch. Finally, the impact of non-ideal RF switches in the multi-ranger is minimal with at least 30 dB isolation.

CHAPTER 6

6. SRS HARDWARE

The design of the SRS hardware focused on an architecture that minimizes power. Implementation of this architecture was limited to COTS components so this prototype does not achieve low power consumption. Subsequent development of an integrated circuit (IC) implementation will be able to realize the full potential of the design. This chapter will discuss the transceiver, FPGA (field programmable gate array) data acquisition, and antennas designed for the SRS.

6.1. SRS TRANSCEIVER

A homodyne transceiver was chosen because it requires the fewest components and allows lower sampling rate analog-to-digital converters (ADCs) as compared to a heterodyne design. The drawback of using a homodyne transceiver is finite mixer isolation results in dc feedthrough signals. A simple calibration procedure can remove this feedthrough signal – see chapter 7. Fig. 6.1 shows a block diagram of the SRS Multi-Ranger (single range system excludes the switches and uses two antennas). A Hittite VCO (HMC505) with tuning bandwidth 6.2 – 7.7 GHz and an output power of +11 dBm serves as the local oscillator (LO). An in-house designed Wilkinson splitter sends \sim +7 dBm to the transmit antenna(s) and the LO port of the quadrature mixer (Hittite HMC520). S-

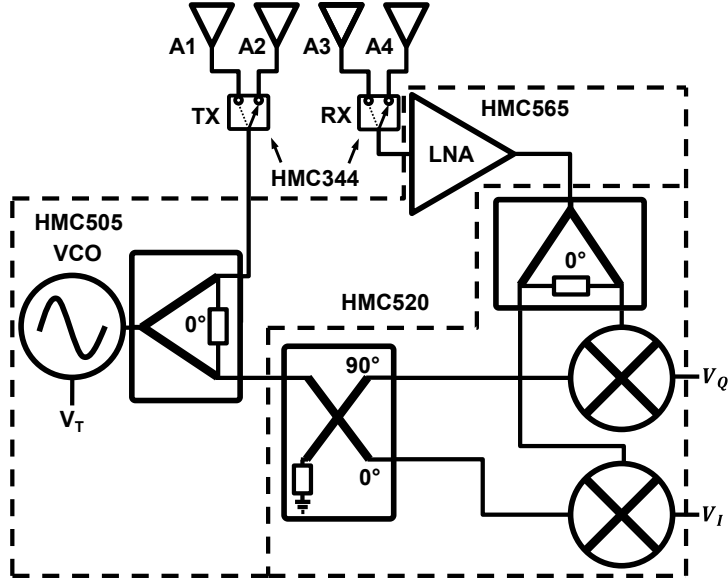


Fig. 6.1. Block diagram of SRS Multi-Ranger transceiver architecture – outer dashed box contains components in dashed area of PCB (Fig. 6.3).

parameters of a connectorized version of the Wilkinson splitter are shown in Fig. 6.2. A low-noise amplifier (Hittite HMC565) with 6-20 GHz bandwidth and 21 dB of gain connects the receive antenna(s) to the quadrature mixer. Power consumption of the transceiver is about 400 mW with a 3 V supply.

The SRS Transceiver PCB (printed circuit board) shown in Fig. 6.3 also contains power filtering and single-ended to differential op-amp circuits for the $V_{I,Q}$ channels. The op-amp circuit brings the ± 0.5 V peak output of the mixer to a 0.5 – 4.5 V differential level expected by the ADCs and also integrates a low pass filter (~ 800 kHz single pole). An EMI (electromagnetic interference) can is placed on top of the RF components to further reduce noise. Measured noise at the output of the op-amps, with 50Ω terminators on the TX and RX ports, was determined using an Agilent 34401A multimeter (3-300 kHz bandwidth) and is -115 dBFS (dB full scale) with the EMI can and -102 dBFS without. Motion around the board (such as waving one's hand) can slightly increase the noise floor (-103 to -107 dBFS). Mechanical stress should be avoided as sharp impacts with a table

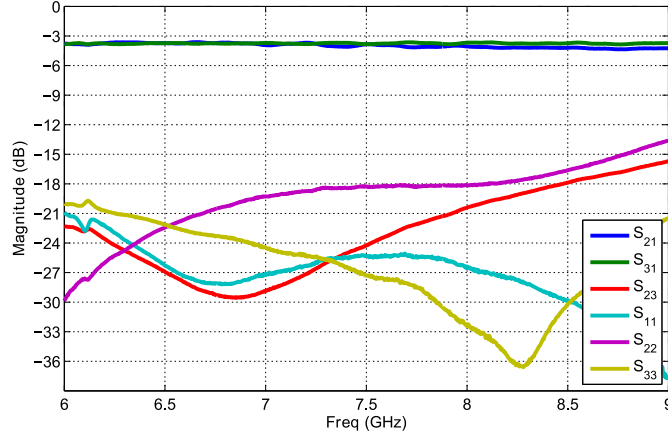


Fig. 6.2. S-parameters of Wilkinson splitter – port 1 connects to VCO, port 3 to the transmit antenna and port 2 to the mixer.

resulted in impulse noise spikes up to -33 dBFS, though some of this signal may be due to the connectors used in the measurement.

Board stackup of the transceiver PCB consists of 10 mils of Rogers RO4350 for the RF components with 3 layers of FR4 for a total thickness of 65 mil. Total board dimension are 2.125" x 2.125". Considering the dimensions of the EMI can (25.4 x 38.1 x 6 mm) and the PCB thickness of 65 mil, total volume of the RF transceiver is 7.4 cc.

A SP4T RF switch (Hittite HMC344LH5) is mounted on each shoe for the SRS Multi-Ranger. Though only two signal paths are used in this work, the switch has four paths to allow future expansion. Internally, all inactive switch paths are terminated to 50Ω . In addition, the unused ports are externally terminated with 50Ω to protect the connector. The switch has a 75 ns response time from a transition on the control input and ~ 41 dB of isolation between switch paths in the band of interest. Control of the switch is through 2.5 V LVDS (low-voltage differential signaling) synchronized to the VCO tuning voltage.

A brief literature review of recent RF IC power consumption found that the SRS Transceiver architecture shown here including ADC sampling and range processing could use < 50 mW of power

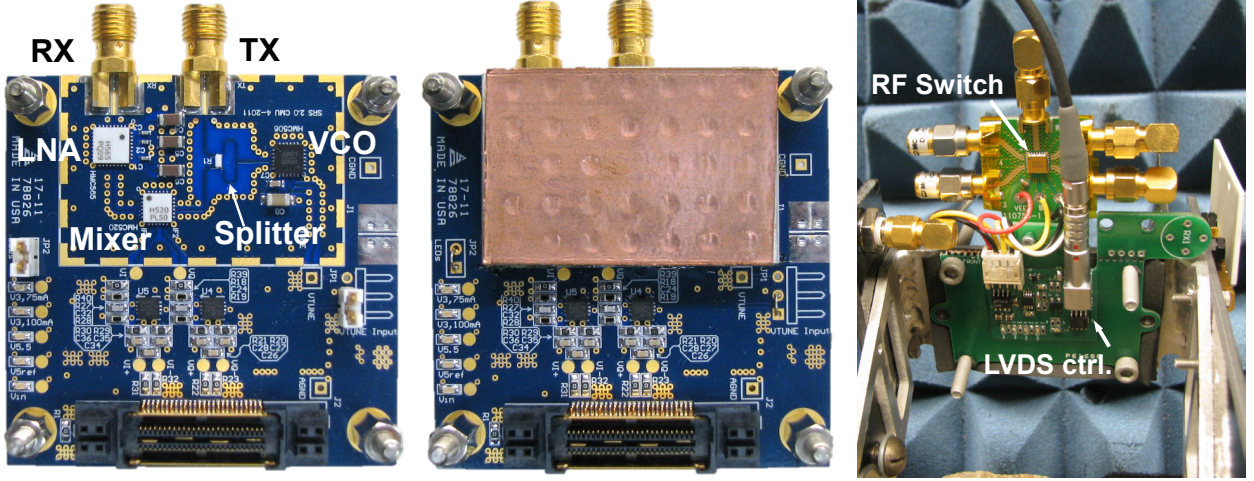


Fig. 6.3. SRS Transceiver PCB (left and middle) – left shows without EMI can. RF switch and LVDS control board (right).

in an optimized design. This assumes 3.12 mW for a VCO [38], 18 mW in a wideband receiver [39], 2x0.18 mW for ADCs [40] and 9.5 mW to compute a complex 1024-point fast Fourier transform [41] in <1 ms.

6.2. FPGA DATA ACQUISITION

The 18-bit 1.6 MS/s ADCs (Linear Tech. LTC2379-18) selected to sample the $V_{I,Q}$ signals required a custom FPGA board to be designed due to their high-speed 100 MHz SPI (serial-peripheral interface) bus connection. The FPGA is a Xilinx Spartan LX45 with a 100 MHz TCXO (temperature compensated crystal oscillator) reference clock. Memory available to the FPGA is 128 MB of DDR3 667 MHz SDRAM, 8 MB of SPI Flash PROM and 32 MB of BPI Flash PROM. I/O interfaces to the FPGA include gigabit Ethernet, one HDMI connector for custom high-speed LVDS connections, a MMCX connection for external clock I/O and a general purpose expansion header. An onboard temperature sensor (TI TMP431) is also available and located above the VCO for monitoring potential frequency drift from temperature changes. Dimensions of the FPGA board are 99.5 x 76.5 mm with height ~22 mm excluding connectors (Fig. 6.4). Power is supplied by 5 V

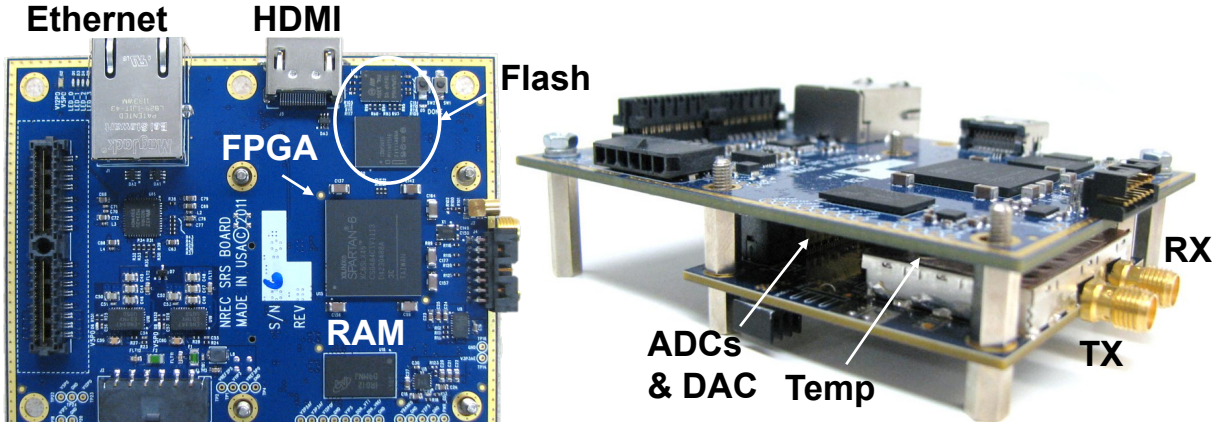


Fig. 6.4. FPGA Data Acquisition board top and side view with SRS Transceiver board attached.

and 12 V connections. Total operating current for the FPGA and transceiver board is 0.7 A on the 5 V rail (3.5 W) and 0.16 A on the 12 V rail (1.92 W).

VCO tuning voltage (V_T) on the SRS Transceiver is controlled with a Linear Technology LTC2641 16 bit DAC (digital-to-analog converter). An op-amp sets the scale from 0-11 V with 800 kHz of bandwidth. The FPGA synchronously sets the DAC code with the RF switch code. RF switch control is through the HDMI port using 2.5 V LVDS.

Data acquisition on the FPGA is controlled by custom logic and a MicroBlazeTM soft microprocessor. The custom logic steps through DAC/switch codes of a SFCW sweep, samples the ADCs and applies block averaging to the ADC samples. ADCs are operated at maximum rate (1.6 MHz) and block averaged down to the requested sample rate (12.6 kHz) to reduce noise. The first 75 ADC samples after a DAC code change are discarded to compensate for VCO settling time. The MicroBlazeTM controls sweep repetition rate, accepts commands over Ethernet, and sends the data from completed sweeps across the Ethernet interface. Default sweep settings can be saved on the SPI Flash and loaded by the MicroBlazeTM on power-up. Acquisition status (run/stop) is transmitted as a logic high/low on the MMCX connector for synchronization with external equipment. Matlab is

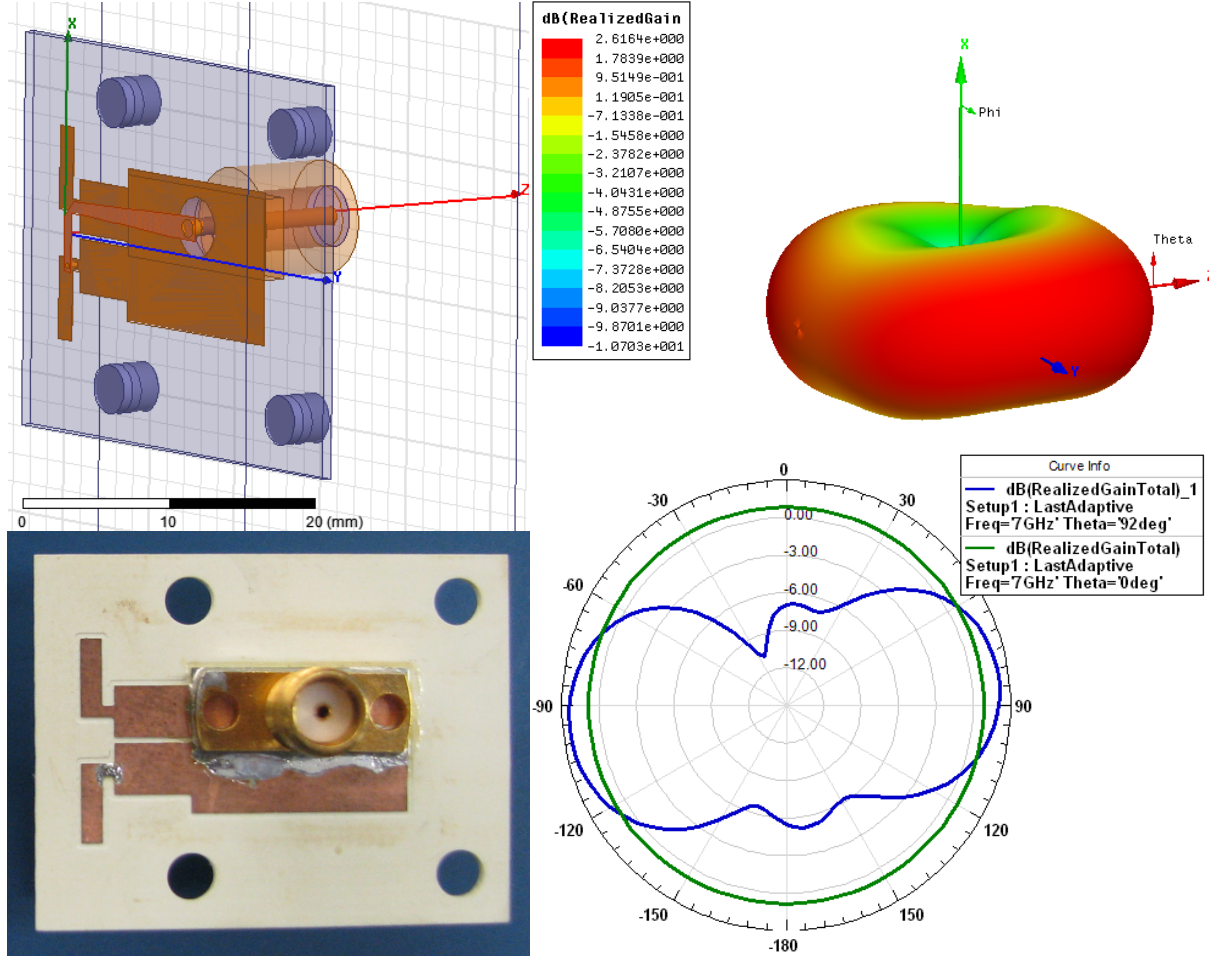


Fig. 6.5. 7 GHz dipole antenna with integrated balun (left). 3D and 2D gain plots (right).

used to send commands and record data over a UDP (user datagram protocol) connection with the FPGA board.

6.3. ANTENNAS

Three antenna types were simulated in Ansoft HFSS and fabricated using a custom built PCB mill machine. An overview of each design along with simulated gain pattern and measured S-parameters will be presented. The first two antennas were chosen because of their pure polarization characteristics. The last antenna was chosen due to its optimal gain pattern for the SRS and wide bandwidth.

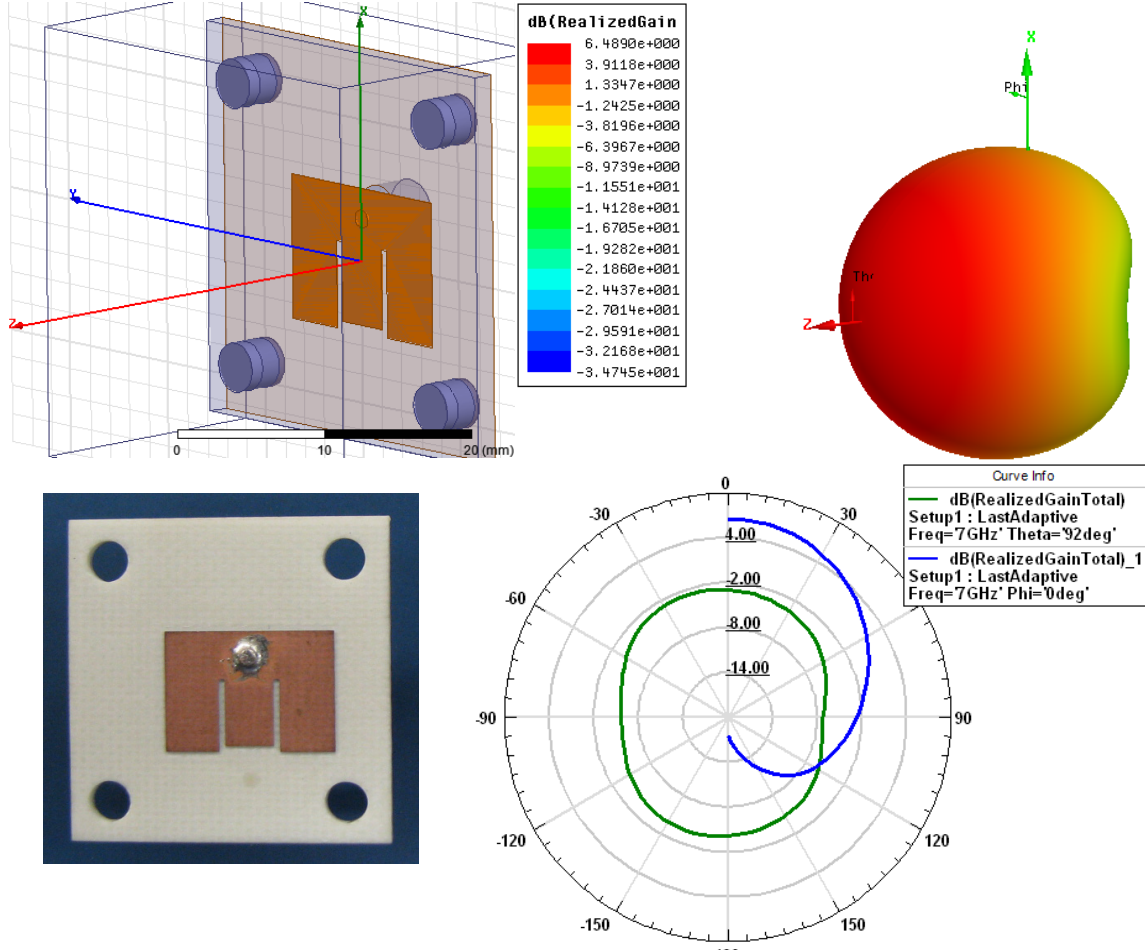


Fig. 6.6. E-shaped patch antenna (left). 3D and 2D gain plots (right).

6.3.1. DIPOLE WITH BALUN

In [42], a printed dipole with integrated balun is described. The design was modified for 7 GHz center frequency, SMA probe feed and Rogers RO4350 substrate. Peak gain is 2.6 dB and measured 6.65-7.34 GHz impedance bandwidth. Fig. 6.5 shows the fabricated antenna and 3D gain and 2D gain cut planes. The substrate dimensions are 35.2 x 27.5 mm with 30 mil thickness. A 2 cm spaced drill pattern is used for mounting. Measured S-parameters of all three antennas using an Agilent E8358A VNA are compared in Fig. 6.9.

Gain is omnidirectional so there is no part of the step that is favored with this antenna. This antenna had poor measured performance with the SRS hardware. Possible reasons are interaction

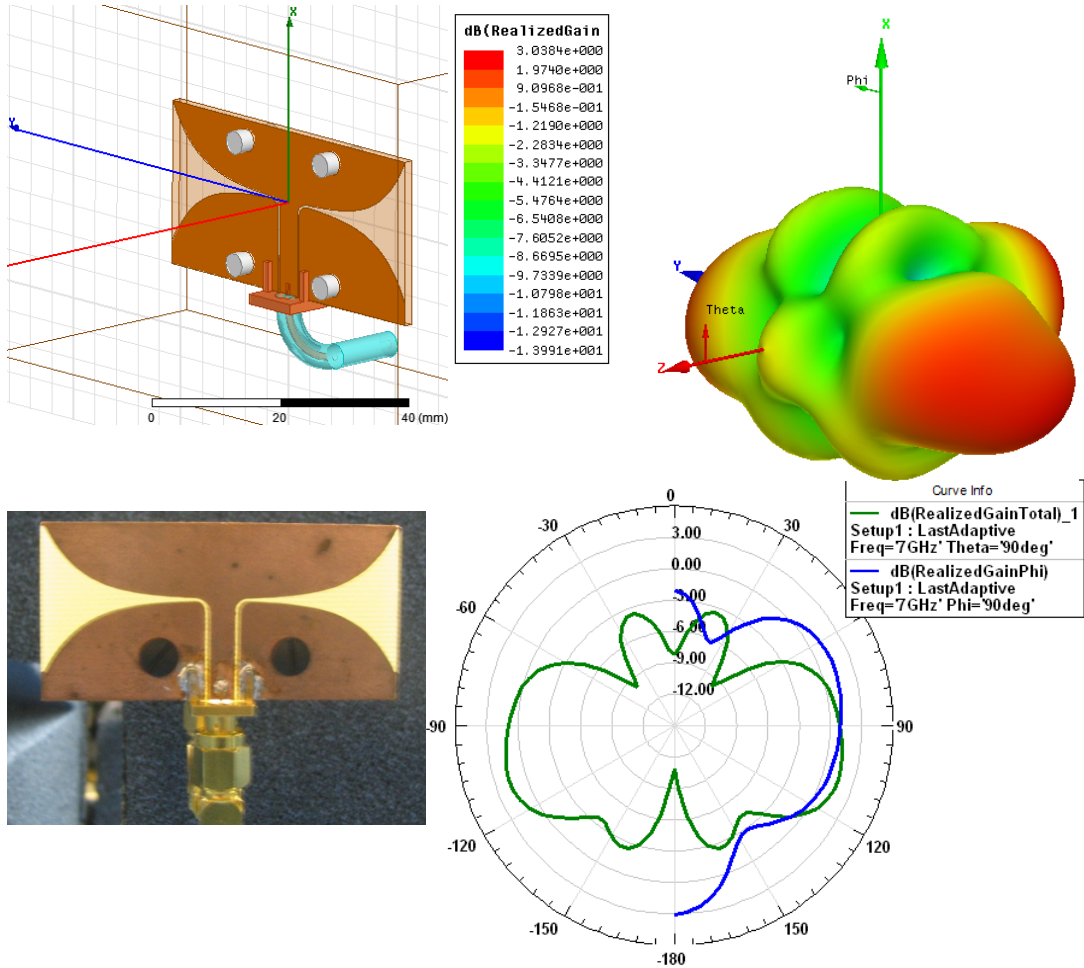


Fig. 6.7. Vivaldi antenna with right angle feed (left). 3D and 2D gain plots (right).

with the mount and the integrated balun with SMA feed are of similar size as the radiating arms resulting in degraded polarization purity.

6.3.2. E-SHAPED PATCH ANTENNA

The E-shaped patch, described in [43], is an interesting design that enhances the poor inherent bandwidth of a patch antenna by adding a couple of slots to create another resonant frequency. This patch antenna can easily be mounted conformal to the shoe and the ground plane should reduce the chance of coupling with objects behind the antenna. The antenna was designed on Rogers RO4003 and has a measured impedance bandwidth of 6.85-7.5 GHz (Fig. 6.9) and a simulated peak gain of

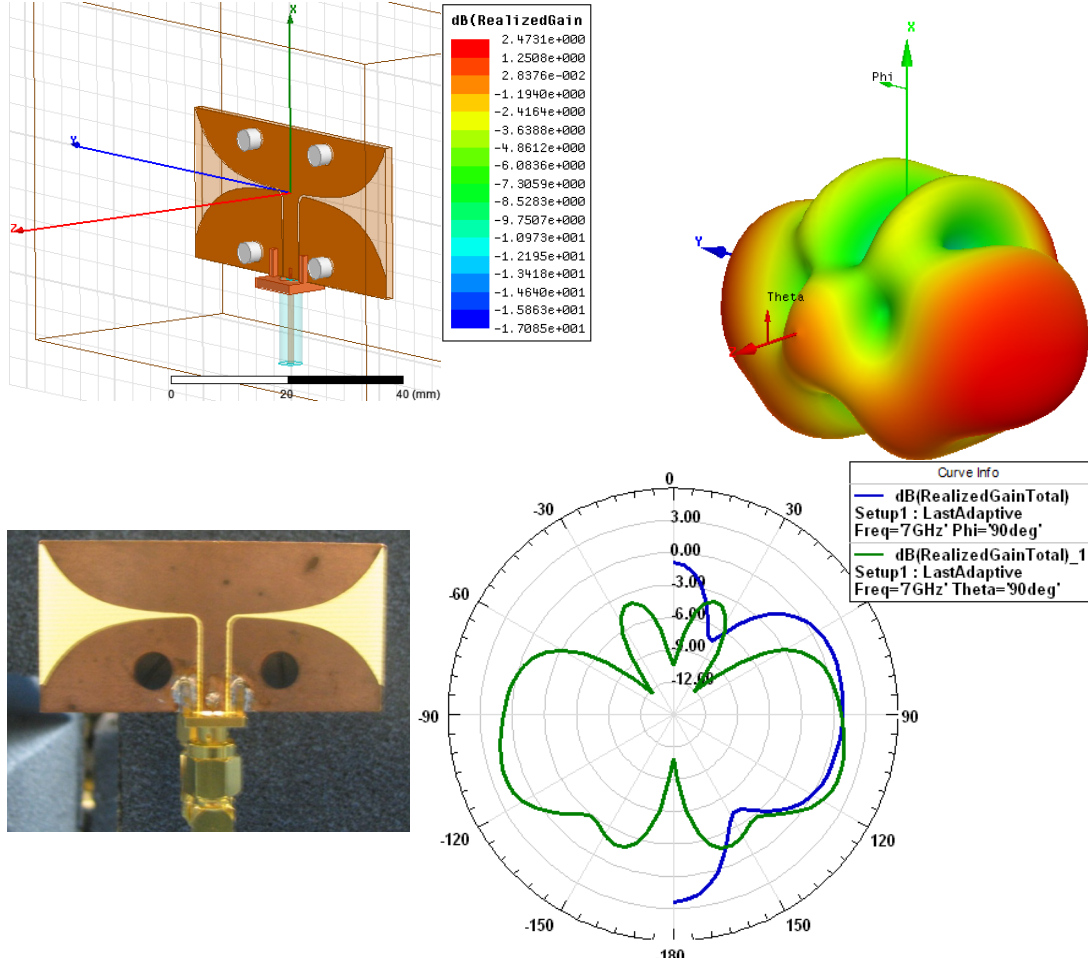


Fig. 6.8. Vivaldi antenna with straight feed (left). 3D and 2D gain plots (right).

6.49 dB. Fig. 6.6 shows gain plots and a picture of the fabricated antenna. Substrate dimensions are 2.75 x 2.75 cm with 60 mil thickness. Mounting holes are again spaced by 2 cm.

When mounted on the shoe, the patch antenna faces the opposite shoe while standing. This provides strong signal while standing and when the shoe swings past the other. Both of these conditions are rare and short term for a pedestrian, so the antenna gain pattern is sub-optimal for the SRS. Nonetheless, the polarization purity of the patch should help with the ranging performance as shown in chapter 5. Measured performance with this antenna was only acceptable when the shoes were close. It is suspected that the finite ground plane and the dielectric characteristics of the flat bar the antenna was mounted to corrupted the antenna pattern.

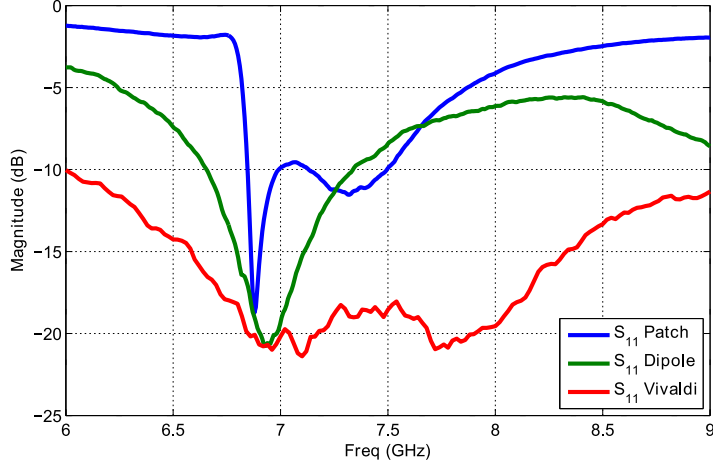


Fig. 6.9. S-parameters of patch, dipole and Vivaldi antennas.

6.3.3. VIVALDI ANTENNA

The Vivaldi antenna design is well suited to the SRS application. Maximum gain is in the endfire configuration, along the direction of the PCB plane. An array of two Vivaldi antennas back to back generates gain in the forward and backward directions. This maximizes the antenna gain when the shoes are furthest apart and the channel path loss is greatest.

Vivaldi antennas typically require a complicated feed network for wide bandwidth operation. Linardou et al. [44], describe a novel design in which the Vivaldi is fed by converting a coplanar waveguide to two slotlines that exponentially taper to form a two element array antenna. Two versions of the Vivaldi antenna were simulated in HFSS; a straight and right angled coaxial feed. The right angle fed Vivaldi is shown in Fig. 6.7. Null depths and gain change slightly for the straight coaxial feed.

The fabricated antenna has dimensions 26.7 x 54.1 mm on a 60 mil substrate. Both FR4 and Rogers RO4003 were used as substrates. Peak gain is about 3 dB and measured bandwidth is 6 – 9 GHz (Fig. 6.9), with the upper end limited by the VNA measurement range. Measured results of the Vivaldi with the SRS showed good performance throughout the step. Range errors were greatest

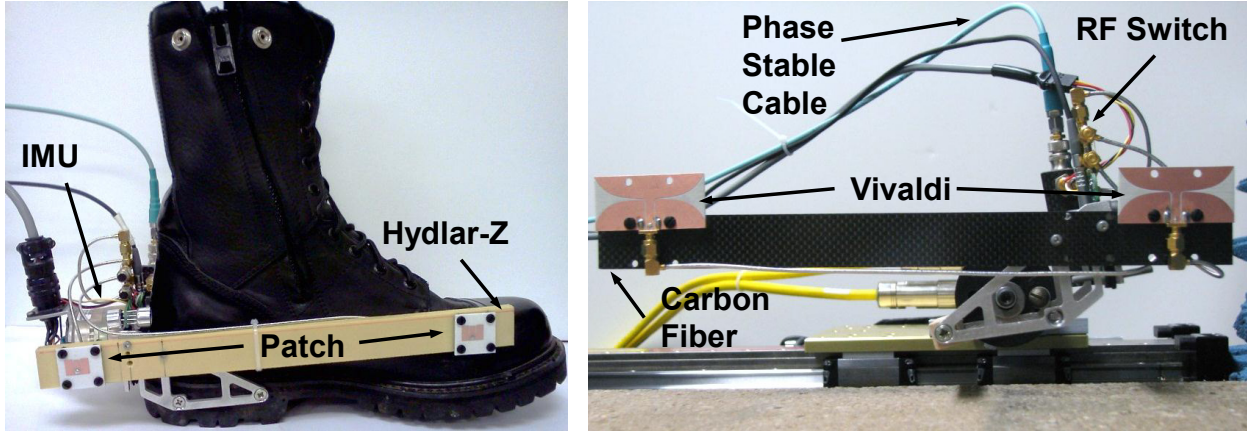


Fig. 6.10. Patch antennas on Hydlar-Z mount on shoe with IMUs (left). Rogers RO4003 Vivaldi antennas mounted with carbon fiber on the motion stage (right).

when the shoes moved past each other and the LOS signal path went through the nulls of the Vivaldi. This is also the region where the signal transfers from one element of the array to the other.

6.4. ANTENNA MOUNTING

For walking tests, the SRS Multi-Ranger hardware (transceiver and FPGA board) is mounted in a backpack along with a battery and other navigation components to operate the IMUs. Phase stable RF cables (Micro-Coax UFA147B) and shielded twisted pair cables for the RF switch run down to each shoe. Motion stage tests mount the transceiver and FPGA board on a table with power from bench power supplies.

The shoe mount for the antennas consists of a metal (aluminum) frame that is screwed into the sole of the shoe. This mount also holds the IMU and the RF switch boards. A 12" x 1" flat bar is attached to the metal frame and used to hold the antennas in position. Two different flat bars were used; 1/8" carbon fiber and 1/4" Kevlar-Nylon composite (Hydlar-Z). The Hydlar-Z was expected to have better antenna performance due to its low-loss dielectric properties. Experimental results showed the carbon fiber to be superior, both in rigidity and antenna performance. Carbon fiber is known to be a lossy material due to its conductivity. One explanation for the better antenna

performance is the carbon fiber absorbs radiation and reduces multipath reflections off the metal mount. The Vivaldi antenna is mounted slightly above the centerline of the bar and uses ~ 5 mm of spacers (see Fig. 6.3) because the carbon fiber absorption strongly changes the impedance bandwidth and ranging performance when the antenna is centered. Fig. 6.10 shows the antennas mounted on both carbon fiber and Hydlar-Z. Custom length flexible semi-rigid coaxial cables (Belden 1671A/RG405) connect each antenna to the RF switch.

CHAPTER 7

7. SRS MEASUREMENTS

This chapter will evaluate the ranging performance of the SRS hardware in a laboratory setting. Methods to calibrate the range and hardware errors will also be discussed. Ranging performance will be evaluated using the SRS Multi-Ranger for short and long term motion and compared to simulation. Finally, preliminary walking data with the SRS integrated on boots will be shown.

7.1. CALIBRATION

There are multiple steps to calibrating the SRS hardware. The first two steps correct the internal transceiver and generally only need to be performed once for a particular set of hardware. Subsequent steps primarily remove cable effects and must be redone when there is change in cabling. The final calibration step removes any residual range error and is repeated whenever the highest accuracy is required.

7.1.1. VCO FREQUENCY

The VCO used in the SRS has a non-linear voltage to frequency transfer function. For accurate frequency selection, the DAC codes need to be correlated to output frequency for the individual VCO in use. This is performed using a HP microwave counter (HP5343A) connected to the transmit port of the SRS using a 10 dB attenuator to avoid damage to the counter. The DAC is

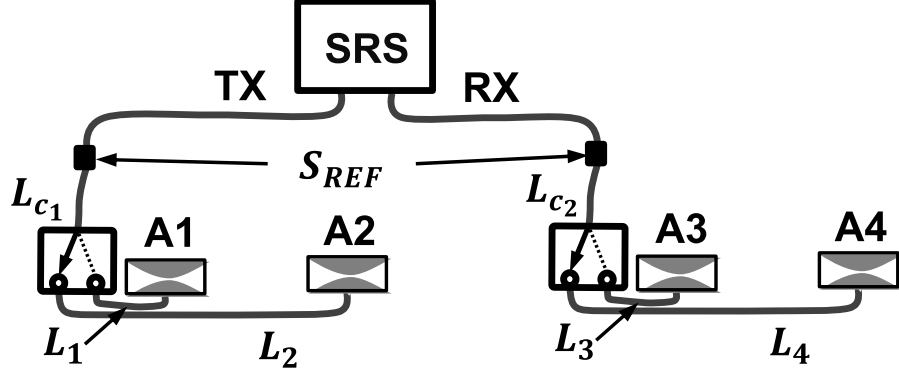


Fig. 7.1. SRS Multi-Ranger RF cable layout and calibration point S_{REF} .

stepped through a sequence of codes, dwelling long enough to measure the frequency of the counter using GPIB (general purpose instrument bus). The DAC code to VCO frequency table is stored in a file to be read when generating a new frequency sweep. To minimize calibration time, a subset of the possible DAC codes is used instead. Cubic interpolation of the stored DAC codes allows for selection of arbitrary frequencies within the sweep (limited by the DAC resolution). A 401 point full range (0-11 V) DAC code sequence was used for this work.

7.1.2. MIXER DC OFFSET

The homodyne architecture of the SRS results in dc offsets on the IQ outputs of the mixer due to imperfect isolation of the transmitter and receiver. These dc offsets can be confused with the actual signal and must be subtracted from the measurement. Once a frequency sweep is chosen, the mixer dc offsets can be measured by placing 50Ω terminations on the transmit and receive ports of the SRS. The most convenient location to place these terminators is at the end of the cables going to each shoe where S_{REF} is located (Fig. 7.1). A single SFCW sweep is made and the signal measured on the IQ channels is the dc offset

$$S_{DC}(f) = V_I(f) + jV_Q(f), \quad (7.1)$$

The resulting array of S_{DC} across frequency is stored in a file.

7.1.3. RF CABLE AND VCO POWER

The RF cables between the SRS and the shoes significantly contribute to channel delay that the SRS measures for shoe-to-shoe range. In addition, cable attenuation and VCO transmit power may change across the frequency sweep and should be calibrated out for optimal signal processing. This is done by measuring an SFCW sweep with the SRS transmit port connected to the receive port through a 30 dB attenuator between the S_{REF} points in Fig. 7.1. The attenuator ensures the LNA and mixer are operating in a linear region. Measured IQ signals versus frequency are stored in an array

$$S_{REF}(f) = V_I(f) + jV_Q(f) - S_{DC}(f). \quad (7.2)$$

Applying S_{REF} to a channel measurement S through division moves the reference plane for channel delay estimates to the end of the RF cables

$$S(f) = \frac{V_I(f) + jV_Q(f) - S_{DC}(f)}{S_{REF}(f)}. \quad (7.3)$$

7.1.4. MULTI-RANGER CABLE

For the SRS Multi-Ranger, the channel delay reference plane needs to be moved to the port of each antenna. Due to the tight routing of these cables, it is difficult to calibrate in the same manner as 7.1.3. Instead, the length of each cable is measured and the channel delay introduced is calculated. The transfer function for each RF cable in Fig. 7.1 is

$$D_k = e^{-j2\pi L_k f / (c_0 v_p)} \text{ for } k = c_1, c_2, 1, 2, 3 \text{ & } 4, \quad (7.4)$$

where v_p is the velocity propagation factor within the cable (% of c_0 , 83% for the cables used) and L_k is the RF cable length in meters. The calibrated channel response for each path is now

$$S_1(f) = \frac{V_I(f) + jV_Q(f) - S_{DC}(f)}{S_{REF}(f)D_{c_1}(f)D_{c_2}(f)D_1(f)D_3(f)}, \quad (7.5)$$

$$S_2(f) = \frac{V_I(f) + jV_Q(f) - S_{DC}(f)}{S_{REF}(f)D_{c_1}(f)D_{c_2}(f)D_1(f)D_4(f)}, \quad (7.6)$$

$$S_3(f) = \frac{V_I(f) + jV_Q(f) - S_{DC}(f)}{S_{REF}(f)D_{c_1}(f)D_{c_2}(f)D_2(f)D_3(f)}, \quad (7.7)$$

$$S_4(f) = \frac{V_I(f) + jV_Q(f) - S_{DC}(f)}{S_{REF}(f)D_{c_1}(f)D_{c_2}(f)D_2(f)D_4(f)}. \quad (7.8)$$

7.1.5. RANGE

The previous calibration steps operate on the raw IQ data. This final step for SRS calibration is implemented post range processing. Here the error between measured and true range is subtracted from the range solution. This could also be implemented along with the delay calibration similar to (7.4) where the L_k term is iteratively adjusted to remove the range error. However, it is easier to simply subtract the error from the computed range. For the motion stage data to be discussed, the mean range error relative to ground truth is subtracted from the range solution to produce the calibrated range (unless otherwise specified). This calibration should carry over to walking data if the SRS hardware and cables do not change. It is possible for day to day drift to occur (from large temperature changes or cable flexure), so an in situ calibration may be preferred. This is performed by placing each antenna pair at a known separation distance to measure the error. The position used for the range error measurement should have clear LOS (recommended range ≥ 0.3 m) and be near the max gain of the antenna – $< 30^\circ$ of boresight (direction of max gain). Calibrated range for a range error ϵ_R is

$$R'_n = R_n - \epsilon_{R_n} \quad \text{for } n = 1, 2, 3, 4. \quad (7.9)$$

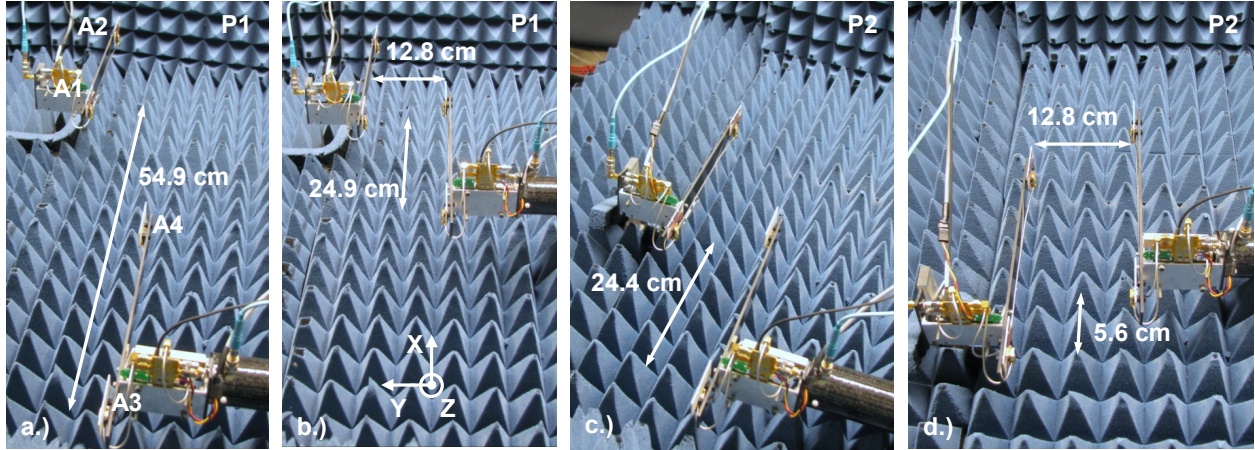


Fig. 7.2. SRS Multi-Ranger on motion stage with foam surface. The moving antennas (A3 & A4) are shown at peak positions of the cosine motion. Fixed position P1 in a, b. Fixed position P2 in c, d. Coordinate system for antenna alignment shown in b.

7.2. MOTION STAGE MEASUREMENTS

7.2.1. STAGE ALIGNMENT

The SRS Multi-Ranger performance was evaluated using a linear motion stage (Parker Motion) above three different surfaces: concrete, aluminum plate and microwave absorbing foam. The choice of surface material was selected to test the most common surface (concrete), the worst case performance with strong multipath (metal), and the best case with limited multipath (foam). Concrete used for stage measurements is ~ 9.5 cm thick. The SRS Multi-Ranger was tested on the motion stage rather than the single range system as it allows simultaneous testing of antennas in four locations.

The test setup uses a fixed shoe (left) and a moving shoe (right) mounted to the motion stage carriage. Two different fixed shoe positions are tested for foam and metal and a single position is used for concrete (Fig. 7.2). In all cases, the motion of the moving shoe is the same. The first position (P1) simulates the right shoe approaching the left with the two back antennas starting with 54.9 cm separation and moving to 24.9 cm in the direction of motion. The second position (P2) simulates the worst case performance of the Vivaldi antennas with the antennas passing through



Fig. 7.3. Laser alignment of linear motor axis.

nulls as when the shoes swing past each other (back antennas from 24.4 cm to -5.6cm). A cosine motion profile was programmed into the motor with 300 mm peak-to-peak excursion and 0.5 m/s max velocity. In both positions, the separation is about 12.8 cm which is approximately the average shoe separation distance from IMU data.

Calibration of the motion stage ground truth is required to evaluate error performance and for simulation. A laser aimed at a $25 \mu\text{m}$ pinhole was used to provide repeatable alignment. The laser was positioned to provide maximum transmission through the pinhole. Visual measurements relative to the laser beam are estimated to be within ~ 0.5 mm. The linear motor's axis was aligned to be parallel to the laser (Fig. 7.3) as were the surfaces (metal, concrete). The initial positions of the antenna centers were measured relative to the laser and are in Table 7.1. Fig. 7.4 shows the test setup for three surfaces in position P1.

Antenna	P1 (cal-1)	P1 (cal-2)	P2
A1	(-0.248, 0, 0.0685)	(-0.249, 0, 0.0705)	(-0.249, 0, 0.0705)
A2	(0, 0, 0.0685)	(0, 0, 0.0705)	(0, 0, 0.0705)
A3	(-0.795, -0.129, 0.099)	(-0.798, -0.128, 0.1015)	(-0.493, -0.127, 0.1015)
A4	(-.548, -0.129, 0.099)	(-0.548, -0.128, 0.1015)	(-0.243, -0.127, 0.1015)

Table 7.1. Initial antenna center positions in meters relative to surface and A2. Coordinate system in Fig. 7.2b, initial positions are shown in a) and c). Two alignments in position P1 were made.

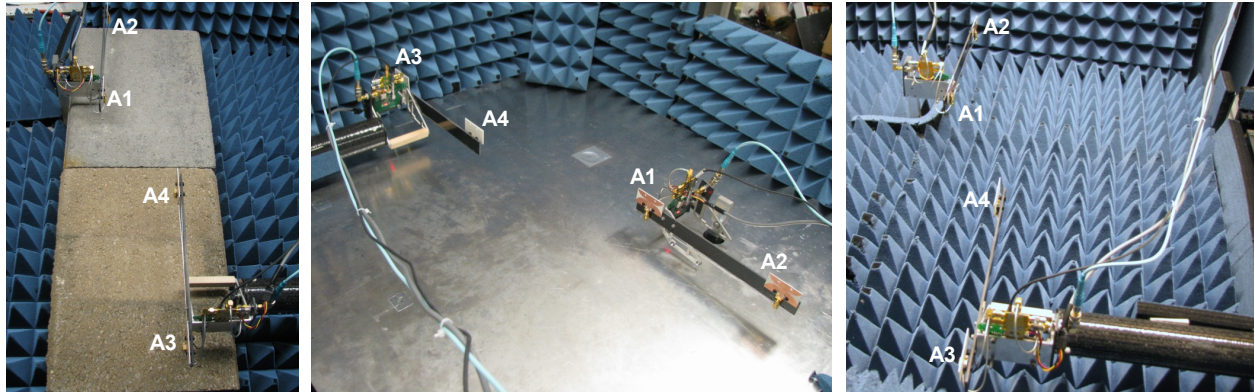


Fig. 7.4. From left to right: concrete, metal and foam surfaces.

Ground truth position is provided by a quadrature encoder on the linear motor with $5 \mu\text{m}$ resolution. The quadrature data was recorded with a Measurement Computing USB-1604HS-2AO data acquisition (DAQ) card using National Instrument's LabVIEW for control. Synchronization between the DAQ card and the SRS hardware was through a start/stop trigger pulse sent by the SRS. Due to hardware buffer sizes on the DAQ, this trigger did not result in sample level synchronization with the SRS and manual alignment was still necessary for post-processing. Additionally, for long data collection runs (1000 s and 1 hr), sample clock drift between the DAQ and the SRS is significant. A rubidium locked sample clock was used on the DAQ but there currently is no interface to externally lock the sample clock on the SRS. Post-processing with a $\sim 0.02\%$ time base correction was performed to realign the ground truth to the SRS samples.

7.2.2. RESULTS

Unless otherwise stated, a dataset is 18 s long and consists of 8 periods of the cosine motion (15.08 s) with fixed position at the beginning and end of the sequence. Simulation results use the antenna positions in Table 7.1 and 8 periods of the cosine – the fixed position at the beginning and end of the sequence is not simulated. The concrete model used is specified in Chapter 3 and the aluminum metal model uses a conductivity of $\sigma_s = 3.96 \times 10^7 \text{ S/m}$ [25]. Foam is modeled as only a LOS signal for range calculation. The antenna modeled is the Vivaldi with straight feed and the switch is

considered to have 41 dB of attenuation. SFCW settings are $N=21$ and 6.2-7.7 GHz sweep in 1.67 ms ($f_R=600$ Hz) for a single range. Four ranges are computed sequentially in 6.67 ms with an 18.3 ms delay until the next set of ranges resulting in a range update rate of 40 Hz. This reduced range update rate of 40 Hz is designed to match the navigation system's processing rate while still completing an individual range sweep fast enough that the Doppler shift is not significant. The Chirp- z has a max range limit of 2 m and calculates 512 points in that range. Prony fits for 3 exponentials and the LOS term only ($M=3, m=1$). Hybrid ranging is used in all results unless explicitly stated otherwise.

In the following tables the statistics of the range error measurements/simulations are presented for each surface, ranging and range filtering algorithm. Three levels of range filtering are used: level 0 is range limit filtering (0-2 m), level 1 uses ground truth antenna location and level 2 is antenna location with circle intersection (see 4.4). Antenna location filtering removes any range when the ground truth is <0.19 m. The mean error statistic for measured data is to be interpreted as the final calibration ϵ_R as in (7.9) which makes the standard deviation σ equivalent to the RMS error. Simulated data is already calibrated, so the mean error statistic is the error introduced by the ranging algorithm (which could also be removed with (7.9)).

7.2.2.1. TABULATED RESULTS

CONCRETE

Filter Level 0	Chirp- z Meas.		Chirp- z Sim.		Prony Meas.		Prony Sim.	
Range	μ	σ	μ	σ	μ	σ	μ	σ
R_1	-73.56	6.28	5.58	0.37	-26.27	3.72	1.58	0.37
R_2	-59.19	16.96	2.94	1.76	-16.25	19.59	2.94	1.76
R_3	-29.16	5.16	2.41	0.88	-1.01	5.02	2.4	0.88
R_4	-36.27	5.39	6.92	0.37	-1.25	4.62	6.92	0.37

Table 7.2. Concrete results in mm. Position P1 cal-1, date taken: 5/16/12

Filter Level 1	Chirp- z Meas.		Chirp- z Sim.		Prony Meas.		Prony Sim.	
Range	μ	σ	μ	σ	μ	σ	μ	σ
$R_1 (0, 0, 0, 0)$	-73.56	6.28	5.58	5.58	-26.27	3.72	1.58	0.37
$R_2 (39, 47, 39, 47)$	-71.46	3.23	4.35	4.35	-48.13	6.39	6.11	1.09
$R_3 (0, 0, 0, 0)$	-29.16	5.16	2.41	2.41	-1.01	5.02	2.4	0.88
$R_4 (0, 0, 0, 0)$	-36.27	5.39	6.92	6.92	-1.25	4.62	6.92	0.37

Table 7.3. Concrete results in mm. Position P1 cal-1, date taken: 5/16/12. Filter drop percentage for each algorithm meas/sim in () after Range.

Filter Level 2	Chirp- z Meas.		Chirp- z Sim.		Prony Meas.		Prony Sim.	
Range	μ	σ	μ	σ	μ	σ	μ	σ
$R_1 (0, 0, 0, 0)$	-73.56	6.28	5.58	0.37	-26.27	3.72	1.58	0.37
$R_2 (50, 47, 39, 47)$	-71.46	3.23	4.35	0.87	-48.13	6.39	6.11	1.09
$R_3 (0, 0, 0, 0)$	-29.16	5.16	2.41	0.88	-1.01	5.02	2.4	0.88
$R_4 (32, 47, 25, 47)$	-36.27	5.39	7.14	0.29	-1.15	4.52	7.14	0.29

Table 7.4. Concrete results in mm. Position P1 cal-1, date taken: 5/16/12. Filter drop percentage for each algorithm meas/sim in () after Range.

Filter Level 0	Chirp- z Meas.		Chirp- z Sim.		Prony Meas.		Prony Sim.	
Range	μ	σ	μ	σ	μ	σ	μ	σ
R_1	-69.51	3.81	3.95	0.4	-33.91	2.4	3.95	0.4
R_2	-55.66	19.93	13.34	13.54	-7.46	19.16	16.69	11.34
R_3	-23.69	3.83	7.35	0.6	-8.03	5.33	7.35	0.6
R_4	-32.58	3.63	7.27	0.39	-2.67	2.94	7.27	0.39

Table 7.5. Concrete results in mm. Position P1 cal-2, date taken: 6/20/12

Filter Level 1	Chirp- z Meas.		Chirp- z Sim.		Prony Meas.		Prony Sim.	
Range	μ	σ	μ	σ	μ	σ	μ	σ
$R_1 (0, 0, 0, 0)$	-69.51	3.81	3.95	0.4	-33.91	2.4	3.95	0.4
$R_2 (39, 47, 39, 47)$	-67.3	8.15	-4.35	3.84	-39	6.59	-1.96	2.98
$R_3 (0, 0, 0, 0)$	-23.69	3.83	7.35	0.6	-8.03	5.33	7.35	0.6
$R_4 (0, 0, 0, 0)$	-32.58	3.63	7.27	0.39	-2.67	2.94	7.27	0.39

Table 7.6. Concrete results in mm. Position P1 cal-2, date taken: 6/20/12. Filter drop percentage for each algorithm meas/sim in () after Range.

Filter Level 2	Chirp- z Meas.		Chirp- z Sim.		Prony Meas.		Prony Sim.	
Range	μ	σ	μ	σ	μ	σ	μ	σ
$R_1 (0, 0, 8, 0)$	-69.51	3.81	3.95	0.4	-33.58	2.1	3.95	0.4
$R_2 (39, 47, 39, 47)$	-67.3	8.15	-4.35	3.84	-39	6.59	-1.96	2.98
$R_3 (0, 0, 8, 0)$	-23.69	3.83	7.35	0.6	-9.29	3.52	7.35	0.6
$R_4 (19, 47, 30, 47)$	-32.72	3.73	7.35	0.32	-31.6	2.72	7.35	0.32

Table 7.7. Concrete results in mm. Position P1 cal-2, date taken: 6/20/12. Filter drop percentage for each algorithm meas/sim in () after Range.

Filter Level 0	Chirp- z Meas.		Chirp- z Sim.		Prony Meas.		Prony Sim.	
Range	μ	σ	μ	σ	μ	σ	μ	σ
R_1	-71.67	2.43	3.95	0.4	-29.62	2.46	3.95	0.4
R_2	-45.02	20.08	13.34	13.54	-2.57	19.82	16.69	11.34
R_3	-23.51	4.19	7.35	0.6	-4.04	3.9	7.35	0.6
R_4	-32.94	2.68	7.27	0.39	0.82	3.33	7.27	0.39

Table 7.8. Concrete results in mm for 1 hr cosine. Position P1 cal-2, date taken: 6/20/12

Filter Level 1	Chirp- z Meas.		Chirp- z Sim.		Prony Meas.		Prony Sim.	
Range	μ	σ	μ	σ	μ	σ	μ	σ
$R_1 (0, 0, 0, 0)$	-71.67	2.43	3.95	0.4	-29.62	2.46	3.95	0.4
$R_2 (46, 47, 46, 47)$	-56.15	8.74	-4.35	3.84	-28.85	4.09	-1.96	2.98
$R_3 (0, 0, 0, 0)$	-23.51	4.19	7.35	0.6	-4.04	3.9	7.35	0.6
$R_4 (0, 0, 0, 0)$	-32.94	2.68	7.27	0.39	0.82	3.33	7.27	0.39

Table 7.9. Concrete results in mm for 1 hr cosine. Position P1 cal-2, date taken: 6/20/12. Filter drop percentage for each algorithm meas/sim in () after Range.

Filter Level 2	Chirp- z Meas.		Chirp- z Sim.		Prony Meas.		Prony Sim.	
Range	μ	σ	μ	σ	μ	σ	μ	σ
$R_1 (0, 0, 0, 0)$	-71.67	2.43	3.95	0.4	-29.6	2.41	3.95	0.4
$R_2 (51, 47, 46, 47)$	-54.66	7.57	-4.35	3.84	-28.84	4.08	-1.96	2.98
$R_3 (0, 0, 0, 0)$	-23.51	4.2	7.35	0.6	-4.05	3.9	7.35	0.6
$R_4 (32, 47, 46, 47)$	-33.32	2.53	7.35	0.32	-0.17	3.51	7.35	0.32

Table 7.10. Concrete results in mm for 1 hr cosine. Position P1 cal-2, date taken: 6/20/12. Filter drop percentage for each algorithm meas/sim in () after Range.

MICROWAVE ABSORBING FOAM

Filter Level 0	Chirp- z Meas.		Chirp- z Sim.		Prony Meas.		Prony Sim.	
Range	μ	σ	μ	σ	μ	σ	μ	σ
R_1	-85.52	4.15	1.54	0.72	-14.68	5.91	1.54	0.72
R_2	-75.09	15.38	6.56	1.89	-13.41	25.06	4.56	1.67
R_3	-51.33	3.82	1.23	0.28	-17.95	2.94	1.23	0.28
R_4	-44.06	2.09	2.89	0.72	-31.14	1.8	2.91	0.7

Table 7.11. Foam results in mm. Position P1 cal-1, date taken: 5/17/12

Filter Level 1	Chirp- z Meas.		Chirp- z Sim.		Prony Meas.		Prony Sim.	
Range	μ	σ	μ	σ	μ	σ	μ	σ
$R_1 (0, 0, 0, 0)$	-85.52	4.15	1.54	0.72	-14.68	5.91	1.54	0.72
$R_2 (38, 47, 38, 47)$	-81.94	6.91	4.31	0.77	-51.95	4.62	2.57	0.38
$R_3 (0, 0, 0, 0)$	-51.33	3.82	1.23	0.28	-17.95	2.94	1.23	0.28
$R_4 (0, 0, 0, 0)$	-44.06	2.09	2.89	0.72	-31.14	1.8	2.91	0.7

Table 7.12. Foam results in mm. Position P1 cal-1, date taken: 5/17/12. Filter drop percentage for each algorithm meas/sim in () after Range.

Filter Level 2	Chirp- z Meas.		Chirp- z Sim.		Prony Meas.		Prony Sim.	
Range	μ	σ	μ	σ	μ	σ	μ	σ
R_1 (0, 0, 8, 0)	-85.52	4.15	1.54	0.72	-13.24	3.89	1.54	0.72
R_2 (39, 47, 38, 47)	-81.56	6.08	4.31	0.77	-51.95	4.62	2.57	0.38
R_3 (0, 0, 8, 0)	-51.33	3.82	1.23	0.28	-18.24	2.86	1.23	0.28
R_4 (1, 47, 24, 47)	-44.08	2.09	2.87	0.67	-31.3	1.6	2.87	0.67

Table 7.13. Foam results in mm. Position P1 cal-1, date taken: 5/17/12. Filter drop percentage for each algorithm meas/sim in () after Range.

Filter Level 0	Chirp- z Meas.		Chirp- z Sim.		Prony Meas.		Prony Sim.	
Range	μ	σ	μ	σ	μ	σ	μ	σ
R_1	-81.68	5.55	3.93	0.28	-29.49	3.91	2	0.28
R_2	-71.78	18.86	25.69	13.12	-14.2	23.33	9.01	3.4
R_3	-43.53	5	0.9	0.65	-15.6	6.71	-0.85	0.28
R_4	-36.94	2.48	3.05	0.72	-20.58	1.83	3.07	0.7

Table 7.14. Foam results in mm. Position P1 cal-2, date taken: 6/12/12

Filter Level 1	Chirp- z Meas.		Chirp- z Sim.		Prony Meas.		Prony Sim.	
Range	μ	σ	μ	σ	μ	σ	μ	σ
R_1 (0, 0, 0, 0)	-81.68	5.55	3.93	0.28	-29.49	3.91	2	0.28
R_2 (39, 47, 39, 47)	-80.47	8.38	4.63	0.35	-43.87	4.13	2.89	0.33
R_3 (0, 0, 0, 0)	-43.53	5	0.9	0.65	-15.6	6.71	-0.85	0.28
R_4 (0, 0, 0, 0)	-36.94	2.19	3.05	0.72	-20.58	1.83	3.07	0.7

Table 7.15. Foam results in mm. Position P1 cal-2, date taken: 6/12/12. Filter drop percentage for each algorithm meas/sim in () after Range.

Filter Level 2	Chirp- z Meas.		Chirp- z Sim.		Prony Meas.		Prony Sim.	
Range	μ	σ	μ	σ	μ	σ	μ	σ
R_1 (0, 0, 15, 0)	-81.68	5.55	3.93	0.28	-28.54	3.47	2	0.28
R_2 (40, 47, 39, 47)	-79.92	7.32	4.63	0.35	-43.87	4.13	2.89	0.33
R_3 (0, 0, 15, 0)	-43.53	5	0.9	0.65	-17.99	4.14	-0.85	0.28
R_4 (1, 47, 27, 47)	-36.94	2.2	3.01	0.67	-20.86	1.72	3.01	0.67

Table 7.16. Foam results in mm. Position P1 cal-2, date taken: 6/12/12. Filter drop percentage for each algorithm meas/sim in () after Range.

Filter Level 0	Chirp- z Meas.		Chirp- z Sim.		Prony Meas.		Prony Sim.	
Range	μ	σ	μ	σ	μ	σ	μ	σ
R_1	-57.22	17.41	26.92	11.86	-37.2	15.09	8.04	2.25
R_2	-4.6	47.2	8.5	1.93	7.83	22.25	8.46	2
R_3	-12.16	58.04	-1.11	0.29	18.21	30.97	-1.11	0.29
R_4	-39.87	28.37	27.39	12.64	5.88	18.54	5.07	2.54

Table 7.17. Foam results in mm. Position P2, date taken: 6/12/12

Filter Level 1	Chirp- z Meas.		Chirp- z Sim.		Prony Meas.		Prony Sim.	
Range	μ	σ	μ	σ	μ	σ	μ	σ
R_1 (48, 59, 48, 59)	-82.94	3.36	4.64	1.22	-56.02	3.58	3.02	0.36
R_2 (49, 46, 49, 46)	-7.12	67.62	4.69	0.26	14.55	27.6	2.84	0.26
R_3 (0, 0, 0, 0)	-12.16	58.04	-1.11	0.29	18.21	30.97	-1.11	0.29
R_4 (49, 60, 49, 60)	-50.4	2.82	-0.07	0.46	-19.76	8.29	-1.81	0.35

Table 7.18. Foam results in mm. Position P2, date taken: 6/12/12. Filter drop percentage for each algorithm meas/sim in () after Range.

Filter Level 2	Chirp- z Meas.		Chirp- z Sim.		Prony Meas.		Prony Sim.	
Range	μ	σ	μ	σ	μ	σ	μ	σ
R_1 (48, 59, 48, 59)	-82.94	3.36	4.64	1.22	-56.02	3.58	3.02	0.36
R_2 (64, 100, 88, 99)	-43.94	51.46	4.58	0.28	22.31	9.77	2.9	0.32
R_3 (21, 59, 28, 59)	-27.21	45.01	-1.24	0.24	11.46	32	-1.24	0.24
R_4 (88,100, 92,100)	-49.83	2.39	-	-	-	-	-	-

Table 7.19. Foam results in mm. Position P2, date taken: 6/12/12. Filter drop percentage for each algorithm meas/sim in () after Range. “-” indicates too many measurements were dropped.

Filter Level 0	Chirp- z Meas.		Chirp- z Sim.		Prony Meas.		Prony Sim.	
Range	μ	σ	μ	σ	μ	σ	μ	σ
R_1	-85.44	2.91	3.93	0.28	-26.23	3.02	2	0.28
R_2	-63.03	23.02	25.69	13.12	-5.96	23.19	9.01	3.4
R_3	-34.49	5.02	0.9	0.65	-14.73	2.42	-0.85	0.28
R_4	-39.29	3.24	3.05	0.72	-10.94	5.14	3.07	0.7

Table 7.20. Foam results in mm for 1 hr cosine. Position P1 cal-2, date taken: 6/20/12

Filter Level 1	Chirp- z Meas.		Chirp- z Sim.		Prony Meas.		Prony Sim.	
Range	μ	σ	μ	σ	μ	σ	μ	σ
R_1 (0, 0, 0, 0)	-85.44	2.91	3.93	0.28	-26.23	3.02	2	0.28
R_2 (46, 47, 46, 47)	-66.07	8.4	4.63	0.35	-30.15	3.74	2.89	0.33
R_3 (0, 0, 0, 0)	-34.49	5.02	0.9	0.65	-14.73	2.42	-0.85	0.28
R_4 (0, 0, 0, 0)	-39.29	3.24	3.05	0.72	-10.94	5.14	3.07	0.7

Table 7.21. Foam results in mm for 1 hr cosine. Position P1 cal-2, date taken: 6/20/12. Filter drop percentage for each algorithm meas/sim in () after Range.

Filter Level 2	Chirp- z Meas.		Chirp- z Sim.		Prony Meas.		Prony Sim.	
Range	μ	σ	μ	σ	μ	σ	μ	σ
R_1 (1, 0, 6, 0)	-85.42	2.9	3.93	0.28	-25.92	2.73	2	0.28
R_2 (49, 47, 46, 47)	-65.5	8.2	4.63	0.35	-30.15	3.74	2.89	0.33
R_3 (1, 0, 6, 0)	-34.53	5.02	0.9	0.65	-14.83	2.42	-0.85	0.28
R_4 (26, 47, 45, 47)	-39.68	3.06	3.01	0.67	-12.39	5.24	3.01	0.67

Table 7.22. Foam results in mm for 1 hr cosine. Position P1 cal-2, date taken: 6/20/12. Filter drop percentage for each algorithm meas/sim in () after Range.

Filter Level 0	Chirp- z Meas.		Chirp- z Sim.		Prony Meas.		Prony Sim.	
Range	μ	σ	μ	σ	μ	σ	μ	σ
R_1	-85.64	4.93	3.93	0.28	-32.7	4.03	2	0.28
R_2	-74.56	19.37	25.69	13.12	-12.31	22.5	9.01	3.4
R_3	-49.18	5.39	0.9	0.65	-18.12	3.43	-0.85	0.28
R_4	-38.73	2.99	3.05	0.72	-29.24	3.41	3.07	0.7

Table 7.23. Foam results in mm. Position P1 cal-2, date taken: 6/20/12

Filter Level 1	Chirp- z Meas.		Chirp- z Sim.		Prony Meas.		Prony Sim.	
Range	μ	σ	μ	σ	μ	σ	μ	σ
$R_1 (0, 0, 0, 0)$	-85.64	4.93	3.93	0.28	-32.7	4.03	2	0.28
$R_2 (39, 47, 39, 47)$	-76.96	7.18	4.63	0.35	-38.4	5.16	2.89	0.33
$R_3 (0, 0, 0, 0)$	-49.18	5.39	0.9	0.65	-18.12	3.43	-0.85	0.28
$R_4 (0, 0, 0, 0)$	-38.73	2.99	3.05	0.72	-29.24	3.41	3.07	0.7

Table 7.24. Foam results in mm. Position P1 cal-2, date taken: 6/20/12. Filter drop percentage for each algorithm meas/sim in () after Range.

Filter Level 2	Chirp- z Meas.		Chirp- z Sim.		Prony Meas.		Prony Sim.	
Range	μ	σ	μ	σ	μ	σ	μ	σ
$R_1 (1, 0, 10, 0)$	-85.67	4.95	3.93	0.28	-31.66	2.73	2	0.28
$R_2 (39, 47, 39, 47)$	-76.96	7.18	4.63	0.35	-38.4	5.16	2.89	0.33
$R_3 (1, 0, 10, 0)$	-49.36	5.16	0.9	0.65	-18.98	2.42	-0.85	0.28
$R_4 (17, 47, 30, 47)$	-38.88	2.89	3.01	0.67	-29.37	3.43	3.01	0.67

Table 7.25. Foam results in mm. Position P1 cal-2, date taken: 6/20/12. Filter drop percentage for each algorithm meas/sim in () after Range.

ALUMINUM PLATE

Filter Level 0	Chirp- z Meas.		Chirp- z Sim.		Prony Meas.		Prony Sim.	
Range	μ	σ	μ	σ	μ	σ	μ	σ
R_1	-81.57	10.7	-3.19	3.81	-37.3	8.84	3.28	3.64
R_2	-28.73	27.32	-1.75	21.35	-5.95	39.71	9.42	14.32
R_3	-25.03	3.19	26.98	48.89	-3.28	3.58	25.15	7.78
R_4	-32.87	10.16	0.4	3.76	5.16	5.51	6.62	3.6

Table 7.26. Metal results in mm. Position P1 cal-2, date taken: 6/5/12

Filter Level 1	Chirp- z Meas.		Chirp- z Sim.		Prony Meas.		Prony Sim.	
Range	μ	σ	μ	σ	μ	σ	μ	σ
$R_1 (0, 0, 0, 0)$	-81.57	10.7	-3.19	3.81	-37.3	8.84	3.28	3.64
$R_2 (39, 47, 39, 47)$	-48.09	10.51	-4.46	10.16	-44.47	9.64	-1.4	6.02
$R_3 (0, 0, 0, 0)$	-25.03	3.19	26.98	48.89	-3.28	3.58	25.32	7.9
$R_4 (0, 0, 0, 0)$	-32.87	10.16	0.4	3.76	5.16	5.51	6.62	3.6

Table 7.27. Metal results in mm. Position P1 cal-2, date taken: 6/5/12. Filter drop percentage for each algorithm meas/sim in () after Range.

Filter Level 2	Chirp- z Meas.		Chirp- z Sim.		Prony Meas.		Prony Sim.	
Range	μ	σ	μ	σ	μ	σ	μ	σ
R_1 (15, 61, 6, 54)	-79.62	10.56	0.58	2.41	-36.63	8.65	6.44	2.74
R_2 (47, 49, 46, 47)	-43.92	3.79	-3.21	8.18	-41.19	5.15	-1.4	6.02
R_3 (15, 61, 6, 54)	-24.44	3.08	-28.11	13.37	-3.12	3.59	18.02	4.95
R_4 (9, 49, 36, 47)	-35.62	5.76	-2.87	1.52	3.01	3.93	3.56	1.4

Table 7.28. Metal results in mm. Position P1 cal-2, date taken: 6/5/12. Filter drop percentage for each algorithm meas/sim in () after Range.

Filter Level 0	Chirp- z Meas.		Chirp- z Sim.		Prony Meas.		Prony Sim.	
Range	μ	σ	μ	σ	μ	σ	μ	σ
R_1	-85.19	11.13	-3.19	3.81	-32.93	13.79	3.28	3.64
R_2	-38.57	25.44	-1.75	21.35	-11.47	42.14	9.42	14.32
R_3	-28.85	2.58	26.98	48.89	-10.13	4.18	25.15	7.78
R_4	-37.18	12.41	0.4	3.76	0.54	6.54	6.62	3.6

Table 7.29. Metal results in mm. Position P1 cal-2, date taken: 6/6/12

Filter Level 1	Chirp- z Meas.		Chirp- z Sim.		Prony Meas.		Prony Sim.	
Range	μ	σ	μ	σ	μ	σ	μ	σ
R_1 (0, 0, 0, 0)	-85.19	11.13	-3.19	3.81	-32.93	13.79	3.28	3.64
R_2 (39, 47, 39, 47)	-56.93	11.75	-4.46	10.16	-49.09	10.77	-1.4	6.02
R_3 (0, 0, 0, 0)	-28.85	2.58	26.98	48.89	-10.13	4.18	25.32	7.9
R_4 (0, 0, 0, 0)	-37.18	12.41	0.4	3.76	0.54	6.54	6.62	3.6

Table 7.30. Metal results in mm. Position P1 cal-2, date taken: 6/6/12. Filter drop percentage for each algorithm meas/sim in () after Range.

Filter Level 2	Chirp- z Meas.		Chirp- z Sim.		Prony Meas.		Prony Sim.	
Range	μ	σ	μ	σ	μ	σ	μ	σ
R_1 (22, 61, 20, 54)	-82.42	11.36	0.58	2.41	-29.75	14	6.44	2.74
R_2 (50, 49, 50, 47)	-51.55	6.01	-3.21	8.18	-43.89	3.52	-1.4	6.02
R_3 (22, 61, 20, 54)	-28.02	2.29	-28.11	13.37	-9.6	4.46	18.02	4.95
R_4 (12, 49, 37, 47)	-40.99	7.67	-2.87	1.52	-2.53	6.39	3.56	1.4

Table 7.31. Metal results in mm. Position P1 cal-2, date taken: 6/6/12. Filter drop percentage for each algorithm meas/sim in () after Range.

Filter Level 0	Chirp- z Meas.		Chirp- z Sim.		Prony Meas.		Prony Sim.	
Range	μ	σ	μ	σ	μ	σ	μ	σ
R_1	-20.06	71.46	4.69	23.29	4.87	35.74	13.72	16.18
R_2	-14.24	66.34	-11.98	11.61	14.66	27.06	-3.44	4.67
R_3	8.09	66.66	7.14	3.98	44.1	41.86	9.13	4.03
R_4	21.29	83.51	4.82	22.98	48.36	39.71	13.38	14.52

Table 7.32. Metal results in mm. Position P2, date taken: 6/11/12

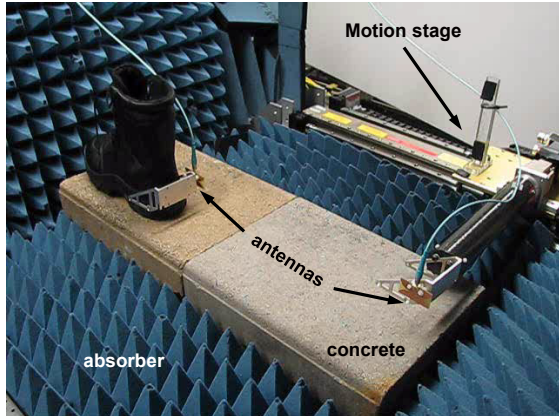


Fig. 7.5. Inline Vivaldi antennas experimental setup with SRS single ranger (left). Measured error versus position using level 0 range filtering and Chirp- z .

Filter Level 1 Range	Chirp- z Meas.		Chirp- z Sim.		Prony Meas.		Prony Sim.	
	μ	σ	μ	σ	μ	σ	μ	σ
R_1 (49, 59, 49, 59)	-50.75	75.73	-6.85	11.14	-14.72	29.6	-2.74	6.91
R_2 (51, 46, 51, 46)	-37.31	79.6	-3.87	8.73	1.18	23.15	-1.2	4.17
R_3 (0, 0, 0, 0)	8.09	66.66	7.14	3.98	44.1	41.86	9.13	4.03
R_4 (49, 60, 49, 60)	-14.06	78.95	-5.19	12.81	16.25	12.09	-2.3	8.03

Table 7.33. Metal results in mm. Position P2, date taken: 6/11/12. Filter drop percentage for each algorithm meas/sim in () after Range.

Filter Level 2 Range	Chirp- z Meas.		Chirp- z Sim.		Prony Meas.		Prony Sim.	
	μ	σ	μ	σ	μ	σ	μ	σ
R_1 (60, 60, 49, 59)	-29.05	73.94	-6.2	10.32	-14.72	29.6	-2.74	6.91
R_2 (84, 98, 95, 99)	-55.68	45.74	-1.87	4.65	-	-	0.25	1.84
R_3 (50, 51, 42, 56)	-28.51	5.58	4.75	3.87	15.82	5.79	5.67	2.81
R_4 (76, 97, 95, 99)	-35.34	42.29	-1.31	6.47	-	-	-1.53	5.51

Table 7.34. Metal results in mm. Position P2, date taken: 6/11/12. Filter drop percentage for each algorithm meas/sim in () after Range. “-” indicates too many measurements were dropped.

7.2.2.2. OPTIMAL ANTENNA ALIGNMENT

The data presented in this chapter has thus far focused on motion approximating a walking motion with \sim 10 cm of lateral separation of the antennas. For the Vivaldi antennas, the optimal motion has 0 cm lateral separation so that the LOS signal path is always on boresight with minimal change in antenna gain throughout the motion. This inline motion configuration can give insight to the best possible ranging performance of the Vivaldi antennas as well as to what degree does more realistic motion profiles degrade performance. An experiment with the Vivaldi antennas aligned for inline motion was performed with an older version of the SRS single ranger. This SRS used the

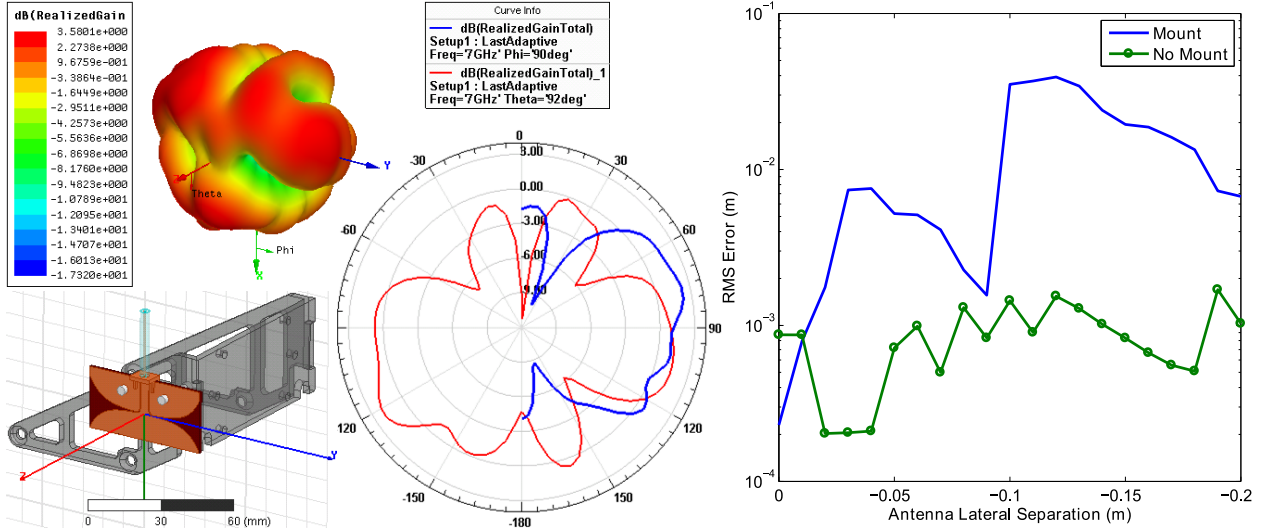


Fig. 7.6. Vivaldi antenna with straight coax feed and aluminum mount 2D and 3D gain patterns (left). Effect of left shoe lateral separation on RMS range error and antenna model choice in SRS Simulator (right).

DAQ card with lower performance 16 bit ADCs to record the IQ channels instead of the dedicated FPGA.

Fig. 7.5 shows the experimental setup and an error versus position plot of the SRS. The SFCW sweep was configured for a sweep of $N=201$ between 6.5-7.5 GHz and $f_R=200$ Hz. The motion profile was a quasi-square wave of 2 cycles with peak excursion of 350 mm and a velocity limit of 0.5 m/s. Only the Chirp- z algorithm with hybrid ranging was used on this data. Laser alignment was not used so range calibration is based on the initial position. RMS error is 0.59 mm with a mean error after calibration of -0.42 mm.

SIMULATION OF LATERAL SEPARATION

The SRS Simulator using the motion stage ground truth data (350 mm quasi-square wave) and a sweep of shoe lateral separation from 0-20 cm was used to analyze the effect of antenna alignment. Initially, the straight coax fed Vivaldi antenna was selected for the antenna dataset but it did not show the increase in error with lateral separation that was found in measurements. A new HFSS Vivaldi model including the aluminum mount frame (no carbon fiber was used on this mount) was

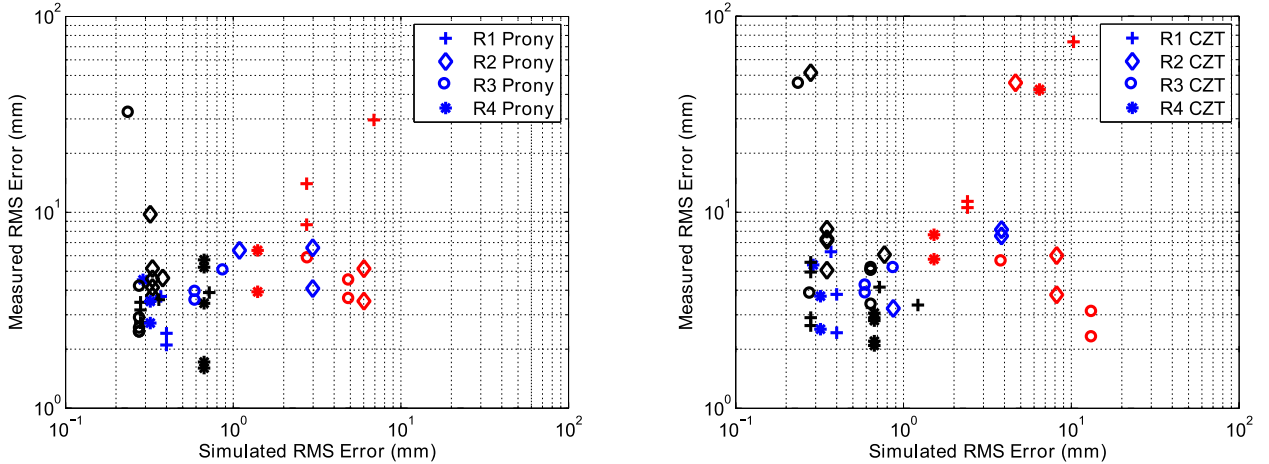


Fig. 7.7. Measured versus simulated RMS error using level 2 range filtering. Left Prony method, right Chirp- z . Blue is concrete, black is foam and red is metal.

simulated (gain patterns in Fig. 7.6). This time the simulation showed similar behavior as found in measurements with RMS error increasing with lateral separation (Fig. 7.6). Additionally, this illustrates the need to model the antenna mount to increase correlation between measured and simulated results.

7.2.3. ANALYSIS

In Fig. 7.7, level 2 filtered RMS error (i.e. standard deviation σ) of measured and simulated across all surfaces are shown for both Prony and Chirp- z . The bulk of the measurements for both algorithms are sub-cm RMS error. Overall, the Prony method performs slightly better with an average RMS error of 5.54 mm across all level 2 measurements while the Chirp- z achieves 9.71 mm. The Chirp- z has significantly higher error in position P2 leading to the higher average RMS error. If the position P2 data is dropped, then the average RMS error drops to 4.21 mm for Prony and 4.91 mm for Chirp- z . Clearly, filtering to reject when the shoe is in the position P2 region is necessary to maintain high overall accuracy throughout the step. Average RMS error with level 0 filtering is 12.78 mm for Prony and 16.47 mm for Chirp- z .

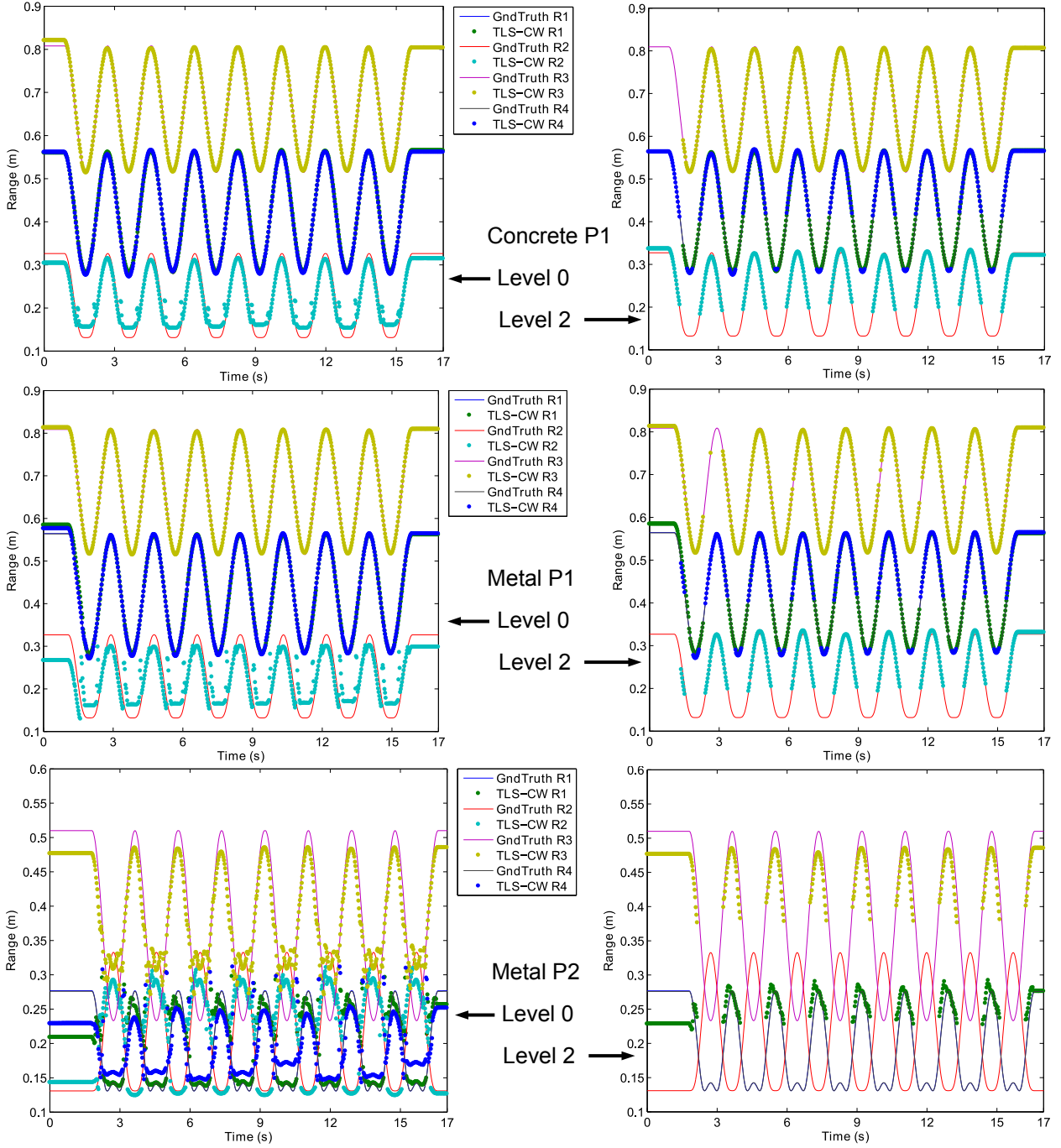


Fig. 7.8. Prony computed range plots comparing level 0 (left) and level 2 (right) filtering. Cropped to 17 s due to ground truth alignment. R1 and R4 ground truth are approximately equal.

Simulated results are typically 2-10 times better accuracy than measured. With level 0 range filtering, the SRS simulator does predict poor accuracy on R2 on the metal and concrete surfaces (cal-2). In cal-1 on concrete, the simulation predicts higher error on R2. This suggests that the slight alignment change between cal-1 and cal-2 coupled with the modeled antenna pattern is causing the

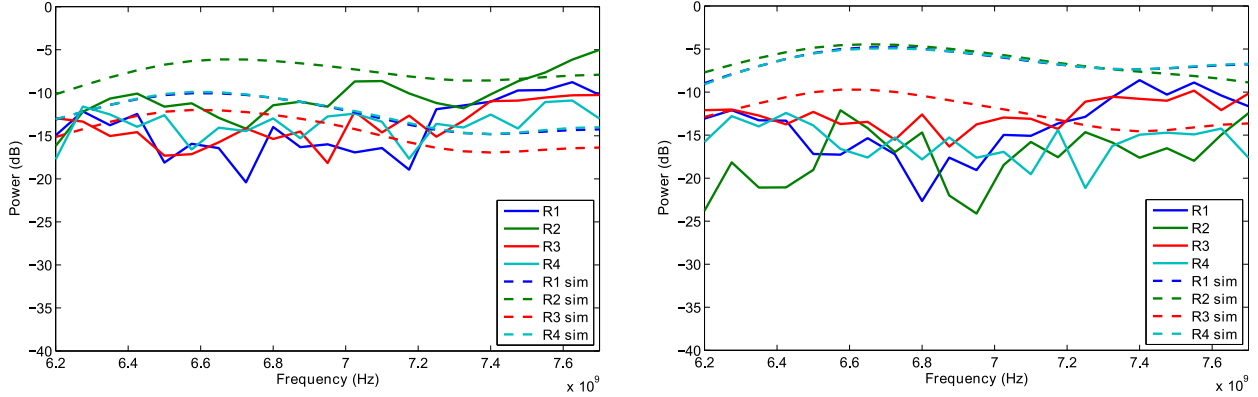


Fig. 7.9. Simulated and measured channel spectral response for concrete position P1 (6/20/12). Left corresponds to max range (2.75 s), right is min range (3.65 s).

reduced simulation agreement (i.e. null location and strength). The antenna model used does not consider the carbon fiber mount or metal frame. More accurate simulation results may be possible with increased complexity on the HFSS model.

Range plots along with ground truth are shown in Fig. 7.8 for the Prony method under level 0 and level 2 range filtering (Chirp- Z results are fairly similar). Range calibration is performed by subtracting the mean error (ϵ_R) from the range output. The position P1 plots show poor accuracy in R3 while the antennas pass each other (bottom half of cosine). Filtering ranges below 0.19 m removes this trouble region and allows the calibration to have good accuracy otherwise. Also, for certain ranges there is a fixed error ~ 1 cm between 0-1 s. This is likely due to incorrect wavelength ambiguity estimation on one or more of the CW measurements – the error appears to be quickly corrected by filtering.

For position P2, R3 has the best performance because the antennas never pass – though the range accuracy becomes poor when the antenna is within 0.3 m. The other ranges appear to have a compressed dynamic range. The strong NLOS component off the metal will of course travel a longer distance. If the Prony solution is unable to fully separate LOS and NLOS, it may become biased by the strong NLOS component, compressing the dynamic range. Assuming the Prony

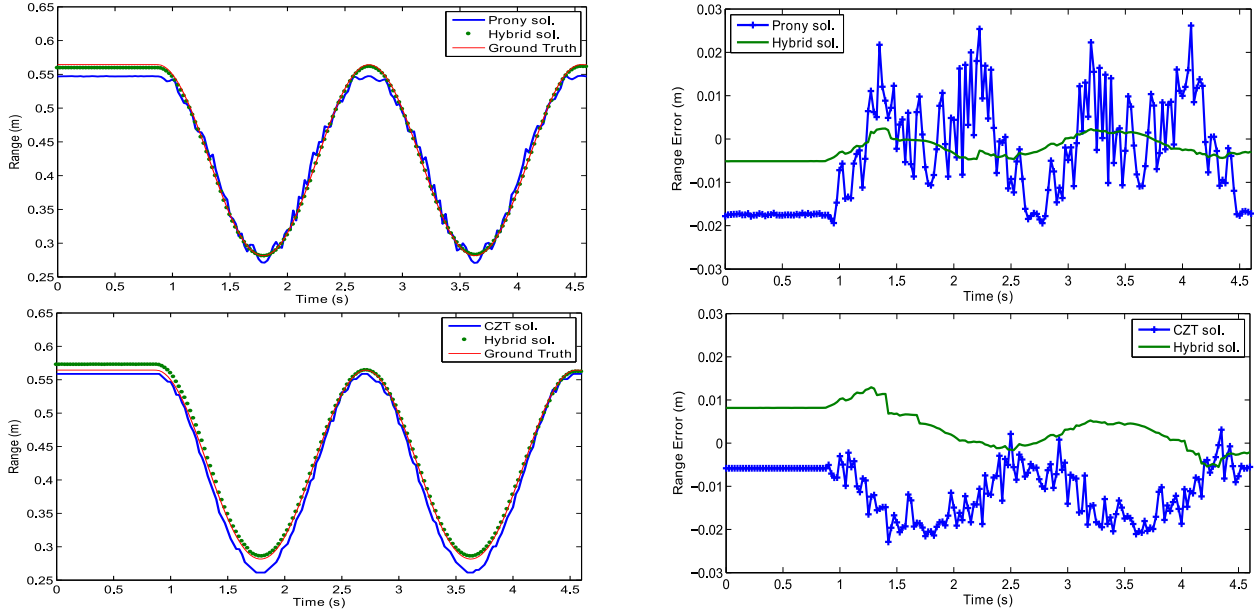


Fig. 7.10. Comparison of Prony and Chirp- z (CZT) only solution with CW phase Hybrid ranging. Range plots on left, range error on right. Dataset is concrete at position P1 (6/20/12).

method is sufficiently rejecting the NLOS component, then the compressed dynamic range may be due to sudden changes in phase from the transition between elements of the Vivaldi array. Level 2 filtering appears to be a bit overaggressive here, completely rejecting R2 and R4. Also, the use of average error for calibration seems to be a poor choice for R3 – much better agreement would be possible if the initial or final position is used for calibration.

7.2.3.1. CHANNEL POWER

In Fig. 7.9, the measured and simulated channel response is shown at the maximum and minimum of the cosine motion profile. The measured channel response is relative to S_{REF} (30 dB attenuator). Considering cable losses and VCO power, the transmitted power at the terminal of the antennas is ~ 0 dBm. The simulated channel response also transmits at 0 dBm and can be compared to the measured response by adding 30 dB to account for the attenuator (as plotted). At the maximum range position, the simulated and measured channel response for each range agrees fairly well. The measured data shows more fading likely due to additional multipath from the laboratory not modeled in the simulation.

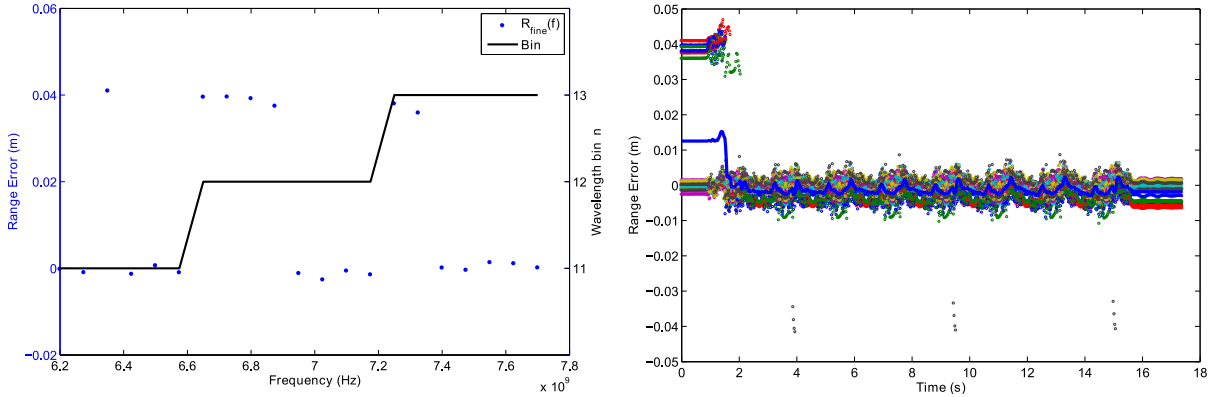


Fig. 7.11. Range error and wavelength bin selection across frequency at 0 s (left). Range error across motion for all N measurements in dots – solid line is the final range solution from averaging all measurements (right). Average error is removed for all range error plots. Dataset is concrete at position P1 (6/20/12) and range R1 computed using Chirp- z .

At minimum range, only R3 agrees well between measured and simulation with the other ranges approximately 10 dB off. R3 is the largest range which means the LOS path is closer to boresight of the antenna than the other ranges. Thus it appears that the simulated antenna pattern off-boresight is different than a real mounted antenna.

7.2.3.2. HYBRID RANGING

It was postulated in Chapter 2, based on experimental results in [22], that combining CW phase with SFCW range processing would result in lower range error. In Fig. 7.10, plots of the Prony and Chirp- z solution with and without CW phase processing are shown. Adding hybrid ranging significantly lowers the range variance, providing a much smoother range estimate. Fig. 7.12 shows a side-effect of using hybrid ranging – multiple peaks in the error distribution. Both coarse range (Prony or Chirp- z) and fine range (hybrid) error distributions for R1 are shown for the concrete 1 hr dataset (6/20/12). Depending on the implementation of the navigation algorithm, the presence of multiple peaks in the error distribution may cause a shifting mean error if modeled as a single Gaussian. Generally, the solution is to slightly increase the modeled variance for the range in the navigation algorithm. The fine range distribution peaks are clustered within a few mm, so the impact should be minimal.

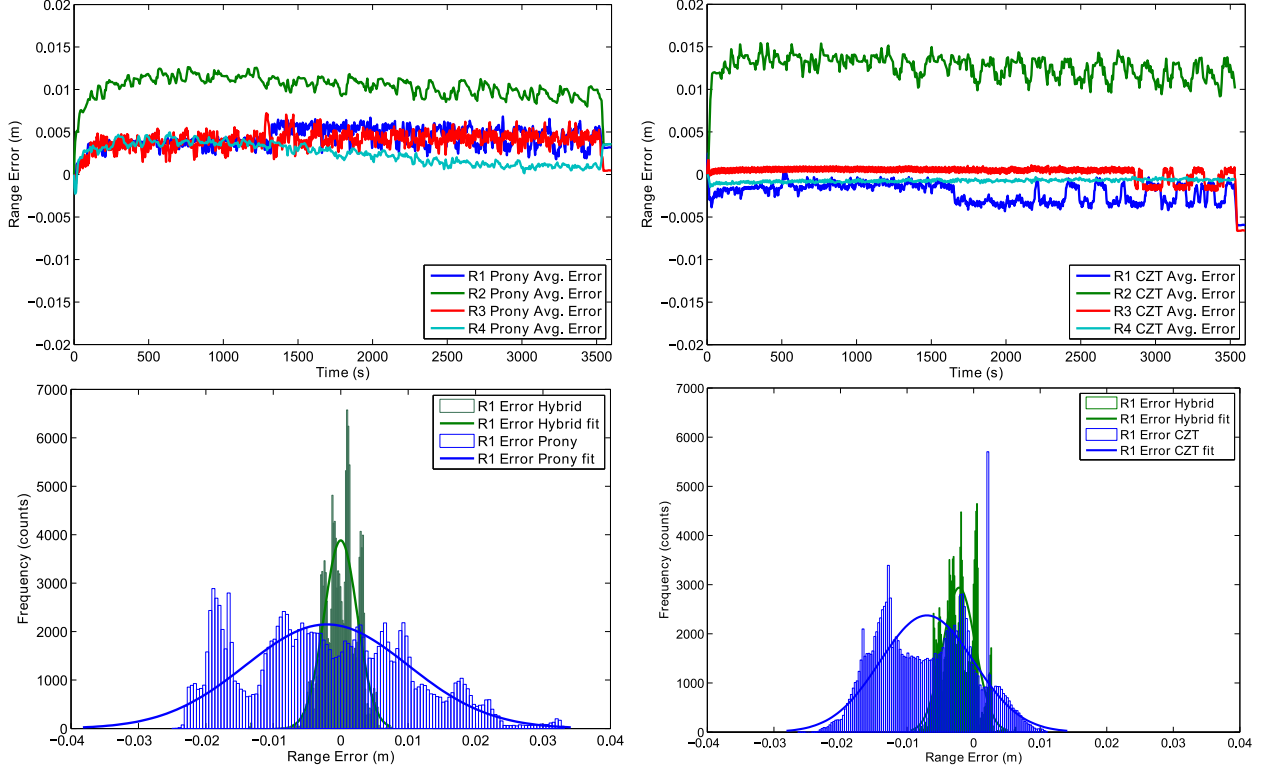


Fig. 7.12. Top, calibration stability over 1 hr shown through 10 s moving average of range error on concrete (6/20/12). Bottom, coarse and fine range error distribution of R1 with normal distribution fit. Prony on left, Chirp- z (CZT) on right.

Each CW phase measurement is converted to range after first selecting the wavelength bin n using the coarse range solution. The wideband measurement (~ 3.9 cm $< \lambda < \sim 4.8$ cm) results in approximately 3 different n selections across the band. Occasionally, near the transitions of n there can be wavelength size errors due to noise on the coarse range or the CW phase (Fig. 7.11). The final range solution is obtained by averaging all N range estimates across frequency. In Fig. 7.11, the range error for all N (21) measurements as well as the final range solution - the average - is shown. All plotted ranges have their mean range error removed. At 0 s, some measurements are using an incorrect n resulting in a $\sim \lambda$ size range error. The final range solution is less affected by this due to averaging ($\sim \lambda/4$ error). Other methods, such as median filtering or grouping analysis, may perform better than averaging but were not tested in this work.

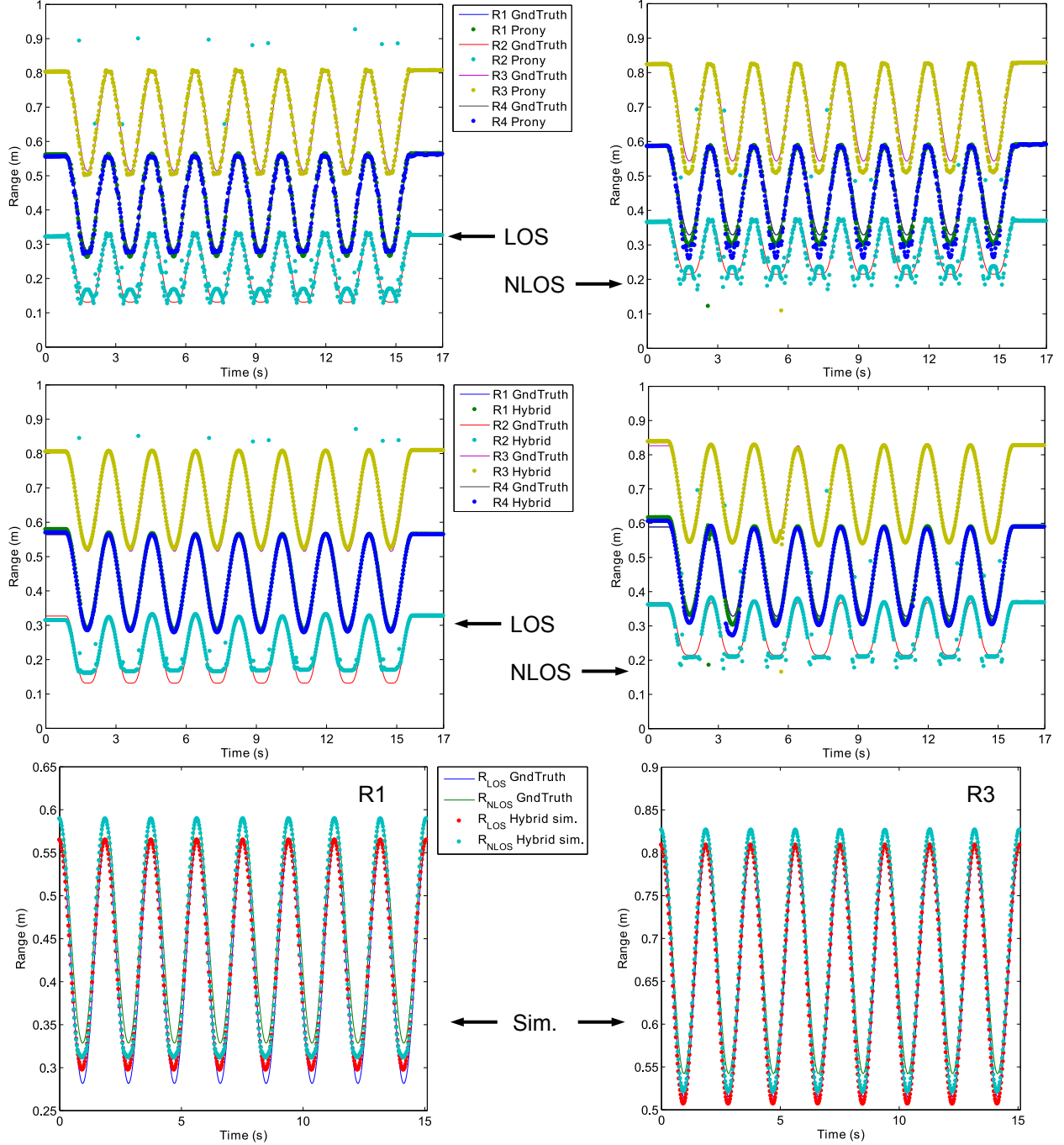


Fig. 7.13. Prony extraction of NLOS (right) and LOS (left) components ($M=20$, $m=2$). Top figures are Prony range output alone, middle figures add CW phase for hybrid ranging. Dataset is concrete at position P1 (6/20/12) with level 0 filtering. Bottom two figures show simulated ($M=3$, $m=2$) R1 and R3 hybrid ranges along with ground truth.

7.2.3.3. CALIBRATION STABILITY

Long term operation of the SRS requires an understanding of the stability of the calibration. To test this, a short 18 s dataset was taken and used to calculate ϵ_R calibration values. These calibration

numbers were then used on the 1 hr dataset. Shown in Fig. 7.12 is a 10 s moving average of the range error on concrete for both the Prony and Chirp- z algorithm with level 2 filtering. Drift over 1 hr is within a couple of mm for all ranges. R1, R3 and R4 all stay within a few mm of the calibration but R2 has \sim 1 cm offset. It is not entirely clear where R2 develops this offset. One possibility is that the RF cables (Fig. 7.4) are stretched across the motion path and above antenna A3, potentially adding a source of multipath. If the cable settled differently between measurements, that could explain the average error shift.

Another interesting artifact is the step functions seen in the Chirp- z R1 and R3. This is due to improper wavelength ambiguity selection on some of the CW measurements. The amplitude of these shifts is only a couple mm ($<<\lambda$) illustrating the benefit of averaging all CW ranges together.

7.2.3.4. MULTIPATH EXTRACTION

In Fig. 7.13 the Prony method is used to extract the LOS and NLOS components. For extraction, $M=20$ and $m=2$. The high M was required to get low noise range estimates. Range calibration was performed by matching the last position (17 s) to the ground truth. Both Prony only as well as CW phase hybrid ranging solutions are shown. Assuming the LOS signal power is much greater than the NLOS, hybrid ranging is less useful on the NLOS range solution because the CW phase measurements are dominated by the LOS signal. Nonetheless, the data is presented as it appears to have a smoothing effect and the range profiles between LOS and NLOS are similar. Statistics are in Table 7.35 and the mean μ value shown is the average error after calibration from the last range position. The LOS component has good ranging accuracy everywhere except below 0.19 m on R2 as seen before. For the NLOS component of R2, a much better match is seen at the valleys of the cosine. It would seem that the reason for the poor LOS range accuracy <0.19 m is

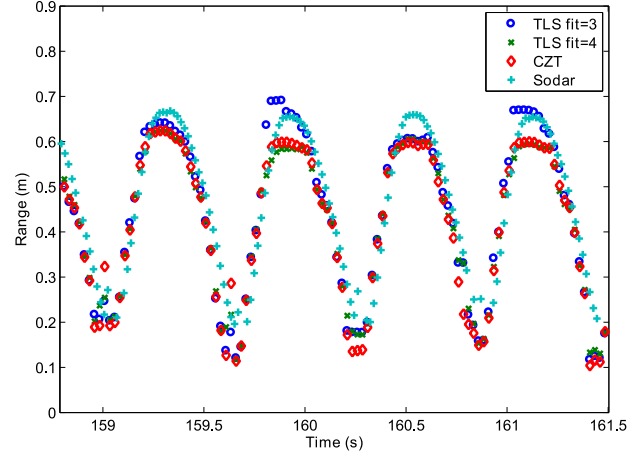


Fig. 7.14. Vivaldi antenna mounted to back of shoe with acoustic sensor (left). Walking results (7/25/12) on carpeted wood walkway using several ranging algorithms and acoustic ranger (right).

because the Prony method becomes overwhelmed by the NLOS in this region and is unable to separate them.

Filter Level 0	Prony NLOS		Hybrid NLOS		Prony LOS		Hybrid LOS		
	Range	μ	σ	μ	σ	μ	σ	μ	σ
R_1	-12.87	19.92		-3.96	19.11	-3.47	8.61	3.72	4.36
R_2	0.55	47.68		1.01	43.69	15.38	85.99	20.21	79.04
R_3	-13.01	22.81		-0.58	17.07	-2.73	7.23	2.36	3.72
R_4	-24.89	33.84		-11.39	27.76	-4.04	9.38	0.30	2.36

Table 7.35. Concrete results in mm with Prony NLOS and LOS extraction ($M=20$, $m=2$). Position P1 cal-2, date taken: 6/20/12

The NLOS R_1 , R_3 and R_4 ranges all appear to overestimate the excursion of the cosine as it moves to the near position when using the Prony method. Hybrid ranging solves the issue on R_3 , however it still remains on R_1 and R_4 . This may be due to an antenna effect such as a phase or polarization change as signal path moves off boresight. In Fig. 7.13, the bottom two figures show simulation results for concrete with Prony parameters $M=3$ and $m=2$. Simulation shows that the NLOS range is overestimated at the valleys similar to the measured results. This suggests that this range error is due to the antenna characteristics. Also, this confirms that the first two Prony solutions correspond to LOS and the NLOS ground reflection signals. For both measured and simulated results, the NLOS range solution required a different calibration than the LOS range. This

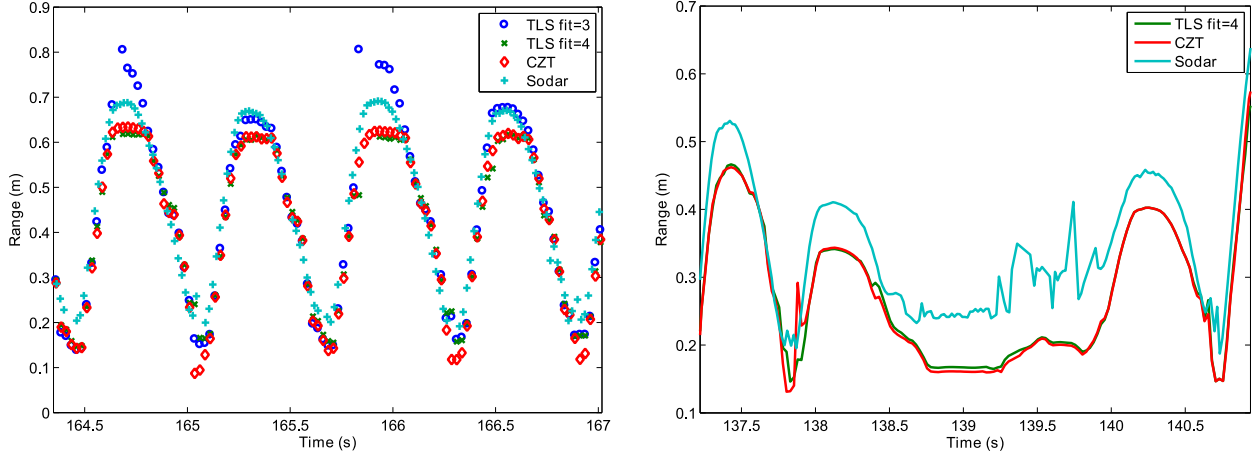


Fig. 7.15. Walking results (7/25/12) on concrete floor using several ranging algorithms and acoustic ranger (left). Ranging results during turn (right).

may be due to the change in signal phase on reflection. For example metal, will add $\pm\pi$ to the propagation phase kR for each frequency. The Prony method computes propagation phase from ΔkR which will shift the location of the NLOS solution when incorporating the surface reflection phase shift across frequency.

7.2.4. WALKING TEST

7.2.4.1. SINGLE RANGER HEEL MOUNT

The SRS single ranger with Vivaldi antennas was mounted on a shoe near the heel along with an acoustic range sensor with a few cm accuracy [6]. The SRS hardware used an older VCO with a sweep range of 6.1-7.5 GHz, $N=21$, $f_R=600$ Hz and a range update rate of 40 Hz. Fig. 7.14 shows the results of with level 0 filtering, Chirp- z , TLS Prony with $M=3,4$, $m=1$ and sodar results. Surface construction consists of ~ 8.9 cm of wood covered by carpet and supported by steel joists and a concrete wall. The SRS shows good agreement with the acoustic sensor (sodar) throughout most of the step though the sensors are not co-located. The Prony solution with $M=3$ occasionally shows much higher peak ranges than the acoustic sensor especially compared to Chirp- z . Increasing the

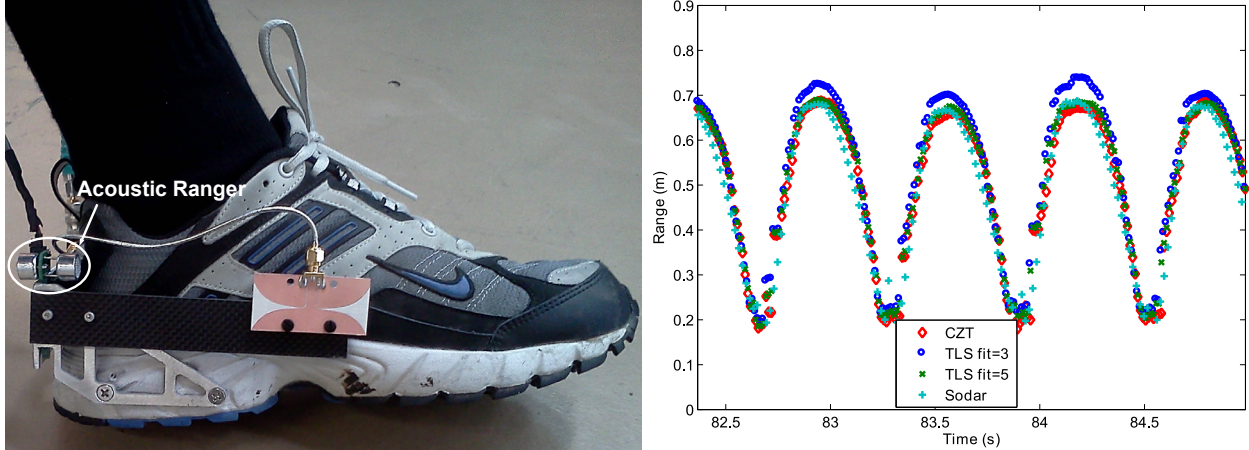


Fig. 7.16. Vivaldi antenna mounted in the forward position above arch of shoe (left). Walking results (7/27/12) on concrete floor using several ranging algorithms and acoustic ranger (right).

Prony fit order to $M=4$ appears to correct this behavior suggesting that additional multipath with the mount is the source of this effect.

A concrete surface was also tested with this antenna configuration and SFCW settings and is shown in Fig. 7.15. Again the Prony algorithm sometimes overestimates range at the peaks of the stride motion (maximum shoe separation) when using $M=3$. Increasing the fit order to 4 appears to have much better results though without ground truth it is hard to know which is more correct. Also shown in Fig. 7.15 is the ranging solution while the walker is turning around. This maneuver is not optimal for the sodar's gain pattern (directed forward and backwards on each shoe) as it has higher variance in the range compared to the SRS. Accurate measurements during heading changes are especially important for inertial navigation performance and the SRS has a large advantage here.

7.2.4.2. SINGLE RANGER ARCH MOUNT

The SRS single ranger was also tested with the Vivaldi antennas mounted forward near the arch of the shoe. A 1/8" thick carbon fiber bar is used to extend the antenna to the forward position. All SFCW settings are the same though range update rate was increased to 80 Hz. As before, a TLS Prony fit order of 3 appears to have problems with overestimating the range compared to the Chirp-

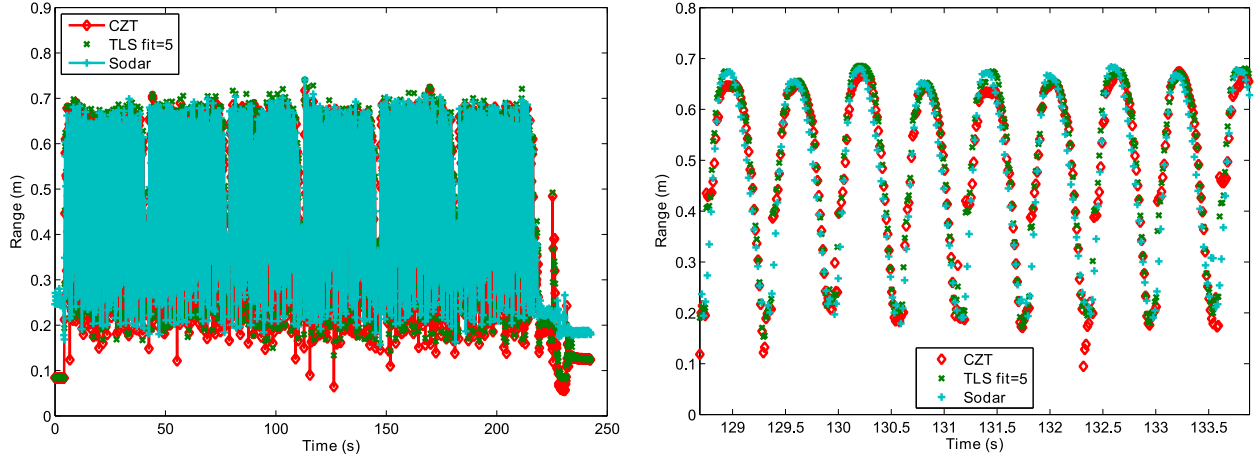


Fig. 7.17. Walking results (7/27/12) on concrete floor using several ranging algorithms and acoustic ranger (sodar). Full dataset view (left) and zoomed section (right).

z (Fig. 7.16). For this mount configuration, the fit order needed to be increased to $M=5$ for better agreement with the Chirp- z computed range. Compared to the sodar, the SRS qualitatively matches the expected range profile of a forward mounted antenna. During the falling edge of the range, the moving shoe heel is pitched down, rotating about the arch location as it lifts off the ground and swings forward. This results in a slightly shorter range from the acoustic sensor located at the heel compared to the Vivaldi antennas at the arch as shown in Fig. 7.16.

At the beginning and end of this walking dataset, the shoes were positioned side-by-side approximately 10 cm from each other. In Fig. 7.17, the entire walking data set is shown. The SRS solution starts and ends near 10 cm. The sodar has significant error here due to its gain pattern. Also shown is spurious ranges below 0.2 m in the Chirp- z that are not seen in the Prony or sodar data. These ranges occur when the shoes are swinging past each other. This suggests that the Prony method is able to better estimate range even when moving through the nulls of the Vivaldi antenna.

Initially, the Vivaldi antenna was mounted approximately centered on the carbon fiber bar. This position produced erratic range results as shown in Fig. 7.18. The reason for this behavior is believed to be from the carbon fiber RF absorption properties. Measured return loss of the antenna

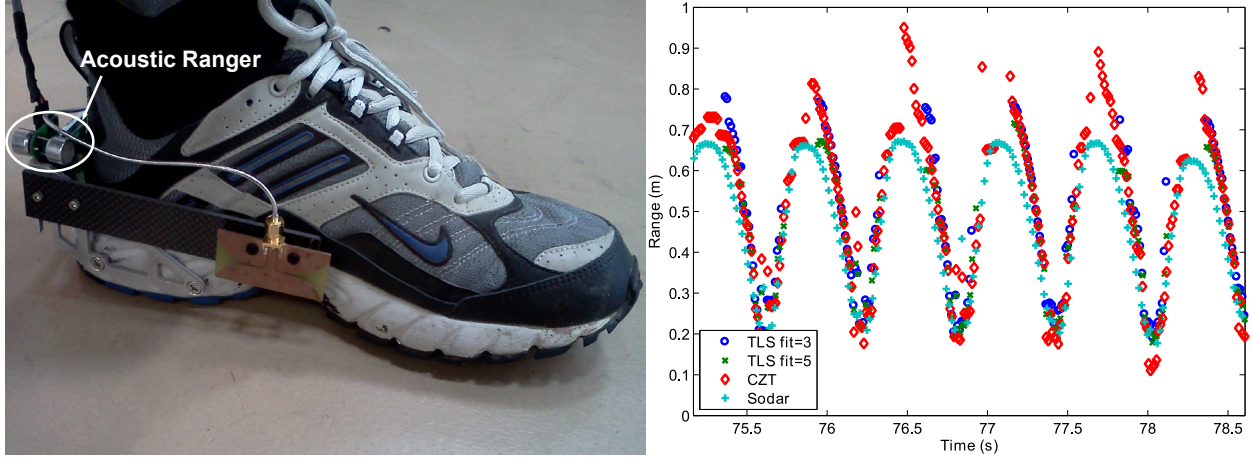


Fig. 7.18. Vivaldi antenna mounted in the forward position above arch of shoe and centered on the carbon fiber bar (left). Walking results (7/27/12) on concrete floor using several ranging algorithms and acoustic ranger (right).

is significantly changed in this mounting configuration. Shifting the antenna off center, as in Fig. 7.16, fixes the return loss issue and stabilizes the range solution.

7.2.4.3. MULTI-RANGER TEST

Currently only the patch antenna has been used in walking tests with the SRS Multi-Ranger configuration. Results from this test illustrated the need for an antenna pattern like the Vivaldi where the gain is directed along the path of the shoe. The SRS hardware used a VCO with a sweep range of 6.1-7.5 GHz, $N=21$, $f_R=600$ Hz and a range update rate of 40 Hz. The Prony algorithm was configured with $M=3$, $m=1$. Patch antennas were mounted onto a 0.25" thick Nylon/Kevlar composite bar (Hydlar Z). In Fig. 7.19, the unfiltered range solution along with IMU range solution is plotted. The patch has reasonable performance when the shoes are close together, as expected due to the pattern gain of the antenna. At the peak of the stride, the patch has large errors. This corresponds to the lowest gain of the antennas therefore it may be expected that range accuracy would become degraded. However simulation did not predict such large errors.

Examining the right graph in Fig. 7.19 shows measured and simulated signal power of the Prony solution. The measured solution has a much larger power variance, especially at the peak ranges.

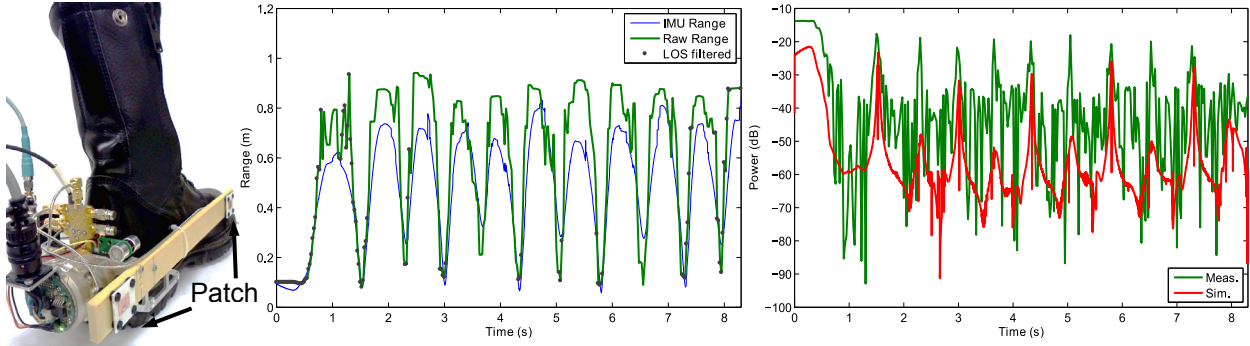


Fig. 7.19. Patch antenna mounted to shoe on Hydar Z material (left). R1 walking results using SRS Prony algorithm and LOS filtering (middle). Simulated and measured R1 Prony power (right).

This may be due to fringing effects of the patch's finite ground plane near the dielectric of the Hydar Z mount. Using the SRS Simulator to calculate the LOS vector, a filter can be created to reject ranges whose LOS vector approaches the edge of the patch. The middle graph of Fig. 7.19 shows a LOS filter with the angle off the normal of the patch limited to 84.4° . This rejects a large fraction of the measurements because the shoes may not remain approximately parallel to each other throughout the step (depending on the walking subject). The remaining data points generally agree well with the IMU computed range – though there are a few that were missed by the filter. While filtering can reduce the errors associated with this patch antenna, the Vivaldi antenna performs much better with less aggressive range filters.

7.3. SUMMARY

Stage measurements show that the SRS Multi-Ranger can achieve sub-cm average RMS error over multiple surfaces. Appropriate filtering in problem regions of the antenna pattern can bring the average RMS error to a few mm. Constraining motion along the optimal antenna pattern was demonstrated to achieve sub-mm error. Hybrid ranging was found to lower ranging error in the presence of multipath. SRS calibration was shown to be stable within a few mm over an hour, though one range experienced a 1 cm initial offset possibly due to experimental setup. The SRS Simulator was useful in analyzing problems in measured ranges. Discrepancies between the SRS

Simulator and measurement in certain regions appear to be from the limited scope of the antenna models which lacked simulation of mounting hardware.

Walking tests showed that the Prony fit order needs to be increased to reduce multipath errors from the mount. Good agreement was found between the SRS and sodar, though the SRS seems to have better accuracy when the shoes are close. The current patch antenna design proved to be unsuitable for walking due to the gain pattern and possible interaction with the mount.

CHAPTER 8

8. CONCLUSION

In this work, a stepped-frequency continuous wave ranging sensor was developed to aid pedestrian inertial navigation by measuring the distance in between shoes. The Shoe Ranging Sensor was analyzed through simulation and measurements on a motion stage. Measured error performance was found to be sub-cm RMS across different walking surfaces with appropriate range filtering. Sub-mm RMS error was attained when the antenna was favorably positioned leading to the conclusion that the antenna is the key factor to the SRS performance. A multiple ranging sensor architecture was developed using time-domain multiplexing and multiple antennas that enables inertial heading errors to become observable under pedestrian navigation.

Performance of the SRS is primarily limited by antenna performance rather than transceiver hardware. This is because the required coherence time of the shoe-to-shoe channel is so low at a few ns that the stability requirement of the VCO is easily met. The benefit of this is the transceiver hardware, which used a homodyne architecture and unlocked VCO, can be designed for ultra-low power and low cost yet still meet the required performance. The use of SFCW modulation also allows for lower sampling rate ADCs, which further reduces power consumption.

Two different ranging algorithms were presented; a Fourier approach using the Chirp- z transform and a parametric estimation technique known as total least squares Prony. With hybrid ranging, the Chirp- z and Prony method had similar error performance when the motion was confined to avoid problem regions of the antennas. In those problem regions, the Prony method was able to perform better. The Prony method is expected to perform well by separating LOS from multipath components, potentially achieving super-resolution. Actual ranging performance and multipath extraction have increased uncertainty because the Prony method does not attempt to separate the frequency dependent polarization phase from the propagation phase.

8.1. CONTRIBUTIONS

1. **Derivation of SFCW and hybrid ranging accuracy constraints** – chapter 2. Cramér-Rao Lower Bound was solved for SFCW radar modulation. SFCW accuracy was shown to be bounded by FMCW accuracy for large N and a given signal-to-noise energy ratio. The required accuracy of a coarse range estimate was shown to be 0.3λ for a 76% probability of correctly resolving wavelength ambiguity in a hybrid CW phase ranging algorithm.
2. **Extension of Friis Equation to include polarization phase of arbitrary oriented antennas** – chapter 3. The Friis transmission equation was reformulated in terms of the far-field electric field, allowing for a more complete description of polarization induced phase from arbitrarily oriented antennas. This allows for a more accurate simulation of propagation with complicated antenna polarization characteristics.
3. **Experimental verification of polarization phase term in Friis equation extension** – chapter 5. A two element arrayed Vivaldi antenna was rotated through 360° to verify the

predicted signal phase due to polarization coupling. The experimental results agreed well with simulation in regions where the antenna geometry was sufficiently modeled.

4. **Developed SRS Simulator using 2-ray channel model and IMU data to analyze SRS performance on different surfaces and antennas** – chapter 2, 5. A channel simulator was developed in Matlab that generated a 2-ray model including polarization phase effects based on IMU data and simulated antenna patterns. This allows predication and analysis of SRS performance limited by the accuracy of the antenna models.
5. **Characterization of SRS Multi-Ranger hardware with different surfaces, ranging algorithms and antennas** – chapter 7. The SRS was mounted to a linear motion stage above several surfaces to allow analysis of error performance and ranging algorithms. Walking tests with the SRS showed good agreement with an acoustic range sensor and found the Vivaldi antenna to have the most consistent performance throughout the step.
6. **SRS single and Multi-Ranger architecture with sub-cm measured error performance** – chapter 2, 6, 7. A low-power and low-cost ranging sensor architecture was designed and extended to provide multiple ranges with minimal increase in complexity. The SRS achieves antenna limited performance of sub-cm accuracy when measured with motion similar to walking and sub-mm when configured for optimal antenna alignment.

8.2. FUTURE WORK

There are several directions for future research into the SRS that should be explored. These future research areas are broken down into hardware, simulation and algorithms and are described in detail below.

8.2.1. HARDWARE

This work found that SRS performance is limited primarily by antenna effects, particularly from nulls and coupling with the mount. A more focused effort to optimize an antenna for the mount may greatly increase overall performance throughout the step. The patch antenna was simulated to have much better performance than the Vivaldi due to its polarization purity. However the measured performance was significantly worse due to coupling with the mount. A modified ground plane integrated with the mount may result in more stable performance.

The SRS Simulator also suggested that reordering the SFCW sweep can reduce the effect of Doppler shift on the range error. This was not tested in hardware due to time constraints, though it is fairly easy to implement. Care should be taken to perform calculations and calibration on properly ordered measurements.

A more advanced SRS design using a mm-wave antenna array may have some interesting advantages. The SRS in its current configuration performs best when the LOS signal remains within the main beam of the antennas. Beam-steering guided by the IMU may allow the LOS signal to always be within the main beam throughout the step. Additionally, the steered main beam angle may be suitable to provide vector ranging without requiring multiple antenna pairs.

One drawback of the current SRS architecture is the requirement of long phase stable cables to be routed along each leg. This approach allows high accuracy through the use of a single oscillator for ranging. A possible solution is an active target or retroreflector array [45] on the other shoe. The retroreflector retransmits coherently the received signal back towards the transceiver. Range is computed in the same method as traditional radar because the signal travels through the channel twice. An X-band system may result in an array too large for the shoe so a single antenna element may be preferred. An active (amplified) design is desirable to counteract channel loss. Traditional

two-port amplifiers in retroreflectors require significant isolation through the use of hybrids or circulators to prevent oscillation between receive and transmit signal paths. An interesting solution to this problem is to use a one-port negative resistance amplifier, [46] [47], which can simplify the retroreflector design to a single antenna and a single transistor. Simple modulation may be performed on the retroreflector to aid in distinguishing from multipath or multiple retroreflectors.

8.2.2. SIMULATION

The SRS Simulator did not always match well to measured results due to incomplete HFSS modeling of the mounted antenna. One reason for this was the lack of microwave models in the literature for the carbon fiber mounting brackets. Dielectric properties of the carbon fiber could be measured so that a more complete HFSS model may be made. Another option is to have a 3D antenna pattern scan of the entire shoe with the SRS mounted. With accurate antenna models, a more complete position and orientation based range filtering may be developed by using the SRS simulator to map out problem regions for a particular antenna and surface.

8.2.3. ALGORITHMS

This work only explored one parametric modeling technique. There may be others that are a better fit. The matrix pencil method (MPM) has been shown to outperform the TLS Prony under high noise [48]. Prony ranging performance appeared to be limited by frequency dependent parameters such as the polarization phase. It may be possible to extend the Prony method or develop a new method based on the channel model in chapter 3 to extract these parameters and increase ranging accuracy.

APPENDIX A

A. COORDINATE TRANSFORMATIONS

It is convenient to maintain several independent coordinate systems (frames) when ray tracing between shoes. The global coordinate system, North-East-Down or NED, is stationary whereas all other coordinate systems may have some orientation and translation with respect to the NED frame. There are two IMU frames (one for each shoe) and an antenna (ANT) frame for each IMU. The IMU frame may have an arbitrary orientation and position with respect to the NED frame however the antenna frames have a fixed transformation to the corresponding IMU frame.

Ray tracing requires the line-of-sight (LOS) vector from the NED frame be transformed into the antenna frame so that the antenna electric field can be determined along the vector. The antenna electric field has two orthogonal components to the LOS vector which must be transformed back to NED frame so that the coupling between the two antennas can be found. The antenna frame is the same coordinate system that is used to model the antenna in Ansoft HFSS. The steps involved calculating these transformations will be shown initially for the case where the IMU frame has some rotation about its x-axis. Subsequently, a brief discussion of the steps required to accommodate an arbitrary IMU orientation will be presented.

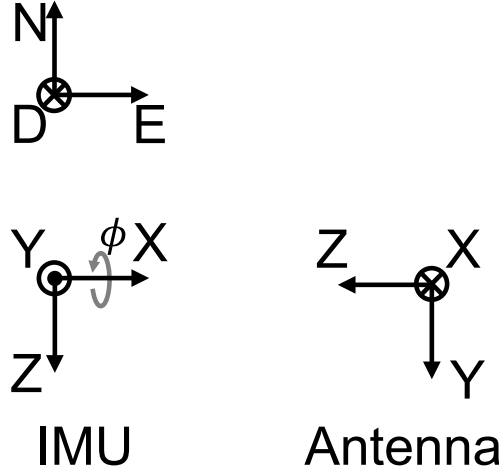


Fig. A.1. Global NED, IMU and antenna (ANT) frame definitions. All frames and rotations use right-handed conventions.

A.1. SINGLE AXIS ROTATION

A.1.1. ROTATION MATRICES

In Fig. A.1 the coordinate systems are defined in their initial orientation. Only one IMU and antenna frame are shown as the second set has identical initial orientation, though different origins, in this example. The positions of the IMU and antennas relative to their parent coordinate system (in superscript brackets) are:

$$P_{IMU1}^{[NED]} = [X_{I1}; Y_{I1}; Z_{I1}] \quad (A.1)$$

$$P_{IMU2}^{[NED]} = [X_{I2}; Y_{I2}; Z_{I2}] \quad (A.2)$$

$$P_{ANT1}^{[IMU1]} = [X_{A1}; Y_{A1}; Z_{A1}] \quad (A.3)$$

$$P_{ANT2}^{[IMU2]} = [X_{A2}; Y_{A2}; Z_{A2}] \quad (A.4)$$

To convert a 3D vector from one frame to another, a 3x3 rotation matrix is needed. Given two frames whose coordinate axes are a multiple of 90° from each other as in Fig. A.1, the rotation matrix R is composed of 1's and 0's and can be defined by inspection. The convention that will be used here is the superscript on R indicates the initial frame and the subscript indicates the final

frame i.e. R_{ANT1}^{IMU1} describes a rotation matrix to transform a vector from the IMU1 frame to the ANT1 frame ($P^{[ANT1]} = R_{ANT1}^{IMU1}P^{[IMU1]}$). To define R in the static case ($\phi = 0$), the rows of R are determined such that the dot product between the row and the input vector selects the component that lines up with the output vector. For example, $X_A = -Y_I$, therefore the first row of R_{ANT1}^{IMU1} is $[0 \ -1 \ 0]$. The rotation matrices for this problem can be defined as

$$R_{ANT1}^{IMU1} = R_{ANT2}^{IMU2} = \begin{bmatrix} 0 & -1 & 0 \\ 0 & 0 & 1 \\ -1 & 0 & 0 \end{bmatrix} \quad (A.5)$$

$$R_{NED}^{IMU1} = R_{NED}^{IMU2} = \begin{bmatrix} 0 & 0 & -1 \\ 1 & 0 & 0 \\ 0 & -1 & 0 \end{bmatrix}. \quad (A.6)$$

Some properties of rotation matrices need to be defined. The transpose and inverse of R are identical and invert the rotation (i.e. $R_{IMU1}^{ANT1} = R_{IMU1}^{IMU1T}$). Rotation matrices can be concatenated to form a composite transformation – for example, from NED to ANT1. The order of concatenation is from right to left with the rightmost matrix the starting frame and the leftmost the ending frame (i.e. $R_{ANT1}^{NED} = R_{ANT1}^{IMU1}R_{IMU1}^{NED}$). The transpose of concatenated rotations will flip this order (i.e. $R_{ANT1}^{NEDT} = R_{NED}^{ANT1} = R_{IMU1}^{NEDT}R_{ANT1}^{IMU1T}$).

A single axis rotation of IMU1 as in Fig. A.1, requires a new R_{NED}^{IMU1} matrix. The rotation matrix for a right-hand rotation about the x, y or z-axis by the corresponding angles ϕ , θ and ψ is defined as [49]

$$R_x = \begin{bmatrix} 1 & 0 & 0 \\ 0 & \cos(\phi) & -\sin(\phi) \\ 0 & \sin(\phi) & \cos(\phi) \end{bmatrix}, \quad (A.7)$$

$$R_y = \begin{bmatrix} \cos(\theta) & 0 & \sin(\theta) \\ 0 & 1 & 0 \\ -\sin(\theta) & 0 & \cos(\theta) \end{bmatrix}, \quad (A.8)$$

$$R_z = \begin{bmatrix} \cos(\psi) & -\sin(\psi) & 0 \\ \sin(\psi) & \cos(\psi) & 0 \\ 0 & 0 & 1 \end{bmatrix}. \quad (\text{A.9})$$

Through concatenation with (A.6) and (A.7), the rotation matrix from IMU1 to NED is now

$$R_{NED}^{IMU1} = \begin{bmatrix} 0 & 0 & -1 \\ 1 & 0 & 0 \\ 0 & -1 & 0 \end{bmatrix} \begin{bmatrix} 1 & 0 & 0 \\ 0 & \cos(\theta) & -\sin(\theta) \\ 0 & \sin(\theta) & \cos(\theta) \end{bmatrix}. \quad (\text{A.10})$$

A.1.2. LOS VECTOR IN ANTENNA FRAME

The LOS between ANT1 and ANT2 can now be calculated including the effects of translation and rotation of IMU1 (IMU2 is fixed). To define the LOS vector, the antenna positions within the NED frame are required. From (A.1)-(A.4), (A.6) and (A.10),

$$P_{ANT1}^{[NED]} = R_{NED}^{IMU1} P_{ANT1}^{[IMU1]} + P_{IMU1}^{[NED]}, \quad (\text{A.11})$$

$$P_{ANT2}^{[NED]} = R_{NED}^{IMU2} P_{ANT2}^{[IMU2]} + P_{IMU2}^{[NED]}, \quad (\text{A.12})$$

$$\mathbf{LOS}^{[NED]} = P_{ANT2}^{[NED]} - P_{ANT1}^{[NED]}. \quad (\text{A.13})$$

The LOS vector is transformed to each antenna frame using (A.5),(A.6), (A.10) and (A.13)

$$\mathbf{LOS}^{[ANT1]} = R_{ANT1}^{IMU1} R_{NED}^{IMU1T} \mathbf{LOS}^{[NED]}, \quad (\text{A.14})$$

$$\mathbf{LOS}^{[ANT2]} = R_{ANT2}^{IMU2} R_{NED}^{IMU2T} (-\mathbf{LOS}^{[NED]}), \quad (\text{A.15})$$

A.1.3. SPHERICAL UNIT VECTORS IN NED FRAME

In Fig. A.2, the spherical coordinate system used by the antennas is shown. Useful relationships between Cartesian and spherical are [50]

$$r = \sqrt{x^2 + y^2 + z^2}, \quad (\text{A.16})$$

$$\theta = \arccos(z/r), \quad (\text{A.17})$$

$$\phi = \text{atan2}(y, x) \quad (\text{A.18})$$

$$\hat{\mathbf{r}} = \sin(\theta) \cos(\phi) \hat{\mathbf{x}} + \sin(\theta) \sin(\phi) \hat{\mathbf{y}} + \cos(\theta) \hat{\mathbf{z}}, \quad (\text{A.19})$$

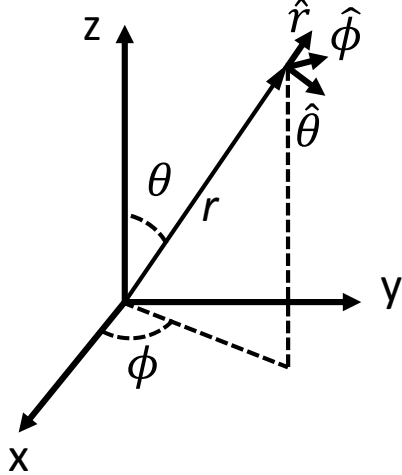


Fig. A.2. Spherical coordinate system used for antenna electric field vectors.

$$\hat{\theta} = \cos(\theta) \cos(\phi) \hat{x} + \cos(\theta) \sin(\phi) \hat{y} - \sin(\theta) \hat{z}, \quad (\text{A.20})$$

$$\hat{\phi} = -\sin(\phi) \hat{x} + \cos(\phi) \hat{y}, \quad (\text{A.21})$$

where \hat{r} , $\hat{\theta}$, and $\hat{\phi}$ are unit vectors defined in Cartesian coordinates. Note, θ and ϕ here are different angles than used with the rotation matrices in the previous section.

The antenna electric field description is compactly stored in a spherical coordinate system which, though convenient, adds the difficulty of unit vectors that change with the LOS vector. Typically it is useful to have the electric field unit vectors described in the NED frame which is easily done by inverting the rotation matrices used in (A.14) and (A.15) to convert the LOS vectors to the antenna frames. The inversion operation involves flipping the left-right order of the rotation matrices and the transpose (inverse) of each matrix. Using (A.5), (A.6), and (A.10), the unit vectors for each antenna (denoted by subscript) in NED are

$$\hat{\theta}_1^{[NED]} = R_{NED}^{IMU1} R_{ANT1}^{IMU1T} \hat{\theta}_1^{[ANT1]}, \quad (\text{A.22})$$

$$\hat{\phi}_1^{[NED]} = R_{NED}^{IMU1} R_{ANT1}^{IMU1T} \hat{\phi}_1^{[ANT1]}, \quad (\text{A.23})$$

$$\hat{\theta}_2^{[NED]} = R_{NED}^{IMU2} R_{ANT2}^{IMU2T} \hat{\theta}_2^{[ANT2]}, \quad (\text{A.24})$$

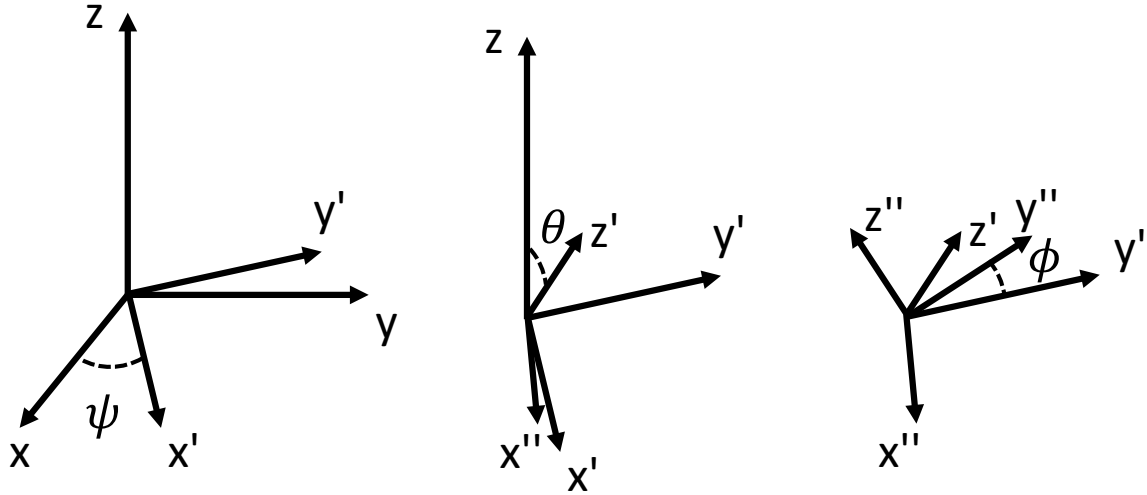


Fig. A.3. Euler rotation sequence (zyx, left to right) to $x'' y'' z''$ frame.

$$\hat{\phi}_2^{[NED]} = R_{NED}^{IMU2} R_{ANT2}^{IMU2T} \hat{\phi}_2^{[ANT2]}, \quad (A.25)$$

where $\hat{\mathbf{r}}$ could be similarly defined however is unnecessary as there is no electric field component in that direction for far-field (by definition).

A.2. EULER ANGLES

In the navigation case, the IMU frame will not be constrained to rotation along a single axis. According to Euler, the transformation between any two frames can be described by three successive rotations about different axes [49]. The convention used here is known as zyx Euler and is convenient because the Euler angles (ψ, θ, ϕ) are similar to heading, pitch, and roll measured by the IMU. A transformation from IMU to NED frame involves a rotation about the IMU z-axis by ψ , rotation about the new y-axis by θ , and finally a rotation about the new x-axis by ϕ (Fig. A.3). Using the single axis rotation matrices (A.7)-(A.9), the composite rotation is

$$R_{NED}^{IMU1} = R_z(\psi_1) R_y(\theta_1) R_x(\phi_1), \quad (A.26)$$

$$R_{NED}^{IMU2} = R_z(\psi_2) R_y(\theta_2) R_x(\phi_2). \quad (A.27)$$

For completeness, the inverse rotation is

$$R_{IMU1}^{NED} = R_x(\phi_1)^T R_y(\theta_1)^T R_z(\psi_1)^T, \quad (\text{A.28})$$

$$R_{IMU2}^{NED} = R_x(\phi_2)^T R_y(\theta_2)^T R_z(\psi_2)^T. \quad (\text{A.29})$$

To find Euler angles from a rotation matrix, e.g. R_{NED}^{IMU1} , it is useful to condense (A.26) into

$$R_{NED}^{IMU1} = \begin{bmatrix} c_{\theta_1} c_{\psi_1} & -c_{\phi_1} s_{\psi_1} + s_{\phi_1} s_{\theta_1} c_{\psi_1} & s_{\phi_1} s_{\psi_1} + c_{\phi_1} s_{\theta_1} c_{\psi_1} \\ c_{\theta_1} s_{\psi_1} & c_{\phi_1} c_{\psi_1} + s_{\phi_1} s_{\theta_1} s_{\psi_1} & -s_{\phi_1} c_{\psi_1} + c_{\phi_1} s_{\theta_1} s_{\psi_1} \\ -s_{\theta_1} & s_{\phi_1} c_{\theta_1} & c_{\phi_1} c_{\theta_1} \end{bmatrix}, \quad (\text{A.30})$$

where, for compactness, ‘c’ and ‘s’ indicate cosine and sine respectively with the angle in subscript.

The Euler angles are found by trigonometry and combination of elements (row, column) in the rotation matrix to isolate the corresponding angle

$$\psi_1 = \text{atan2}\left(R_{NED}^{IMU1}(2,1), R_{NED}^{IMU1}(1,1)\right), \quad (\text{A.31})$$

$$\theta_1 = \text{asin}\left(-R_{NED}^{IMU1}(3,1)\right), \quad (\text{A.32})$$

$$\phi_1 = \text{atan2}\left(R_{NED}^{IMU1}(3,2), R_{NED}^{IMU1}(3,3)\right). \quad (\text{A.33})$$

REFERENCES

- [1] D. Cyganski et al., "WPI Precision Personnel Locator System," in *Institute of Navigation National Technical Meeting*, San Diego, 2007, pp. 806-817.
- [2] Hans G. Schantz, "A Real-Time Location System Using Near-Field Electromagnetic Radiation," in *IEEE Antennas and Propagation Society International Symposium*, Honolulu, 2007, pp. 3792-95.
- [3] Eric Foxlin, "Pedestrian Tracking with Shoe-Mounted Inertial Sensors," *IEEE Comput. Graph. Appl.*, vol. 25, no. 6, pp. 38-46, Dec. 2005.
- [4] Lauro Ojeda and Johann Borenstein, "Personal Dead-Reckoning System for GPS-Denied Environments," in *IEEE International Workshop on Safety, Security and Rescue Robotics*, Rome, 2007, pp. 1-6.
- [5] Timothy J. Brand and Richard E. Phillips, "Foot-to-Foot Range Measurement as an Aid to Personal Navigation," in *ION 59th Annual Meeting/CIGTF 22nd Guidance Test Symposium*, Albuquerque, 2003, pp. 113-121.
- [6] Michel Laverne, Michael George, Dale Lord, Alonzo Kelly, and Tamal Mukherjee, "Experimental Validation of Foot to Foot Range Measurements in Pedestrian Tracking," in *Proceedings of ION GNSS*, Portland, 2011, p. 1386.
- [7] G. W. Gilman, H. B. Coxhead, and F. H. Willis, "Reflection of Sound Signals in the Troposphere," *J. Acoust. Soc. Am.*, vol. 18, no. 2, pp. 274-83, July 1946.
- [8] Richard Przybyla et al., "An Ultrasonic Rangefinder based on an AlN Piezoelectric Micromachined Ultrasound Transducer," in *IEEE Sensors*, Hawaii, 2010, pp. 2417 - 2421.
- [9] Valentin Magori, "Ultrasonic Sensors in Air," in *IEEE Ultrasonics Symposium*, Cannes, 1994, pp. 471-481.
- [10] Ulla Wandinger, "Introduction to Lidar," in *LIDAR: Range-Resolved Optical Remote Sensing of the Atmosphere*, Claus Weitkamp, Ed.: Springer, 2005, ch. 1, pp. 1-3.
- [11] Brian Yamauchi, "Fusing Ultra-Wideband Radar and LIDAR for Small UGV Navigation," *Proc.*

SPIE 7692, vol. 76920O, April 2010.

- [12] Hans Gregory Schantz, "On the Origins of RF-Based Location," in *Wireless Sensors and Sensor Networks (WiSNet), 2011 IEEE Topical Conference on*, Phoenix, 2011, pp. 21-4.
- [13] Novatel Inc. (2012, June) Novatel Inc. OEM628 GNSS Receiver. [Online]. <http://www.novatel.com/assets/Documents/Papers/OEM628.pdf>
- [14] ASTYX GmbH Communication & Sensors. (2012, June) Astyx 77GHz Automotive Radar. [Online]. <http://www.astyx.de/download/77ghzautomotiveradarbrochure.pdf>
- [15] Time Domain. (2012, June) Time Domain P400 RCM UWB Radar. [Online]. <http://www.timedomain.com/datasheets/320-0289BP400RCMDatasheetFinal.pdf>
- [16] Eugene Hecht, *Optics*, 4th ed. San Francisco: Addison Wesley, 2002.
- [17] Kevin McClaning, *Wireless Receiver Design for Digital Communications*, 2nd ed. USA: SciTech Publishing, 2012.
- [18] Ken S. Kundert, "Introduction to RF Simulation and its Application," Designers Guide Consulting, Inc., White Paper v2, 2003.
- [19] Merril I. Skolnik, *Introduction to Radar Systems*, 3rd ed.: McGraw Hill, 2001.
- [20] D. R. Wehner, *High-Resolution Radar*, 2nd ed. Boston, USA: Artech House, 1994.
- [21] William David, "FMCW MMW Radar for Automotive Longitudinal Control," University of California, Berkeley, California PATH Research Report UCB-ITS-PRR-97-19 ISSN 1055-1425, 1997.
- [22] C. Zhou, J. Downey, D. Stancil, and T. Mukherjee, "A Shoe to Shoe RF Ranging Sensor for Aiding Inertial Navigation," in *IEEE VTC*, San Francisco, 2011.
- [23] Theodore S. Rappaport, *Wireless Communications: Principles and Practice*, 2nd ed.: Prentice Hall, 2002.
- [24] Constantine A. Balanis, *Antenna Theory: Analysis and Design, 3rd Edition*. Hoboken: John Wiley & Sons, 2005.

- [25] Constantine A. Balanis, *Advanced Engineering Electromagnetics*. Hoboken: John Wiley & Sons, 1989.
- [26] Sung Kim, Jack Surek, and James Baker-Jarvis, "Electromagnetic Metrology on Concrete and Corrosion," *J. Res. Natl. Inst. Stand. Technol.*, vol. 116, no. 3, pp. 655-669, May 2011.
- [27] Edward J. Jaselskis, Jonas Grigas, and Algirdas Brilingas, "Dielectric Properties of Asphalt Pavement," *Journal of Materials in Civil Engineering*, vol. 15, no. 5, pp. 427-434, Sept/Oct 2003.
- [28] Arthur R. Von Hippel, *Dielectric Materials and Applications*. Boston, USA: Artech House, 1995.
- [29] A. Muqaibel, A. Safaai-Jazi, A. Bayram, A. M. Attiya, and S. M. Riad, "Ultrawideband Through-the-Wall Propagation," *Microwaves, Antennas and Propagation, IEE Proceedings*, vol. 152, no. 6, pp. 581-588, December 2005.
- [30] James Baker-Jarvis et al., "Measuring the Permittivity and Permeability of Lossy Materials: Solids, Liquids, Metals, Building Materials, and Negative-Index Materials," NIST, Boulder, Technical Note 1536, 2005.
- [31] Rodger E. Ziemer, William H. Tranter, and D. R. Fannin, *Signals and Systems: Continuous and Discrete*, 4th ed.: Prentice Hall, 1998.
- [32] L. R. Rabiner, R. W. Schafer, and C. M. Rader, "The Chirp z-Transform Algorithm," *IEEE Transactions on Audio and Electroacoustics*, vol. 17, no. 2, pp. 86-92, June 1969.
- [33] Dean A. Frickey, "Using the Inverse Chirp-Z Transform for Time-Domain Analysis of Simulated Radar Signals," in *ICSPAT: Signal Processing Applications and Technology*, Dallas, 1994.
- [34] Michael P. Hurst and Raj Mittra, "Scattering Center Analysis via Prony's Method," *IEEE Transactions on Antennas and Propagation*, vol. 35, no. 8, pp. 986-88, Aug. 1987.
- [35] Francis B. Hildebrand, *Introduction to Numerical Analysis*, 2nd ed. Mineola: Dover Publications, Inc., 1987.
- [36] Md. Anisur Rahman and Kai-Bor Yu, "Total Least Squares Approach for Frequency Estimation Using Linear Prediction," *IEEE Transactions on Acoustics, Speech, and Signal Processing*, vol. 35, no. 10, pp. 1440-54, Oct. 1987.
- [37] Chinghui J. Ying and Randolph L. Moses, "Prony Modeling of Linear FM Radar Data," The

Ohio State University, Columbus, SPANN Technical Report TR-93-01, 1993.

- [38] C. Stagni, A. Italia, and G. Palmisano, "Wideband CMOS LC VCOs for IEEE 802.15.4a Applications," in *European Microwave Integrated Circuit Conference*, Amsterdam, 2008, pp. 246-49.
- [39] G. Cusmai, M. Brandolini, and F. Svelto, "An Interference Robust 0.18 μ m CMOS 3.1-8GHz Receiver Front-End for UWB Radio," in *IEEE Proceedings of the Custom Integrated Circuits Conference*, San Jose, 2005, pp. 157-60.
- [40] Linear Technology Corporation, "LTC2379-18 - 18-Bit, 1.6Msps, Low Power SAR ADC with 101.2dB SNR," Linear Technology Corporation, Milpitas, product datasheet 2011.
- [41] Bevan M. Baas, "A Low-Power, High-Performance 1024-Point FFT Processor," *IEEE Journal of Solid-State Circuits*, vol. 34, no. 3, pp. 380-87, March 1999.
- [42] Huey-Ru Chuang and Liang-Chen Kuo, "3-D FDTD Design Analysis of a 2.4-GHz Polarization-Diversity Printed Dipole Antenna with Integrated Balun and Polarization-Switching Circuit for WLAN and Wireless Communication Applications," *IEEE Transactions on Microwave Theory and Techniques*, vol. 51, no. 2, pp. 374-81, Feb. 2003.
- [43] Yuehe Ge, Karu P. Esselle, and Trevor S. Bird, "E-Shaped Patch Antennas for High-Speed Wireless Networks," *IEEE Transactions on Antennas and Propagation*, vol. 52, no. 12, pp. 3213-19, Dec. 2004.
- [44] I. Linardou, C. Migliaccio, J. M. Laheurte, and A. Papiernik, "Twin Vivaldi Antenna Fed by Coplanar Waveguide," *Electronics Letters*, vol. 33, no. 22, pp. 1835-37, Oct. 1997.
- [45] Prashant K. Ulavapalli, "An Active Subharmonic Retrodirective Array using Dual Polarized Microstrip Antennas," Texas Tech University, Lubbock, M.S. thesis 2004.
- [46] Shyh-Jong Chung, Shing-Ming Chen, and Yang-Chang Lee, "A Novel Bi-Directional Amplifier With Applications in Active Van Atta Retrodirective Arrays," *IEEE Transactions on Microwave Theory and Techniques*, vol. 51, no. 2, pp. 542-47, Feb. 2003.
- [47] Peter Gardner and Dipak K. Paul, "Aspects of the Design of Low Noise, Negative Resistance, Reflection Mode Transistor Amplifiers," *IEEE Transactions on Microwave Theory and Techniques*, vol. 39, no. 11, pp. 1869-75, Nov. 1991.

- [48] Tapan K. Sarkar and Odilon Pereira, "Using the Matrix Pencil Method to Estimate the Parameters of a Sum of Complex Exponentials," *IEEE Antennas and Propagation Magazine*, vol. 37, no. 1, pp. 48-55, Feb 1995.
- [49] David H. Titterton and John L. Weston, *Strapdown Inertial Navigation Technology*, 2nd ed.: Institution of Electrical Engineers and American Institute of Aeronautics and Astronautics, 2004.
- [50] Fawwaz T. Ulaby, *Fundamentals of Applied Electromagnetics*, 4th ed.: Pearson Prentice Hall, 2003.